

Tropical Cyclone Size in Observations and in Radiative-Convective Equilibrium

by

Daniel Robert Chavas

B.S. Atmospheric and Oceanic Sciences, University of Wisconsin-Madison (2007)

B.S. Applied Mathematics, University of Wisconsin-Madison (2007)

Submitted to the Department of Earth, Atmospheric, and Planetary Science

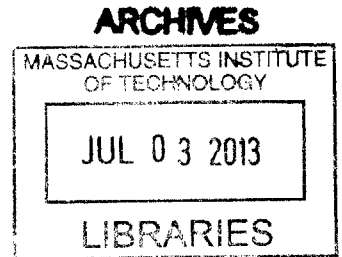
in partial fulfillment of the requirements for the degree of

Doctor of Philosophy in Atmospheric Science

at the

MASSACHUSETTS INSTITUTE OF TECHNOLOGY

June 2013




© Massachusetts Institute of Technology 2013. All rights reserved.

Author


Department of Earth, Atmospheric, and Planetary Science

May 21, 2013

Certified by

 Kerry A. Emanuel
Cecil & Ida Green Professor of Atmospheric Science
Thesis Supervisor

Accepted by

 Robert van der Hilst
Schlumberger Professor of Earth and Planetary Sciences
Head of Dept. of Earth, Atmospheric and Planetary Sciences

Tropical Cyclone Size in Observations and in Radiative-Convective Equilibrium

by

Daniel Robert Chavas

Submitted to the Department of Earth, Atmospheric, and Planetary Science
on May 21, 2013, in partial fulfillment of the
requirements for the degree of
Doctor of Philosophy in Atmospheric Science

Abstract

Tropical cyclone size remains an unsolved problem in tropical meteorology, yet size plays a significant role in the damage caused by tropical cyclones due to wind, storm surge, and inland freshwater flooding. This work explores size, defined as the radius of vanishing wind, in observations and at equilibrium in an idealized numerical model.

First, a climatology of size is created from the QuikSCAT database of near-surface wind vectors for the years 1999-2008. Globally, the distribution of the outer radius is found to be log-normal, with statistically significant variation across ocean basins, but with minimal correlation with various dynamic and thermodynamic parameters.

Second, the sensitivity of the structure of a numerically-simulated axisymmetric tropical cyclone at statistical equilibrium to the set of relevant model, initial, and environmental external parameters is explored. The analysis is performed in a highly-idealized state of radiative-convective equilibrium (RCE). The non-dimensional equilibrium radial wind profile is found to be modulated primarily by a single non-dimensional parameter given by the ratio of the storm radial length scale to the parameterized eddy radial length scale. The relevant storm length scale is shown to be the ratio of the potential intensity to the Coriolis parameter, matching the prediction for the “natural” storm length scale in prevailing axisymmetric tropical cyclone theory. The outer storm circulation is further modulated by a second non-dimensional parameter that represents the non-dimensional Ekman suction rate.

Third, size is explored in three-dimensional “tropical cyclone world” simulations, with preliminary results confirming the relevant length scale obtained in axisymmetry.

Ultimately, the results of the equilibrium storm analysis are insufficient to explain the observed distribution of tropical cyclone size, but they provide the first steps toward a more fundamental understanding of the dynamics of size.

Thesis Supervisor: Kerry A. Emanuel

Title: Cecil & Ida Green Professor of Atmospheric Science

Acknowledgments

It's been a wild ride here – sometimes a struggle, occasionally a big struggle, but more often than not a memorable adventure. I honestly cannot believe that my graduate career is already over, having gazed out from this large 17th floor window taking for granted the clouds, trees, and child's toy of a building that have greeted me every morning for the past five years.

I have to thank first and foremost my advisor, Kerry Emanuel, for taking me on as a student and imparting his infinite wisdom on the science of tropical cyclones and climate and for allowing me the freedom to pursue my interests as I saw fit. My group of close friends within the department, including Marty Singh, Alli Wing, Malte Jansen, Tim Cronin, Neil Zimmerman, and Morgan O'Neill, have provided an endless supply of laughs and support over the years, including plenty of quality conversations about arbitrary topics in the Charney Library. The students in this department are truly outstanding as both scientists and friends. And tremendous thanks goes out to the teaching faculty and staff in the department, which provides an outstanding, broad education in the field.

At MIT I've been so lucky to be able to pursue interests beyond basic science. This includes the opportunity to teach classes and engage others in the policy morass in which our field is embedded, for better or worse. The Science Policy Initiative and the Joint Program on the Science and Policy of Global Change both offered an outlet to meet like-minded students across disciplines and help foster the emerging culture where science and policy embrace rather than repel one another.

In the end, though, nothing can surpass the pure, unadulterated joy derived from the soft landing of a bouncing tennis ball onto the tray of an office chalkboard, released from shoulder height with utmost precision and the subtlest of backspin toward the maroon-dusted floor below. The final score reads: Dan 154, Marty 153. It was only a joke when we said "We play until you graduate". Oh how time flies!

This research is supported in part by the Department of Energy Office of Science Graduate Fellowship Program (DOE SCGF), made possible in part by the Ameri-

can Recovery and Reinvestment Act of 2009, administered by ORISE-ORAU under contract no. DE-AC05-06OR23100.

Contents

| | | |
|----------|--|-----------|
| 1 | Introduction | 21 |
| 1.1 | Motivation | 21 |
| 1.1.1 | Scientific | 21 |
| 1.1.2 | Societal | 22 |
| 1.2 | Review of existing research | 26 |
| 1.2.1 | Observations | 26 |
| 1.2.2 | Modeling | 27 |
| 1.2.3 | Theory | 29 |
| 1.3 | Defining storm size | 33 |
| 1.4 | Objectives | 33 |
| 2 | A QuikSCAT Climatology of Tropical Cyclone Size | 35 |
| 2.1 | Introduction | 35 |
| 2.2 | Data | 36 |
| 2.3 | Methodology | 37 |
| 2.3.1 | Locating TCs | 37 |
| 2.3.2 | Selecting V_{QS} | 38 |
| 2.3.3 | Estimating Outer Radius r_0 | 38 |
| 2.4 | Results | 39 |
| 2.4.1 | Basic statistics | 39 |
| 2.4.2 | Size distribution | 41 |
| 2.4.3 | Control experiments | 43 |
| 2.4.4 | Intra-storm evolution | 44 |

| | | |
|----------|--|-----------|
| 2.4.5 | Case study: Alberto (2000) | 46 |
| 2.5 | Discussion and Conclusions | 49 |
| 3 | Equilibrium Tropical Cyclone Size and Structure in Axisymmetry | 51 |
| 3.1 | Introduction | 51 |
| 3.2 | Methodology | 53 |
| 3.2.1 | Model description | 53 |
| 3.2.2 | Idealized model/environmental RCE set-up | 55 |
| 3.2.3 | Initial perturbation | 57 |
| 3.2.4 | Control simulation parameter values | 58 |
| 3.2.5 | Characterizing equilibrium storm structure | 59 |
| 3.2.6 | Experimental approach: parametric sensitivities and dimensional analysis | 62 |
| 3.2.7 | Potential Intensity in RCE | 63 |
| 3.2.8 | Defining the background state | 64 |
| 3.3 | Results | 66 |
| 3.3.1 | Control run | 66 |
| 3.3.2 | Radial profile sensitivity tests | 67 |
| 3.3.3 | Base case: Inner core | 70 |
| 3.3.4 | Base case: Outer wind field | 74 |
| 3.3.5 | Physical interpretation | 85 |
| 3.3.6 | Estimating l_h | 87 |
| 3.3.7 | Sensitivity to potential intensity | 88 |
| 3.3.8 | Rossby deformation radius | 94 |
| 3.4 | Varying $\frac{C_k}{C_d}$ | 97 |
| 3.4.1 | Inner Core | 99 |
| 3.4.2 | Outer radius | 103 |
| 3.4.3 | Comparison with structural theory | 106 |
| 3.5 | Theoretical scaling for eye | 108 |
| 3.6 | Discussion | 110 |

| | | |
|----------|--|------------|
| 3.7 | Conclusions | 113 |
| 4 | Exploration of Equilibrium Tropical Cyclone Size in Three Dimensional Simulations | 117 |
| 4.1 | Introduction | 117 |
| 4.2 | Methodology | 119 |
| 4.2.1 | CM1 model: 3D | 119 |
| 4.2.2 | Description of simulations | 121 |
| 4.2.3 | Characterizing statistical equilibrium storm structure | 122 |
| 4.3 | TCs in Rotating RCE | 127 |
| 4.3.1 | Self-aggregation | 127 |
| 4.3.2 | Radial wind profiles in the presence of multiple TCs | 128 |
| 4.4 | Size statistics | 130 |
| 4.5 | Discussion | 134 |
| 4.6 | Conclusions | 135 |
| 5 | Conclusions and Future Work | 139 |
| 5.1 | Summary | 139 |
| 5.2 | Future Work | 141 |
| 5.2.1 | Ventilation and equilibrium size | 141 |
| 5.2.2 | Transient size evolution | 142 |
| 5.2.3 | Validation of outer wind field model | 143 |
| 5.2.4 | TC size in more complex environments | 143 |
| 5.2.5 | TC size in the current climate: explaining the log-normal | 144 |
| 5.2.6 | TC size under climate change | 145 |

List of Figures

| | | |
|-----|---|----|
| 1-1 | Visible satellite image of the tropical Atlantic ocean basin from the GOES-East satellite taken on 16 September 2010 at 1445 UTC. Three TCs of very different sizes are identifiable: Karl (small) in the Gulf of Mexico, Igor (large) approaching the Caribbean, and Julia (medium) in the central Atlantic. Source: http://upload.wikimedia.org/wikipedia/commons/d/d5/20100916-1845UTC-GOES-East_visible.jpg | 23 |
| 1-2 | Estimated 1-minute sustained surface wind fields of Hurricanes Camille (1969; left) and Katrina (2005; right) just before landfall near New Orleans (NOAA Hurricane Research Division H*Wind Project, Powell et al. (1998)). At the times shown, their respective peak 1-minute sustained wind speeds were 165 kt and 113 kt and radii of maximum wind were 24 km and 48 km. | 25 |
| 2-1 | Top: Median values of r_{12} (blue) and r_0 (green) of r_0 (red) globally and by basin. All units in [km]. Error bars denote range of two standard deviations from the mean. Bottom: Correlation coefficients between r_0 and various parameters globally and across basins; “day” represents day of the hurricane season. Basins listed are Atlantic (AL), East Pacific (EP), West Pacific (WP), Indian Ocean (IO), and Southern Hemisphere (SH). | 40 |
| 2-2 | Global frequency distribution with Gaussian fit (red line). Top: $\log(r_{12})$; Bottom: $\log(r_0)$ | 42 |

| | | |
|-----|---|----|
| 2-3 | P-values for Gaussian fit to the distribution of $\log(r_{12})$ (blue) and $\log(r_0)$ (red) across basins. | 43 |
| 2-4 | Distribution of $\frac{\partial r_0}{\partial t}$ for all storms with at least four observations. Red lines denote mean (solid) and one standard deviation (dashed) growth rates, with a mean value of 10.9 km day^{-1} | 45 |
| 2-5 | Time evolutions of r_0 for the six storms with at least 14 observations during their lifespans. Red line corresponds to the case with the most observations (22). | 46 |
| 2-6 | Map displaying the NHC Best Track and evolution of Hurricane Alberto (2000). Colors correspond to Saffir-Simpson category; maximum wind speeds from NHC Best Track database. Circles denote QuikSCAT observation, with marker size scaled by QuikSCAT-based estimate of r_0 (see legend). Contours denote climatological distribution of V_p for August (Bister and Emanuel, 2002). | 47 |
| 2-7 | Time series of V_m and V_p (top), r_m and r_0 (bottom) for Alberto (2000). Colors for V_m correspond to Saffir-Simpson category as in Figure 2-6. | 48 |
| 3-1 | Initial three-dimensional radiative-convective equilibrium vertical profile of temperature (red dashed), potential temperature (red solid), and water vapor mixing ratio (blue) for the Control simulation. | 58 |
| 3-2 | Time-mean radial gradient wind profiles at $z = 1.56 \text{ km}$ for days 100-150 as a function of domain width. Note the convergence in storm size beyond $L_{domain} \approx 3000 \text{ km}$ | 60 |
| 3-3 | Comparison of the potential intensity, V_p , calculated from the initial three-dimensional RCE state and the final axisymmetric RCE state outside of the storm across simulation sets varying each of the four governing thermodynamic parameters. | 65 |

| | | |
|-----|--|----|
| 3-4 | For the Control simulation, time evolution of the 2-day running mean V_m , r_m , and r_0 normalized by their respective equilibrium values (upper-right corner). For this simulation, $V_p = 79 \text{ ms}^{-1}$ and $f = 5 \times 10^{-5} \text{ s}^{-1}$. Pink line denotes 30-day period used for equilibrium calculation, and black dashed lines denote $\pm 10\%$ of the equilibrium value. Markers along the abscissa denote estimated time-scales to equilibration. | 67 |
| 3-5 | Equilibrium radial profiles of the gradient wind for simulation sets in which each of the eight dimensional external parameters is varied. The top four panels correspond to the four thermodynamic parameters, for which shading reflects potential intensity from low (light grey) to high (black); the bottom four panels correspond to relevant dynamic parameters, for which shading reflects parameter magnitude from low (light grey) to high (black). | 69 |
| 3-6 | As in Figure 3-5, but with radial profiles normalized as follows: V by V_m and r by r_{ew} . Only those six parameters exhibiting strong structural sensitivity are shown. | 70 |
| 3-7 | Scaling of the equilibrium value of V_m (top) and r_{ew} (bottom) with relevant dimensional parameters, X , normalized by their respective Control values (abscissa). Parameters to which a structural variable exhibits systematic sensitivity are plotted in solid black. | 71 |
| 3-8 | Scaling of the equilibrium values of the non-dimensionalized structural variable V_m (top), r_{ew} (bottom) with the non-dimensional number $C = \frac{V_p}{fl_h}$. Best-fit linear regressions plotted (dash), whose linearly-regressed slopes, corresponding to the estimated power-law scaling exponent in (3.14), and associated 95% confidence intervals listed (parentheses) and r-square values adjusted to account for the number of estimators (top-left corner). For V_m , a logarithmic regression is also shown (dash-dot). Grey fill highlights those simulations for which $V_p(T_{tpp})$ alone is modulated. Grey bars indicate the full range of variability of the 30-day running mean after day 60. | 73 |

| | | |
|------|--|----|
| 3-9 | Comparison of equilibrium radial wind profile for Control simulation (grey) with Eq. (3.18) without (dashed) and with (solid) constant modification ($c = .3$), fit to $r(.75V_m)$ (marked 'X'). | 76 |
| 3-10 | Histogram of optimized constant, c , applied to first term on the RHS of Eq. (3.18) across simulation sets (color). Control simulation is in black. The values are calculated by fitting Eq. (3.18) to $r(.75V_m)$ and then minimizing the mean square error in the region $r(.1V_m < V < .75V_m)$. Values are tested over the range $c = [.1, 10]$. The median is $c = .26$ | 78 |
| 3-11 | Radial profiles of error in the fit of the analytical outer wind model (Eq. (3.18), empirically modified with $c = .3$) to the equilibrium radial wind profile, defined as $V_{E04} - V_{CM1}$, for all simulations varying each of the six relevant dimensional parameters. Error profiles are smoothed with a 10-pt smoother. In the top four panels, shading reflects potential intensity from low (light grey) to high (black); in the bottom two panels, shading reflects parameter magnitude from low (light grey) to high (black). Analytical model is fit to $r(.75V_m)$, with the range $r(.75V_m < V < .1V_m)$ solid and $r(V < .1V_m)$ dashed; radii are normalized by r_0 as calculated from the outer wind model given by Eq. (3.18). Red line depicts mean error over the inner range, and the corresponding mean absolute error (MAE) for the simulation set is listed in the top left corner. | 79 |
| 3-12 | As in Figure 3-6 for varying T_{tpp} , focused on the outer region of the storm. Black curves are the equilibrium radial wind profiles; red curves are solutions of Eq. (3.18) fit directly (top), and fit with $\frac{C_d V_p}{w_{cool}}$ held fixed at its Control value (bottom). Blue dots indicate corresponding r_0 (top) and r_0^* (bottom), and the corresponding scalings with V_p are shown as insets. | 82 |
| 3-13 | Scaling of $r_0/\frac{V_p}{f}$ with C_1 and C_2 , calculated using Eq. (3.18) with empirical fit to simulation results. Marker ('X') denotes Control simulation. Contours depict power law scaling fit given by Eq. (3.21). | 83 |

| | | |
|------|--|----|
| 3-14 | As in Fig. 3-8 but for overall storm size, r_0^* , with C_2 fixed at the Control value. | 84 |
| 3-15 | As in Fig. 3-14 but with r_0^* calculated by applying (3.18) to the numerical equilibrium solution beginning at $r(.2V_m)$ | 86 |
| 3-16 | Estimation of the optimal value of the radial mixing length normalized by $\frac{V_p}{f}$ by matching the logarithmic fit to the data (black dash) to the theoretical relationship of $\frac{V_m}{V_p} = \frac{1}{\sqrt{2}}$ (black dash-dot) for $\frac{C_k}{C_d} = 1$ in Emanuel and Rotunno (2011). The best estimate (grey dot) is approximately $\frac{1}{600}$ of the storm scale. | 89 |
| 3-17 | Scaling of the respective equilibrium values of V_m , r_{ew} , and r_0^* (ordinate) with V_p (abscissa) for the four thermodynamic parameters. Dashed line indicates best fit to all data. For each individual parameter, best fit linear slope (95% CI) and corresponding adjusted r-square statistic listed in lower right corner. Grey bars indicate the full range of variability of the 30-day running mean after day 60. | 90 |
| 3-18 | As in Fig. 3-17 but with r_0^* calculated by applying (3.18) to the numerical equilibrium solution beginning at $r(.2V_m)$ | 91 |
| 3-19 | As in Fig. 3-17 but with r_0^* calculated from (3.18) using the optimal value of c specific to each simulation. Two cases ($T_{tp} = 238 K$, $Q_{cool} = 4 K day^{-1}$) have very large values of c (Table 3.3) and are filtered out as outliers. | 92 |
| 3-20 | As in Figure 3-17, but for the scaling of the ratio of r_e to r_{ew} . Positive slope indicates that the eye is expanding relative to the width of the eyewall. | 93 |
| 3-21 | As in Figure 3-17, but for the scaling of r_0^* with the Rossby deformation radius. | 95 |
| 3-22 | Left: Time-evolution of the radial profile of the full azimuthal wind speed at $z = 1.5 km$ for a dry version of the Control simulation. Right: Time-mean radial wind profile averaged over days 100-130. | 97 |

| | | |
|------|---|-----|
| 3-23 | Equilibrium radial profiles of the gradient wind for simulation sets varying C_k (left) and C_d (right), where $\frac{V_p}{fl_h}$ has been held constant across all simulations. Shading reflects potential intensity from low (light grey) to high (black). | 99 |
| 3-24 | As in Figure 3-23, but with radial profiles normalized as follows: V by V_m and r by r_{ew} | 100 |
| 3-25 | Scaling between $\frac{V_m}{V_p}$ and $\frac{C_k}{C_d}$ in simulations (marker) and the theoretical scaling relation given by Eq. (3.25) (line) from Emanuel and Rotunno (2011) for varying C_k (black, x) and C_d (grey, diamond). The horizontal mixing length, l_h , is varied such that the non-dimensional parameter $\frac{V_p}{fl_h}$ remains fixed at its Control value. For each exchange coefficient, best-fit scaling constants and 95% confidence intervals are listed at the top and adjusted r-square values are listed in the lower-left corner. | 101 |
| 3-26 | Scaling of r_{ew} with the ratio of exchange coefficients, $\frac{C_k}{C_d}$, for varying C_k (black, x) and C_d (grey, diamond). Best fit scaling exponents with 95% confidence intervals are listed in the lower-right corner, and adjusted r-square values are given in the top-left corner. | 102 |
| 3-27 | Scaling of the ratio of r_e to r_{ew} with C_d . Best fit scaling exponents with 95% confidence intervals are listed in the lower-right corner, and adjusted r-square values are given in the top-left corner. | 103 |

3-28 As in Figure 3-11, but for simulations varying C_k and C_d while holding $\frac{V_p}{f l_h}$ fixed to its Control value. Radial profiles of error in the fit of the analytical outer wind model (Eq. (3.18), empirically modified with $c = .3$) to the equilibrium radial wind profile, defined as $V_{E04} - V_{CM1}$, for all simulations varying each of the six relevant dimensional parameters. Error profiles are smoothed with a 10-pt smoother. In the top four panels, shading reflects potential intensity from low (light grey) to high (black); in the bottom two panels, shading reflects parameter magnitude from low (light grey) to high (black). Analytical model is fit to $r(.75V_m)$, with the range $r(.75V_m < V < .1V_m)$ solid and $r(V < .1V_m)$ dashed; radii are normalized by r_0 calculated using the outer wind model. Red line depicts mean error over the inner range, and the corresponding mean absolute error (MAE) for the simulation set is listed in the top left corner. 105

3-29 As in Figure 3-26 but for r_0^* 106

3-30 Scaling of $\frac{\widetilde{r_m}}{r_0^*}$ with $\frac{C_k}{C_d}$ in simulations (marker) with linear fit (dashed) and the theoretical scaling relation given by Eq. (3.29) (solid) from Emanuel and Rotunno (2011) for varying C_k (black, x) and C_d (grey, diamond). The horizontal mixing length, l_h , is varied such that the non-dimensional parameter $\frac{V_p}{f l_h}$ remains fixed at its Control value. For each exchange coefficient, best-fit scaling constants and 95% confidence intervals are listed at the top. 107

4-1 Snapshots of the distribution of the full wind speed [ms^{-1}] at $z = 1.5 km$ for PI43 (top left, day 47.75), CTRL (top right, day 38.5), PI108 (bottom left, day 69.62), and FX2 (bottom right, day 47.88). White dots mark objectively-identified TC centers. Image size scales with domain size such that length scales are preserved. 125

| | | |
|-----|--|-----|
| 4-2 | Snapshot of windspeed (color) at day 100 and accumulated precipitation over days 98-100 (white contour, 2 <i>cm</i> interval) for four small-domain RCE simulations in which the rotation rate and domain size are varied (respective values listed above each plot). Horizontal resolution is 4 <i>km</i> in all cases. | 129 |
| 4-3 | Cross-section of the magnitude of the wind speed between the centers of the two dominant TCs in the lower half of the domain of the PI43 snapshot (Figure 4-1, top-left panel). | 130 |
| 4-4 | Probability distributions for V_m (top left), r_{ew} (top right), r_0 (bottom left), and r_0^* (bottom right) for all four simulations. Median values plotted (dashed line, marker) and listed in the top left corner of each plot. Shading denotes potential intensity from low (light) to high (dark).131 | 131 |
| 4-5 | As in Figure 4-4, but with V_m non-dimensionalized by V_p and radii non-dimensionalized by $\frac{V_p}{f}$ | 133 |

List of Tables

| | | |
|-----|--|-----|
| 3.1 | Parameter values for the Control simulation. The parameters l_h and l_v correspond to the horizontal and vertical mixing lengths, respectively, in the turbulence parameterization; H_{domain} is the height of the model lid; L_{domain} is the radius of the outer wall in the axisymmetric model. | 59 |
| 3.2 | Parameter values for each simulation used to test the scaling relationships associated with Eq. (3.12), where $C_1 = \frac{V_p}{fl_h}$. Control values are listed in Table 3.1. | 75 |
| 3.3 | Optimized c for each simulation (see text for details); corresponding histogram is plotted in Figure 3-10. Asterisk denotes a likely outlier. | 77 |
| 3.4 | Simulations varying either C_k or C_d and the corresponding values for the potential intensity and for the value of the horizontal mixing length used in order to fix $\frac{V_p}{fl_h}$ to its Control value. | 98 |
| 3.5 | As in Table 3.3, but for C_k and C_d , with $C_1 = \frac{V_p}{fl_h}$ held fixed at its Control value. | 104 |
| 4.1 | Parameter values for the 3D Control simulation. See text for details. | 122 |
| 4.2 | Parameter values for each experiment. N denotes the average number of storms extracted by the algorithm at each time step, and T denotes the length of the statistical equilibrium period over which statistics are accumulated. | 123 |

Chapter 1

Introduction

1.1 Motivation

1.1.1 Scientific

What sets the size of a tropical cyclone? Though seemingly a basic question, it remains largely unanswered in the field of tropical meteorology, despite over three decades of remarkable progress elucidating the dynamics of tropical cyclones (TCs). Indeed, the fundamental air-sea interaction instability that underlies their existence has been identified and placed within the context of a more general theory of tropical cyclones as a Carnot heat engine (Emanuel, 1986). The interaction of the TC with its environment has been studied in great detail, particularly the role of vertical wind shear and the associated time-dependent dynamics of TC intensification, which has been successfully incorporated into this Carnot engine framework (Tang and Emanuel, 2010). Furthermore, both theory and relatively simple dynamical models (Ooyama, 1969; Emanuel, 1995a; Rotunno and Emanuel, 1987) can reproduce the characteristic features of mature tropical cyclones, including maximum wind speed, central sea level pressure, and thermodynamic structure. Yet despite such tremendous scientific progress, as well as widespread recognition of the strong sensitivity of both storm surge (Irish et al., 2008) and wind damage (Iman et al., 2005) to storm size, size remains largely unpredictable.

As a simple motivating example, Figure 1-1 displays a visible satellite image of the tropical Atlantic ocean basin taken on 16 September 2010 from the GOES-East satellite. Three TCs are identifiable: Karl in the Gulf of Mexico, Igor in the western Atlantic, and Julia in the central Atlantic. Though each exhibits similar qualitative cloud structure, characterized by a circular central dense overcast (including an eye in the cases of Julia and Igor) surrounded by wispy bands of clockwise-rotating cirrus within the outflow, this structure manifests itself at distinct horizontal length scales for each storm. Indeed, at 1200 UTC on the 16th, the mean radius of 34-kt winds (r_{34kt}), as recorded in the National Hurricane Center Extended Best Track database (Demuth et al., 2006), was 95 km for Karl, 194 km for Julia, and 389 km for Igor – i.e. a near-exact doubling in size moving from small to medium and again from medium to large.

Given that the storms are at nearly identical latitudes (Karl: 19.6N; Julia: 21.8N; Igor: 20.8N), their distinct sizes cannot be attributed to variations in the ambient rotation rate. Nor can their distinct sizes be attributed to variations in peak wind speed, as Julia (90 kt) and Igor (120 kt) are of comparable intensities and, 24 hours later, Karl intensifies to 110 kt while its mean r_{34kt} expands only slightly to 139 km. Finally, the differences likely cannot be attributed to variations in potential intensity, whose approximate September climatological value (1982-1995; Source: <http://wind.mit.edu/~emanuel/pcmin/climo.html>) is largest for Karl (175 kt) and slightly smaller for Igor (160 kt) and Julia (140 kt); sea surface temperature anomalies, which may be used as a proxy for local anomalies in the potential intensity, are only significant for Julia (+1 K; Source: NOAA NCDC <http://www.ncdc.noaa.gov/oa/climate/research/sst/weekly-sst.php>).

Clearly, storm size is an enigma, one that defies conventional intuition.

1.1.2 Societal

In addition to the fundamental scientific motivation for understanding TC size, there exists tremendous societal motivation as well. Landfalling U.S. hurricanes are responsible for seven of the top ten costliest insured property losses due to natural disaster

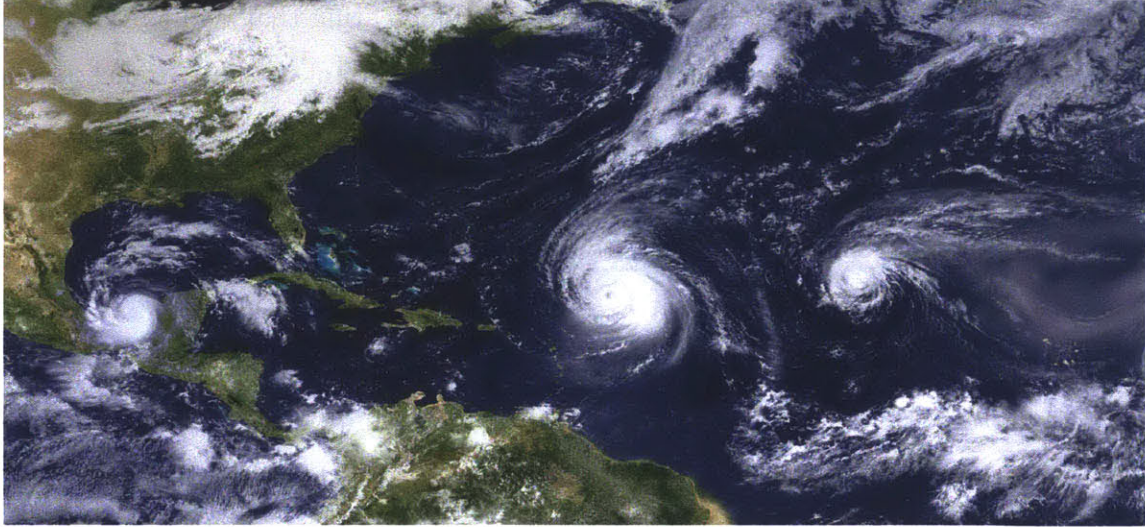


Figure 1-1: Visible satellite image of the tropical Atlantic ocean basin from the GOES-East satellite taken on 16 September 2010 at 1445 UTC. Three TCs of very different sizes are identifiable: Karl (small) in the Gulf of Mexico, Igor (large) approaching the Caribbean, and Julia (medium) in the central Atlantic. Source: http://upload.wikimedia.org/wikipedia/commons/d/d5/20100916-1845UTC-GOES-East_visible.jpg.

worldwide since 1980 (Munich Re, 2011). Despite a projected decrease in the overall number of hurricanes globally, the potential for increases in the frequency and intensity of the strongest hurricanes due to climate change (Knutson et al., 2010) has raised concerns about similar increases in total economic damage in the future (Mendelsohn et al., 2012; Peduzzi et al., 2012). Moreover, 50% of damages due to hurricanes in the United States during the period 1870-2005, normalized for changes in population, wealth, and inflation, was caused by only eight storms (Pielke Jr. et al., 2008), highlighting the fact that U.S. economic damage by TCs is a fat-tailed phenomenon (Katz, 2012), though recent work argues that this tail behavior is linked primarily to that of the distribution of coastal economic value itself (Chavas et al., 2013).

For the purposes of risk assessment and emergency management, it is desirable to explain the observed variability in economic damage in terms of the characteristics of the storms themselves and their associated wind, storm surge, and rainfall hazards. Historically, studies have sought relationships between damages and the maximum wind speed. These relationships are typically found to follow power laws whose scal-

ing exponents range from 3 to 9 (Pielke Jr., 2007), indicating that damages increase very rapidly with wind speed. However, a significant amount of the variance in the historical damage database cannot be explained by variations in peak wind speed alone. More recent research has begun to appreciate the importance of storm size in modulating damage as well, as larger storms have a larger area of wind and rainfall exposure and are capable of generating higher storm surge. Irish and Resio (2010) demonstrated that storm surge is a complex function of multiple variables associated with storm track and structure as well as landfall location, but of particular importance are storm size and the slope of the local continental shelf; the latter has been found to be useful in explaining variability in tail of the U.S. damage distribution (Chavas et al., 2013).

Indeed, the modulation of storm surge by storm size can have devastating consequences, as demonstrated by the contrast between Hurricanes Camille (1969) and Katrina (2005), both of which made landfall near New Orleans, LA. Figure 1-2 displays the 1-minute sustained surface wind fields of each storm just prior to landfall, as analyzed by the NOAA Hurricane Research Division H*Wind Project (Powell et al., 1998). Although Camille was a much more intense storm, with a peak 1-minute sustained wind speed of 165 kt (Category 5 on the Saffir-Simpson scale), as compared to Katrina (113 kt; Category 3), Katrina's radius of maximum wind (48 km) was twice as large as that of Camille. Consequently, Katrina's peak recorded storm surge (8.5 m) was 1.6 m higher than that generated by Camille (6.9 m). The resulting societal impacts were drastically different: Katrina's storm surge breached the local levee system, submerging much of the city of New Orleans. Ultimately, Katrina killed at least 1833 people and caused an estimated \$81 billion (USD 2005) as compared to 259 fatalities and an estimated \$23 billion (USD 2005) caused by Camille (Pielke Jr. et al., 2008). Though the latter case is still undoubtedly terrifying, the large disparity in outcome is primarily attributable to the difference in storm size.

A second, straightforward example of the role of storm size in causing damage is Hurricane Sandy in 2012, which killed 72 people and caused an estimated \$50 billion (2012 USD) in damage within the United States, making it the sixth-costliest U.S.

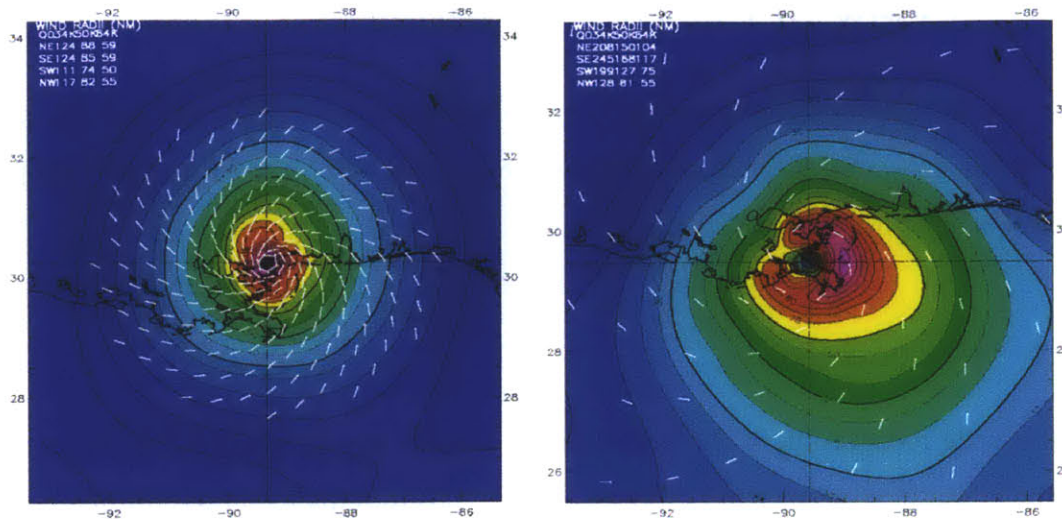


Figure 1-2: Estimated 1-minute sustained surface wind fields of Hurricanes Camille (1969; left) and Katrina (2005; right) just before landfall near New Orleans (NOAA Hurricane Research Division H*Wind Project, Powell et al. (1998)). At the times shown, their respective peak 1-minute sustained wind speeds were 165 kt and 113 kt and radii of maximum wind were 24 km and 48 km.

hurricane landfall in history after normalizing for inflation and changes in population and wealth (Blake et al., 2013). Such tremendous destruction occurred despite the fact that Sandy’s peak sustained wind speed at landfall was a mere 70 kt, barely surpassing the threshold for designation as a hurricane (64 kt). Instead, Sandy was one of the largest TCs¹ ever recorded in the Atlantic basin, with an estimated radius of gale force wind of $r_{34kt}=1610$ km at landfall. Sandy’s large size enabled the storm to generate tremendous storm surge along the New Jersey and New York coastlines, inundating a significant fraction of New York City (peak surge of 9.23 ft at the Battery), and its enormous wind field left a large swath of destruction and cut power to millions of people for up to two weeks across the Northeast. Clearly, in the case of Sandy, storm size rather than peak wind speed was the dominant factor modulating total economic damage.

¹Sandy was in fact no longer a pure tropical cyclone at landfall, as it was beginning to undergo extra-tropical transition.

1.2 Review of existing research

To date, relatively little research has been performed to investigate the factors underlying storm size variability. Here we review the existing literature from the standpoint of observations, modeling, and theory.

1.2.1 Observations

Despite wide recognition of the importance of storm size in determining storm surge and the spatial extent of wind damage, size in nature remains largely unpredictable. In the absence of land interaction, the horizontal extent of the outer circulation is observed in nature to vary only marginally during the lifetime of a given tropical cyclone prior to recurvature into the extra-tropics, but significant variation exists from storm to storm, spanning a wide range of values from ~ 100 -2000 km, regardless of basin, location, and time of year (Merrill, 1984; Frank, 1977; Chavas and Emanuel, 2010; Cheng-Shang et al., 2010). For example, the radius of gale force wind (r_{34kt}) was only 19 km for Tropical Storm Marco in the North Atlantic basin in 2008 (Demuth et al., 2006), whereas this radius reached a maximum of 1110 km for Super Typhoon Tip in the West Pacific basin in 1974 (Dunnavan and Diercks, 1980). Size is found to correlate only weakly with latitude and intensity (Merrill, 1984; Weatherford and Gray, 1988; Chavas and Emanuel, 2010; Chan and Chan, 2012), as the outer and inner core regions appear to evolve nearly independently. Characteristic storm sizes are typically 30-50% larger in the Pacific than in the Atlantic (Merrill, 1984; Liu and Chan, 1999), perhaps a consequence of the existence of large gyre TCs originating from monsoon depressions (Cocks and Gray, 2002). Similarly, Kimball and Mulekar (2004) determined from Atlantic Extended Best Track data that as a storm intensifies the radius of outermost closed isobar (r_{OCI}) remains approximately constant despite changes in the radial structure of the intermediate wind field. Moreover, they found that the radius of maximum winds (r_m) and intermediate wind radii are smaller, but r_{OCI} is larger, in Gulf of Mexico storms relative to North Atlantic storms at comparable latitude.

In terms of the relationship between storm size and the synoptic-scale environment, Quiring et al. (2011) combined the Extended Best Track and NCEP/NCAR Reanalysis datasets but find minimal useful predictors for r_m or r_{34kt} , with the exception of a slight positive correlation between mid-level relative humidity and r_m . Liu and Chan (2002) analyzed synoptic-scale weather patterns associated with Western North Pacific TCs of different sizes and found that small TCs typically form within ridge and monsoon-gyre patterns. Indeed, the West Pacific monsoon can develop a large gyre circulation that generates midget tropical cyclones on its periphery and, on occasion, the entire circulation subsequently evolves into a very large TC (Lander, 1994). Finally, TCs are known to expand during the process of extra-tropical transition (Hart and Evans, 2001; Evans and Hart, 2003; Elsberry, 1995), though the underlying mechanisms of this dynamic process are still an active area of research.

From a broader perspective, Merrill (1984) found that frequency distributions of r_{OCI} in the Atlantic and Western North Pacific are qualitatively log-normal, though no formal statistical test was performed. Dean et al. (2009) found that the distribution of storm size, defined as the radius of vanishing winds divided by the ratio of the potential intensity to the Coriolis parameter, is close to log-normal in the Atlantic basin, though this analysis was based on the radius of gale force wind (r_{34kt}) taken from two datasets that employ very different methodologies and whose r_{34kt} values for overlapping cases disagree markedly. To improve upon this effort, Chavas and Emanuel (2010) analyzed QuikSCAT scatterometer data and found that the global distribution of r_0 is approximately log-normal, though distinct median sizes exist within each ocean basin, suggesting that the size of a given TC is not merely a global random variable but instead is likely modulated either by the structure of the initial disturbance, the environment in which it is embedded, or both.

1.2.2 Modeling

In addition to observational work, numerical modeling also provides insight into the underlying dynamics of TC size. Hill and Lackmann (2009) and Xu and Wang (2010) showed using the full-physics WRF and TCM-4 models, respectively, that TCs tend

to be larger when embedded in moister mid-tropospheric environments due to the increase in spiral band activity and subsequent generation of diabatic potential vorticity which acts to expand the wind field laterally, a result also corroborated by Braun et al. (2012) exploring the role of near-core dry air patches on TC development. Fudeyasu and Wang (2011) combined budget calculations based on output from TCM-4 with solutions to the Sawyer-Eliassen equation and concluded that diabatic heating associated with mid-upper-tropospheric stratiform anvil clouds outside the eyewall in active spiral rainbands generates a mid-tropospheric inflow that transports absolute angular momentum inward to spin up the outer-core circulation, while the azimuthal-mean diabatic heating rate in the eyewall (where it is largest) contributes minimally to this spin-up process due to the high inertial stability in the inner-core region. Using a simple three-layer axisymmetric model, DeMaria and Pickle (1988) found that storm size at peak intensity increased with increasing background rotation rate but was constant with increasing sea surface temperature, while Smith et al. (2011) found in a separate three-layer model an optimum in storm size as a function of rotation rate, which they attributed to the inhibitive effect of inertial stability on boundary-layer inflow as the rotation rate is increased. Finally, the seminal work of Rotunno and Emanuel (1987) found in an idealized axisymmetric framework a strong relationship between the horizontal length scales of the initial and mature vortex. Xu and Wang (2010) corroborate this result, noting an additional sensitivity to the time-evolution of storm size, as a small initial vortex leads to a much slower increase in the inner-core size with time due to the weak surface entropy fluxes beyond the eyewall and associated dearth of spiral rainband activity.

Beyond modeling of individual TCs, Held and Zhao (2008) explore the “tropical cyclone world” of rotating f -plane radiative-convective equilibrium and find that TC size scales inversely with f , in apparent qualitative agreement with a scaling with either the ratio of the potential intensity to the Coriolis parameter (Emanuel, 1986) or the Rossby deformation scale, though they could not distinguish between the two. No work has been done thus far to quantify storm size in global general circulation models.

1.2.3 Theory

Finally, extant theory offers insightful models for TC structure. First and foremost, the maximum wind speed is bounded by the potential intensity (Emanuel, 1986, 2010), V_p , given by

$$V_p^2 = \frac{C_k T_{sst} - T_{tpp}}{C_d T_{tpp}} (k_{sst}^* - k) \quad (1.1)$$

where C_k and C_d are the surface exchange coefficients of enthalpy and momentum, respectively, T_{sst} is the sea surface temperature, T_{tpp} is the outflow temperature near the tropopause, k is the enthalpy of the unperturbed boundary layer air, and k_{sst}^* is the saturation enthalpy at the sea surface temperature and pressure at the radius of maximum winds. Given that a TC can be viewed as Carnot heat engine that extracts heat at the warm surface and expels heat at the cold tropopause (Emanuel, 1986), this quantity can be derived from the balance between net production and net dissipation of energy in the system (Emanuel, 2003). Energy input is associated with two processes: surface fluxes of enthalpy, whose magnitude depends on the local wind speed and air-sea thermodynamic disequilibrium and is given by

$$F_k = C_k \rho |\mathbf{u}| (k_{sst}^* - k) \quad (1.2)$$

where \mathbf{u} is the near-surface wind speed, and sensible heating due to internal frictional dissipation within the boundary layer, given by

$$F_{diss} = C_d \rho |\mathbf{u}|^3 \quad (1.3)$$

The local net energy production is given by the sum of Eqs. 1.2 and 1.3 multiplied by the Carnot efficiency, $\frac{T_{sst} - T_{tpp}}{T_{sst}}$. The effect of including dissipative heating is simply to change the denominator in the Carnot efficiency from T_{sst} to T_{tpp} (Bister and Emanuel, 2002). Local net energy loss due to frictional dissipation is also given by Eq. 1.3, but absent any efficiency multiplier. Assuming that the radial integrals of each of these processes are dominated by their contributions at the radius of maximum winds, and approximating the full wind by its azimuthal component, V , one may equate

the integrands directly and arrive at Eq. 1.1. Overall, the potential intensity is a function of the local, undisturbed thermodynamic environment, and it has been shown to provide a credible bound on the peak intensity of real TCs in nature (Emanuel, 2000).

As for radial structure, Emanuel (2004) developed a complete radial profile as a patchwork of asymptotically-matched solutions for the eye, the convecting inner core, and the non-convecting outer circulation. They combine angular momentum balance in a simple slab boundary-layer model with the constraints imposed by the hypothesis of subcloud layer enthalpy quasi-equilibrium (Raymond, 1995) in the convecting inner region, and with the constraint that the Ekman suction rate at the top of the boundary layer must match the radiative subsidence rate in the lower free troposphere in the non-convecting outer region. The eye solution is assumed to be in near-solid body rotation with the given maximum wind speed and radius of maximum winds due to the fast time-scales of turbulent eddies in the eye, which rapidly transport angular momentum radially inwards (Emanuel, 1997; Smith, 1980).

More recently, Emanuel and Rotunno (2011) derived a full analytical solution for the radial structure of the axisymmetric azimuthal gradient wind at the top of the boundary layer, whose asymptotic solution is given by

$$V(r) = 2r \frac{r_m V_m + \frac{1}{2} f r_m^2}{r_m^2 + r^2} - \frac{1}{2} f r \quad (1.4)$$

where V_m is the maximum gradient wind speed, r_m is the radius of the maximum gradient wind speed, and f is the Coriolis parameter. Importantly, neither V_m nor r_m are free parameters, as V_m is a function solely of the ratio of the surface exchange coefficients and is given by

$$\frac{V_m}{V'_p} = \left(\frac{1}{2} \frac{C_k}{C_d} \right)^{\frac{\frac{1}{2} C_k}{2 - C_d}} \quad (1.5)$$

where V'_p is a nominal version of the potential intensity, V_p , that does not include dissipative heating and uses the environmental saturation entropy in lieu of its ambient boundary layer value. Meanwhile, r_m is defined relative to the outer radius

of vanishing wind ($V = 0$), r_0 , according to the analytical solution for the ratio of angular momentum at r_m to its value at r_0 , given by

$$\frac{M_m}{M_0} = \left(\frac{1}{2} \frac{C_k}{C_d} \right)^{\frac{1}{2 - \frac{C_k}{C_d}}} \quad (1.6)$$

where $M_m \approx V_m r_m$ and $M_0 = \frac{1}{2} f r_0^2$. This solution is based on the assumption that small-scale, mechanically-driven turbulence in the TC outflow fixes the Richardson number to its critical value, thereby defining the radial dependence of the outflow temperature along the tropopause. For a sub-critical, slantwise moist neutral vortex, the distribution of the outflow temperature leads directly to the radial distribution of entropy in the boundary layer and, through thermal wind balance, the radial distribution of the azimuthal winds at the top of the boundary layer.

However, this latest solution is defined relative to a single free parameter given by the outer radius, r_0 – an elegant representation of our collective ignorance on TC size. Indeed, though reasonable theoretical models for storm structure exist, they are necessarily imposed onto an overall radial length scale that itself lacks theoretical guidance. The lone exception to this statement lies within the original potential intensity theory of Emanuel (1986), which includes a scaling for the theoretical upper-bound on r_0 that is given by the ratio of the potential intensity to the Coriolis parameter, $\frac{V_p}{f}$, the derivation and physical insight for which we review here.

From the Carnot heat engine perspective, potential intensity theory assumes a balance between the net heat input into the system, ΔQ , and the work done by the system, W . The heat input is in the form of wind-speed-dependent surface fluxes of enthalpy into the boundary layer from the lower boundary, whose existence is owed to the ambient air-sea disequilibrium of a greenhouse climate (Emanuel, 1987), as well as dissipative heating in the boundary layer; heat is expelled radiatively at the cold tropopause. The work performed is primarily that required to maintain the vortex wind field against frictional dissipation, W_{bl} . However, the system must also do work to restore angular momentum in the outflow to its ambient value, W_{out} , in order to connect the outflow leg with the boundary-layer inflow leg and thus energetically

close the Carnot engine. This restoration is believed to occur via vertical transport of angular momentum by small-scale turbulence in the outflow (Emanuel and Rotunno, 2011). The full balance is given by

$$\Delta Q = W_{bl} + W_{out} \quad (1.7)$$

Thus, implicit in Eq. 1.7 is the fact that any outflow work necessarily detracts from the work available to power the boundary layer winds and thus weakens the equilibrium storm. The outflow work, W_{out} , is simply proportional to the change in kinetic energy required to return the angular momentum back to its original value, which, assuming the process occurs at large radii, gives

$$W_{out} \approx \frac{1}{2}f(M_0 - M) \quad (1.8)$$

If we approximate M with M_m , then combining Eqs. 1.8 and 1.6 results in

$$W_{out} \approx \frac{1}{2}f^2r_0^2 \left(1 - F \left(\frac{C_k}{C_d} \right) \right) \quad (1.9)$$

where $F \left(\frac{C_k}{C_d} \right)$ is given by the RHS of Eq. 1.6, thereby demonstrating that the outflow work is proportional to r_0^2 (i.e. the area of the storm) and thus a larger storm requires more work be performed in the outflow.

The manifestation of this size effect on the steady-state intensity of the vortex arises in the original potential intensity theory of Emanuel (1986), though it is more easily seen in a subsequent iteration of this theory. Eq. 20 of Emanuel (1995b) gives a non-dimensional relation for the central pressure perturbation, P_c ,

$$P_c \sim 1 - \frac{1}{4}r_0^2 \quad (1.10)$$

where r_0 has been non-dimensionalized by $\frac{\sqrt{\chi_s}}{f}$ and $\sqrt{\chi_s}$ is a velocity scale equal to the potential intensity with $C_k = C_d$. This relation dictates that the central pressure perturbation vanishes for a sufficiently large storm relative to this theoretical

length scale. Moreover, this length scale is employed to non-dimensionalize radius in Emanuel (1989) and Emanuel (1995a) and thus is viewed as a “natural” length scale for a TC.

1.3 Defining storm size

There are a variety of metrics to which the term “size” refers, often to great confusion. Operationally, the common size radii are the radius of maximum wind (r_m), the radii of 64, 50, and 34 kt wind (r_{64kt} , r_{50kt} , r_{34kt} , respectively), and the radius of outermost closed isobar r_{OCI} . However, as noted earlier, the inner core, typically encompassing r_m and r_{64kt} and perhaps r_{50kt} , and the outer circulation, typically encompassing r_{34kt} and r_{OCI} , tend to evolve independently of one another, with the latter more stable in time during the lifetime of a TC.

Here we use the term “size” to refer to a measure of the broad outer circulation of the storm, and we formally define size as the outer radius, r_0 , where the radial wind profile vanishes, following theoretical convention given by the combination of Eqs. 1.4 and 1.6 as well as in earlier versions of potential intensity theory (e.g. Emanuel (1986)). Though less tangible operationally, r_0 is the relevant theoretical free parameter in need of constraint. Moreover, r_0 represents a universal metric of size that is independent of any specific choice of wind speed, whether dimensional (e.g. r_{34kt}) or non-dimensional (e.g. radius of 50% of the maximum wind speed), whose radius is used as a basis for comparison across storms.

1.4 Objectives

This work seeks to build upon the small base of existing research on TC size by characterizing the distribution of size in nature and exploring the determinants of equilibrium size in radiative-convective equilibrium, the simplest representation of a tropical atmosphere. Chapter 2 describes the creation of a climatology of tropical cyclone size based on QuikSCAT scatterometer data. Chapter 3 explores the

modulation of tropical cyclone size and structure by dimensional parameters and surface exchange coefficients in an idealized state of axisymmetric radiative-convective equilibrium. Chapter 4 explores tropical cyclone size in an identical thermodynamic environment but in three dimensional “tropical cyclone worlds”. Finally, Chapter 5 concludes with a synthesis of key findings and discussion across all chapters and explores the many opportunities for future work.

Chapter 2

A QuikSCAT Climatology of Tropical Cyclone Size

©American Geophysical Union 2010¹

2.1 Introduction

In the absence of land interaction, the horizontal extent of the outer circulation of a tropical cyclone (TC) is observed in nature to vary only marginally during the lifetime of a given TC prior to recurvature into the extra-tropics (Merrill, 1984; Frank, 1977), but significant variation exists from storm to storm, regardless of basin, location, intensity, and time of year. Kimball and Mulekar (2004) determined from Atlantic Extended Best Track data that as a storm intensifies the radius of outermost closed isobar (ROCI) remains approximately constant despite changes in the radial structure of the intermediate wind field. More recently, modeling work by Hill and Lackmann (2009) and Wang (2009) showed that TCs tend to be larger when embedded in moister mid-tropospheric environments due to the increase in spiral band activity and subse-

¹Permission to use figures, tables, and brief excerpts from this chapter in scientific and educational works is hereby granted provided that the source is acknowledged: Chavas, D. R., and K. A. Emanuel (2010), A QuikSCAT climatology of tropical cyclone size, *Geophys. Res. Lett.*, 37, L18816. Figures 2-3, 2-4, and 2-5 and additional discussion in Section 2.4.4 have been added to the original publication text for the purposes of the presentation herein. Additionally, a few minor text edits from the original publication were made for the purpose of clarification.

quent diabatic generation of potential vorticity which acts to expand the wind field laterally.

From a broader perspective, Merrill (1984) found frequency distributions of ROCI in the Atlantic and Western North Pacific that qualitatively resemble log-normal distributions. Dean et al. (2009) [hereafter *D09*] found that the distribution of normalized storm size, defined as the radius of vanishing winds divided by the ratio of the potential intensity to the Coriolis parameter, is close to log-normal in the Atlantic basin. However, the result of *D09* is based on the radius of gale force winds (R34) taken from two datasets that employ very different methodologies and whose R34 values for overlapping cases disagree markedly.

Ideally, one would prefer to characterize the size distribution based upon direct surface wind measurements taken from a single, consistent source. Thus, this work examines the global distribution of TC size, defined here as the radius of vanishing winds, using an independent, high-resolution dataset generated by the QuikSCAT satellite microwave scatterometer. The following sections outline the data and methodology used to generate a climatology of TC size, discuss its characteristic values and distribution, and explore the intra-storm evolution of size.

2.2 Data

Ocean near-surface (10m) wind vector data are taken from the QuikSCAT Level 2B dataset on a 12.5 km x 12.5 km grid for the period beginning July 19, 1999 (the start of the satellite's operational life) through December 31, 2008; this dataset is available at http://podaac.jpl.nasa.gov/DATA_CATALOG/quikscatinfo.html. Owing to rain contamination of the signal, QuikSCAT data quality is highest away from strong precipitation, and the instrument is considered very accurate in the range 3–20 ms^{-1} (NASA Jet Propulsion Laboratory, 2010); Chou et al. (2010) found RMS differences between QuikSCAT wind speeds and dropwindsonde data of 2.6 ms^{-1} . For a complete discussion of potential errors, see Hoffman and Leidner (2005).

Tropical cyclone 6-hourly location and intensity data are taken from the National

Hurricane Center HURDAT Best Track database (Jarvinen et al., 1984). For calculation of the normalization factor, $\frac{PI}{f}$, which is the natural tropical cyclone length scale (Emanuel, 1986), potential intensity values are taken from monthly mean re-analysis data (Bister and Emanuel, 2002) bi-linearly interpolated to the storm location.

2.3 Methodology

2.3.1 Locating TCs

To create a climatology of tropical cyclones as seen by QuikSCAT, Best Track location and intensity (V_{BT}) data are spline interpolated iteratively forward until reaching the minimum distance, d , to any valid (i.e. non-rain-flagged) QuikSCAT datapoint of a given pass. Cases for which $d > 100 \text{ km}$ or the interpolated intensity $V_{BT} \leq 17.451 \text{ ms}^{-1}$ are skipped.

Next, to identify the TC center of circulation we take as a first guess the interpolated Best Track location, about which we extract all data (including rain-flagged) within a $4^\circ \times 4^\circ$ box. All TC centers are then subjectively identified based on the full QuikSCAT wind vector field in this box. Only those cases for which there exists a single, clearly-defined center of cyclonic circulation are included, based upon the criteria that a) the center is consistent with the wind vectors in the immediate vicinity in all directions, and b) the broad “outer” circulation (i.e. 1-4 degrees from center) is easily discernible and is consistent with the location identified by criterion (a). The authors sought to be conservative in this procedure; when ambiguous, the case was omitted. All data within 2500 km of the center are then used for subsequent analysis.

Only cases over water and for which the potential intensity $PI > 40 \text{ ms}^{-1}$ are included in order to avoid cases in which storms are rapidly transitioning to regions of cold sea surface temperatures where mature tropical cyclones cannot be sustained. The TC translation vector, calculated directly from the full spline interpolation of the Best Track dataset, is then subtracted from all wind vectors. All vectors are projected onto their pure-azimuthal component relative to the TC center and vector

magnitudes are signed: positive for cyclonic, negative for anti-cyclonic. Lastly, wind speeds are azimuthally-averaged within 10-km wide rings moving radially outward from center to obtain a radial wind profile for each TC fix.

Finally, we select a single azimuthal-average wind speed, V_{QS} , and for each TC fix determine its radius, r_{QS} , and extrapolate outward to r_0 using a theoretical model of outer wind structure that assumes minimal deep convection in the outer region. This model is described in detail in Emanuel (2004) and is reviewed below.

2.3.2 Selecting V_{QS}

Selection of an optimal QuikSCAT wind speed, V_{QS} , necessitates balancing three key constraints. First, the assumption of constant background flow, represented by the single translation vector subtracted from all points, loses validity far from center; this constraint renders any effort to extract r_0 directly from the QuikSCAT data invalid. Second, the number of data points increases dramatically as one moves outward from the TC center. Finally, Brennan et al. (2009) found that QuikSCAT observed winds have a near-zero bias due to rain in the range of 10-15 ms^{-1} . The validity of a given azimuthal-average wind speed depends on the trade-offs between the above three factors. Based on these criteria we set $V_{QS} = 12 ms^{-1}$.

The final result is a dataset of 2154 TC fixes spread across five basins: Atlantic (482), East Pacific (367), West Pacific (640), Indian Ocean (78), and Southern Hemisphere (587).

2.3.3 Estimating Outer Radius r_0

To estimate the outer radius, r_0 , we employ the outer wind structure model derived in Emanuel (2004) (for an abridged form, see *D09*) to extrapolate radially outwards from the QuikSCAT-defined azimuthal-average radius, r_{QS} , of the wind speed V_{QS} described above. Here, we briefly review the model's characteristics. The flow is assumed to be steady and axisymmetric. The model assumes that there is no deep convection beyond r_{QS} , resulting in a local balance between subsidence warming and

radiative cooling. Furthermore, given that both the lapse rate and the rate of clear-sky radiative cooling are nearly constant in the tropics, the equilibrium subsidence velocity, w_{rad} , can be taken to be approximately constant. In equilibrium, this subsidence rate must match the Ekman suction rate into the boundary layer in order to prevent the creation of large vertical temperature gradients across the top of the boundary layer. The radial profile of azimuthal velocity is therefore determined as that which provides the required Ekman suction, and is given by

$$\frac{\partial(rV)}{\partial r} = \frac{2r^2 C_D V^2}{w_{rad}(r_0^2 - r^2)} - fr \quad (2.1)$$

where r is the radius, V is the azimuthal wind speed, f is the Coriolis parameter, C_D is the bulk aerodynamic drag coefficient. We set $C_D = 10^{-3}$ and $w_{rad} = 1.6 \text{ cm s}^{-1}$.

To our knowledge, this nonlinear first order differential equation has no analytical solution. *D09* neglected the partial derivative term to derive a simple analytical solution for r_0 . However, (1) can also be solved numerically for r_0 , and the solution to the full equation is 30-150 km larger than the approximated solution over the typical range of tropical latitudes and r_{QS} values (not shown). Thus, for our purposes we elect to use the full numerical solution.

2.4 Results

2.4.1 Basic statistics

Figure 2-1a displays the median radius of 12 ms^{-1} , r_{12} , and r_0 values and the standard deviation of r_0 both globally and by basin.

The global median outer radius is 423 km and ranges from a minimum of 341 km in the East Pacific to a maximum of 488 km in the West Pacific. The standard deviation of r_0 is 168 km and scales across basins in a similar fashion to the median value. The median distance between r_{12} and r_0 is 226 km. These values compare reasonably well with those of previous studies (e.g. Merrill (1984)). Moreover, r_0 is relatively insensitive to variations in w_{rad} and C_D (assumed constant), with changes

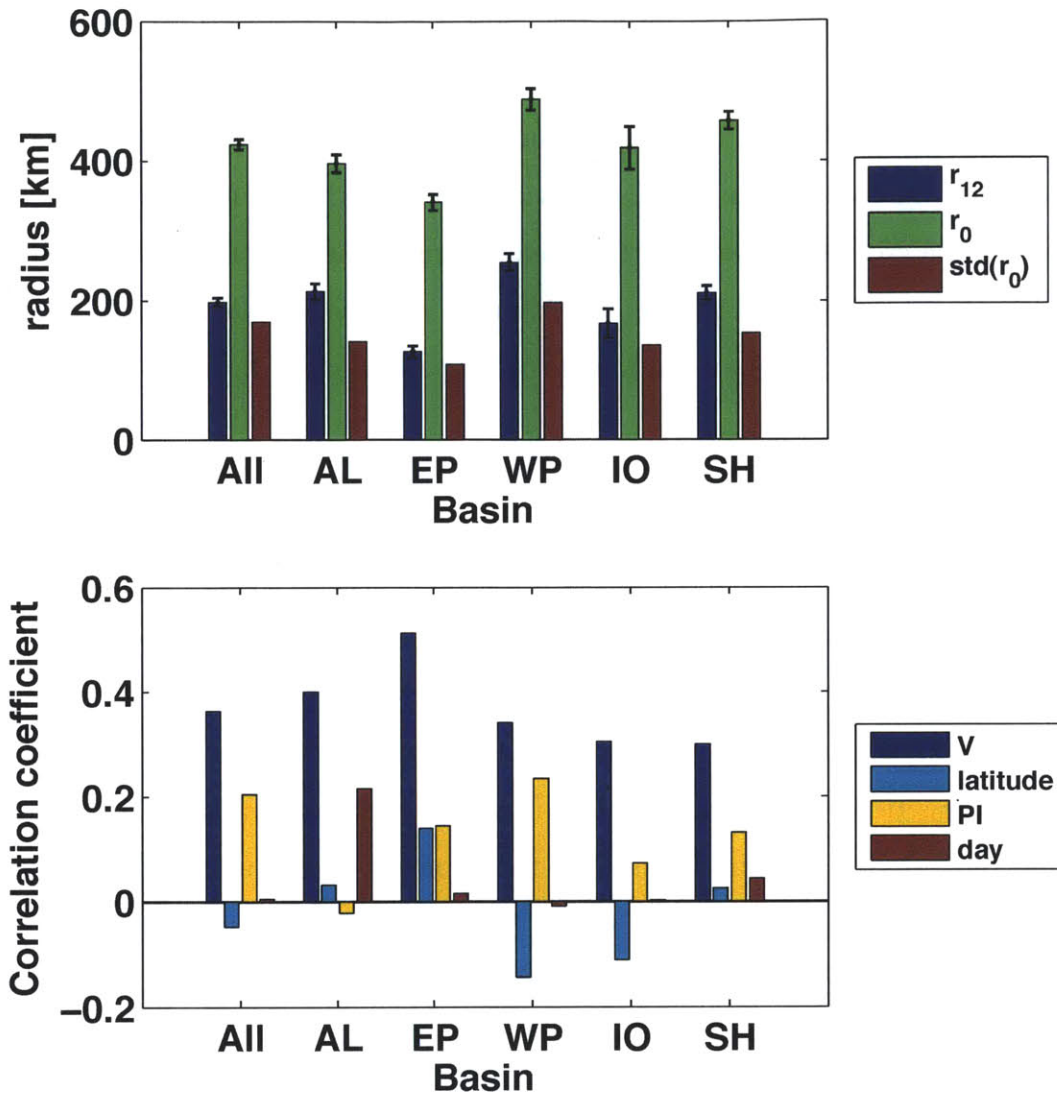


Figure 2-1: Top: Median values of r_{12} (blue) and r_0 (green) of r_0 (red) globally and by basin. All units in [km]. Error bars denote range of two standard deviations from the mean. Bottom: Correlation coefficients between r_0 and various parameters globally and across basins; “day” represents day of the hurricane season. Basins listed are Atlantic (AL), East Pacific (EP), West Pacific (WP), Indian Ocean (IO), and Southern Hemisphere (SH).

of approximately 25 km for the rather extreme cases of a halving or doubling of the ratio $\frac{C_D}{w_{rad}}$ for $\phi = 20^\circ$ and $r_{12} = 200$ km.

Figure 2-1b displays correlation coefficients between r_0 and various parameters of interest. The lone correlation of note exists between r_0 and intensity V ($r = .36$) and is relatively consistent across basins; this matches the weak correlation ($r = 0.28$)

found by Merrill (1984). Meanwhile, r_0 is effectively independent of latitude, which contradicts the typical finding that TCs tend to expand as they recurve poleward (e.g. Merrill (1984)).

2.4.2 Size distribution

Table 1 lists the p-values for the statistical fit to various distributions of $\log(r_{12})$, $\log(r_0)$, $\log(r_{12}^*)$, and $\log(r_0^*)$, where the asterisk denotes normalization by $\frac{PI}{f}$ following *D09*. All p-values are calculated using the Kolmogorov-Smirnoff test statistic. In the case of the normal and log-normal test distributions, the observed data were rescaled to have zero mean and unit variance for comparison to the standard normal parent distribution $N(0,1)$. P-values approaching unity indicate that the observed distribution is close to the parent distribution.

Table 1. Kolmogorov-Smirnoff p-values for statistical fits to various parent distributions for r_{12} , r_0 , r_{12}^* , and r_0^* . Log-normal refers to the normal fit of $\log(r)$.

Largest p-value is bold.

| Probability Distribution | r_{12} | r_0 | r_{12}^* | r_0^* |
|--------------------------|----------|-------------|------------|---------|
| Log-normal | .028 | .626 | .248 | .226 |
| Normal | 0 | 0 | 0 | 0 |
| Weibull | .001 | 0 | 0 | 0 |
| Rayleigh | 0 | 0 | 0 | 0 |
| Gamma | .05 | .11 | 0 | 0 |

The goodness of fit between the distribution of r_0 and a log-normal parent distribution is the most significant from among the variables and distributions tested here. The null hypothesis that r_0 is gamma distributed ($p = .11$) also cannot be rejected at the 95% confidence level, though based on a χ^2 metric ($p=.043$) it can be rejected.

For a direct comparison of r_{12} and r_0 , their global frequency distributions, along with the Gaussian fit to the mean and variance of the logarithm of each dataset, are displayed in Figure 2-2. Globally, $p = .028$ for r_{12} , which indicates that the null hypothesis of a log-normal distribution can be rejected at the 95% confidence

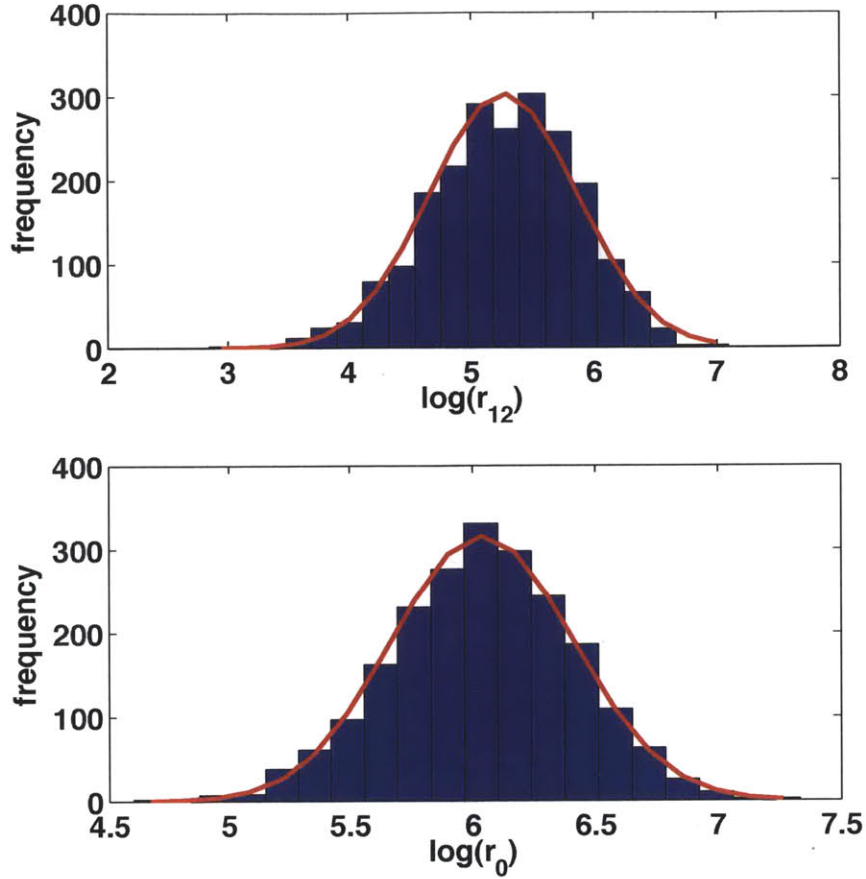


Figure 2-2: Global frequency distribution with Gaussian fit (red line). Top: $\log(r_{12})$; Bottom: $\log(r_0)$.

interval. On the other hand, $p = .626$ for r_0 , which indicates that the distribution is reasonably close to log-normal. Moreover, *D09* determined that normalization of r_0 by $\frac{PI}{f}$ results in a distribution that is much closer to log-normal. Our results indicate that the distribution of r_0 is significantly closer to log-normal than that of r_{12} , but that the subsequent normalization of r_0 in fact makes the log-normal fit worse. Though normalization does improve the fit for r_{12} , this may be understood in a crude mathematical sense given that $\log(\frac{r}{\frac{PI}{f}}) = \log(r) + \log(\frac{f}{PI})$. The distribution of $\frac{f}{PI}$ itself has a p-value of $p = .165$, which is greater than that of r_{12} but less than r_0 , and thus normalization would be expected to improve the fit for r_{12} but to reduce it for r_0 . In either case, the important result here is that normalization is not necessary to observe a size distribution that is relatively close to log-normal. These results are

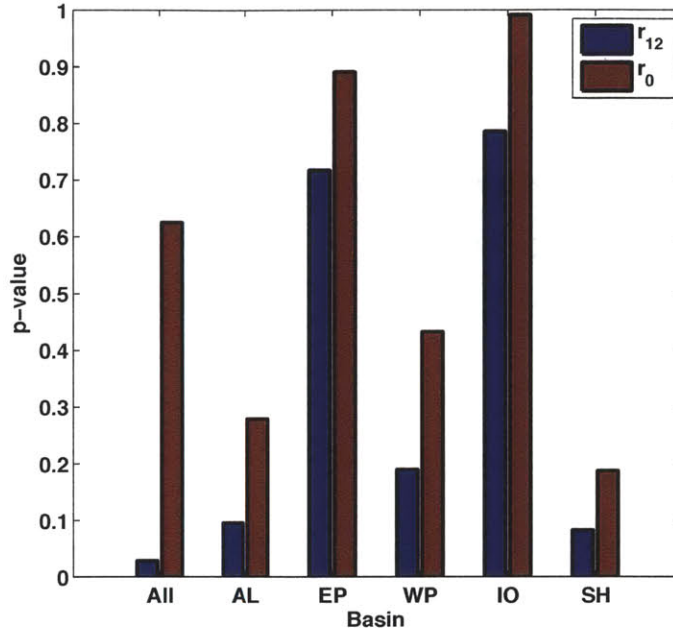


Figure 2-3: P-values for Gaussian fit to the distribution of $\log(r_{12})$ (blue) and $\log(r_0)$ (red) across basins.

found to be largely insensitive to the choice of V_{QS} over the range $8 - 15 \text{ m s}^{-1}$ (not shown). The findings are qualitatively similar within individual basins (Figure 2-3).

2.4.3 Control experiments

To what extent is this log-normal distribution an artifact of the outer wind structure model employed here? Given that our version of r_0 is only a function of r_{12} and f , we perform three test experiments. First, we recalculate r_0 using the observed distribution of f but set all values of r_{12} to be constant and equal to the median value, $r_{12} = 197.15 \text{ km}$, which results in a p-value of $p=.002$. Second, we recalculate r_0 using the observed distribution of r_{12} but set all values of f to be constant and equal to the median value, $f = 5 * 10^{-5} \text{ s}^{-1}$, which results in a p-value of $p=.222$.

Finally, we recalculate r_0 using the observed distribution of both r_{12} and f but randomly reshuffle their pairings, the purpose of which is to address the question of whether nature “matches” r_{12} and f in some optimal way as to generate a log-

normal distribution. For 100 runs, the p-value for the observed pairings of r_{12} and f is larger than approximately 80% of cases with randomized pairings, which suggests that, though not optimized, how r_{12} and f are paired in nature may play a role in bringing the distribution of r_0 closer to log-normal.

Taken together, these experiments indicate that, though a component of the observed distribution is simply due to the nature of the outer structure model chosen in this work, the actual distributions of r_{12} and f are also central to generating the log-normal distribution.

2.4.4 Intra-storm evolution

For the 241 distinct TCs with 4 or more QuikSCAT observations in the dataset used here, the mean intra-storm rate of change of r_{12} and r_0 , taken as the slope of the linear least-squares fit to the data, is 18.1 and 10.9 $km\ day^{-1}$, or approximately 9 and 2.5 % day^{-1} of the median value, respectively. The distribution for the case of r_0 is shown in Figure 2-4. The respective standard deviations are 43.1 and 53.2 $km\ day^{-1}$, indicating significant variance across individual storms; the distribution of rates of change is approximately Gaussian about the mean. Though relatively small, these mean expansion rates are statistically significantly different from zero at the 95% confidence interval ($p = 0$ and .002, respectively). A slow broadening of the wind field with time has also been noted in previous studies (e.g. Cocks and Gray (2002), Merrill (1984)).

Closer inspection reveals that much of this expansion appears to occur early in the storm's evolution. For the 215 distinct TCs whose first 4 observations occur within a 100 hour period, the expansion rate of r_{12} and r_0 over these first 100 hours is 24.0 and 18.7 $km\ day^{-1}$, respectively. Meanwhile, for the 35 distinct TCs with 4 or more observations at least 100 hours after the initial observation, the expansion rate beyond 100 hours declines substantially to 8.3 and $-0.8\ km\ day^{-1}$, respectively, neither of which are statistically significantly different from zero ($p = .28$ and .92). Significant variance exists, though, as standard deviations are 43.1 and 53.2 $km\ day^{-1}$, respectively. If the outer radius of a mature TC truly remains approximately constant

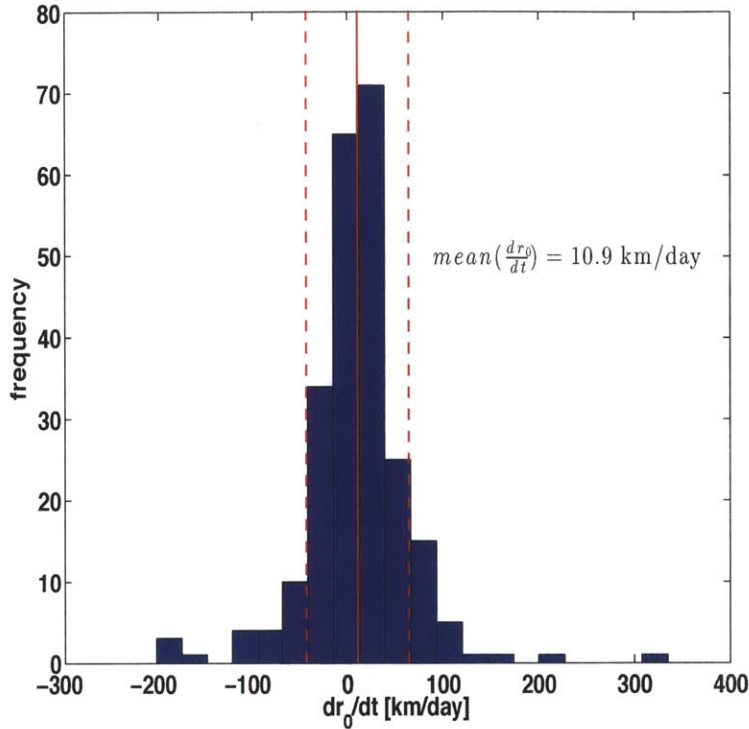


Figure 2-4: Distribution of $\frac{\partial r_0}{\partial t}$ for all storms with at least four observations. Red lines denote mean (solid) and one standard deviation (dashed) growth rates, with a mean value of 10.9 km day^{-1} .

with time, then this result may be an indication that our threshold minimum intensity of 17.5 ms^{-1} is capturing TCs at the tail end of the genesis process during which the outer radius has yet to reach its quasi-steady state, but further investigation is needed to validate such a claim.

Finally, there are six TCs that are observed at least 14 times during their lifespans, enabling a closer look at the evolution of storm size over the lifecycle of a few long-lived storms. Their time evolutions are plotted in Figure 2-5. In most cases the size of these storms remains quite steady in time. In particular, the red curve, which corresponds to the longest lived and most observed storm in the database (22 observations), stays at a remarkably constant size throughout its entire lifespan and at a value tantalizingly close to our global median value of 400 km . This subset appears to provide a convenient, representative sample of our collective knowledge of storm size evolution: during its lifecycle, a tropical cyclone typically does not change significantly

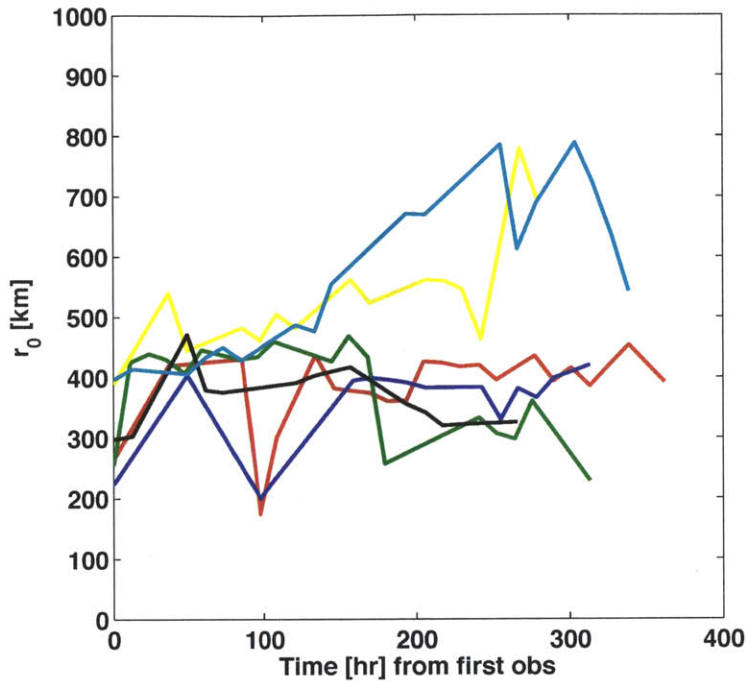


Figure 2-5: Time evolutions of r_0 for the six storms with at least 14 observations during their lifespans. Red line corresponds to the case with the most observations (22).

in size (red, black, green, blue), occasionally it grows gradually (cyan, yellow), but it rarely if ever contracts.

2.4.5 Case study: Alberto (2000)

The most-observed case (red) in Figure 2-5 corresponds to Hurricane Alberto (2000) in the Atlantic basin, whose lifecycle spanned the period August 3-25, 2000. Alberto was one of the top ten longest-lived storms in the Atlantic basin in recorded history (Beven, 2000). Alberto was a classic Cape Verde-type TC that developed from a strong African Easterly Wave (AEW; Thorncroft and Hodges (2001)) off the coast of West Africa that spent its entire life at sea. A map showing the track and evolution of Alberto is displayed in Figure 2-6.

During the course of its life-cycle, Alberto traversed a large range of latitudes. It first develops into a Tropical Depression at $11^\circ N$, begins to recurve poleward near

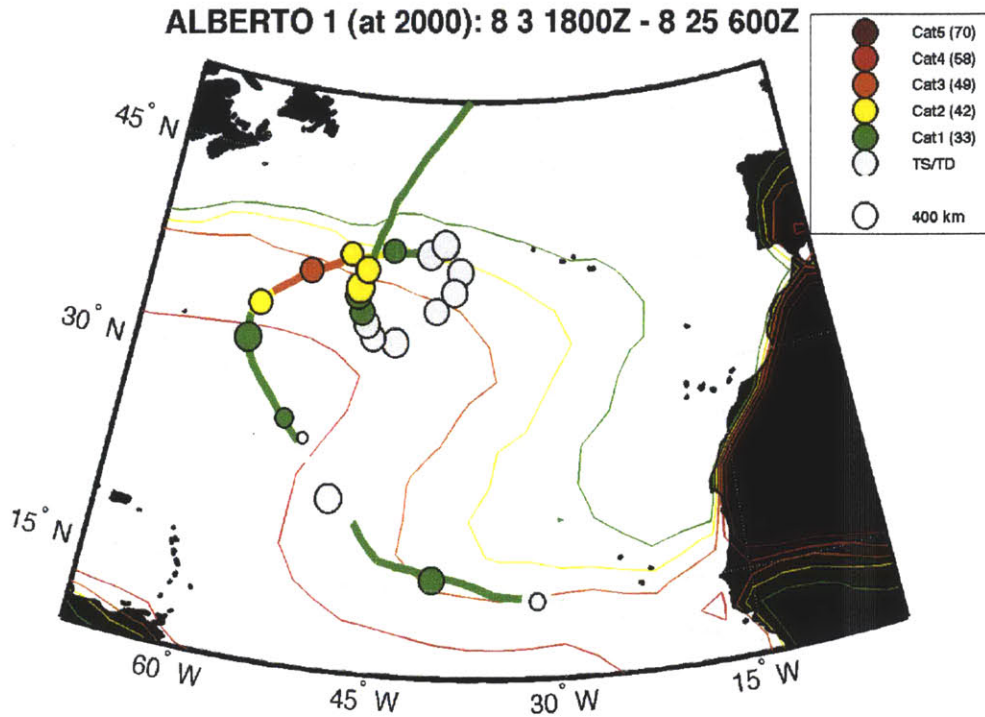


Figure 2-6: Map displaying the NHC Best Track and evolution of Hurricane Alberto (2000). Colors correspond to Saffir-Simpson category; maximum wind speeds from NHC Best Track database. Circles denote QuikSCAT observation, with marker size scaled by QuikSCAT-based estimate of r_0 (see legend). Contours denote climatological distribution of V_p for August (Bister and Emanuel, 2002).

$45^\circ W$, undergoes a large, 5-day anti-cyclonic loop between $33^\circ N$ and $39^\circ N$, and finally moves rapidly northward starting at 0600 UTC on 22 August. Importantly, Alberto was able to move a significant distance poleward before encountering extratropical disturbances, as extratropical transition was observed to begin only on the final leg of its track poleward of $45^\circ N$. Meanwhile, Alberto underwent three different periods of intensification to Hurricane status, the strongest of which allowed the storm to attain Category 3 status ($V_m = 110 \text{ kt}$) on 12 August. Figure 2-7 displays a time-series of the evolution of V_m , V_p , r_m , and r_0 . Data for r_m are taken from the Extended Best Track dataset (Demuth et al., 2006).

The stability of the size of Alberto throughout its lifecycle is remarkable given the significant variations in r_m , V_m , V_p and f that the storm endures. Alberto provides a clear example of the apparent independence of storm size from the variables typically

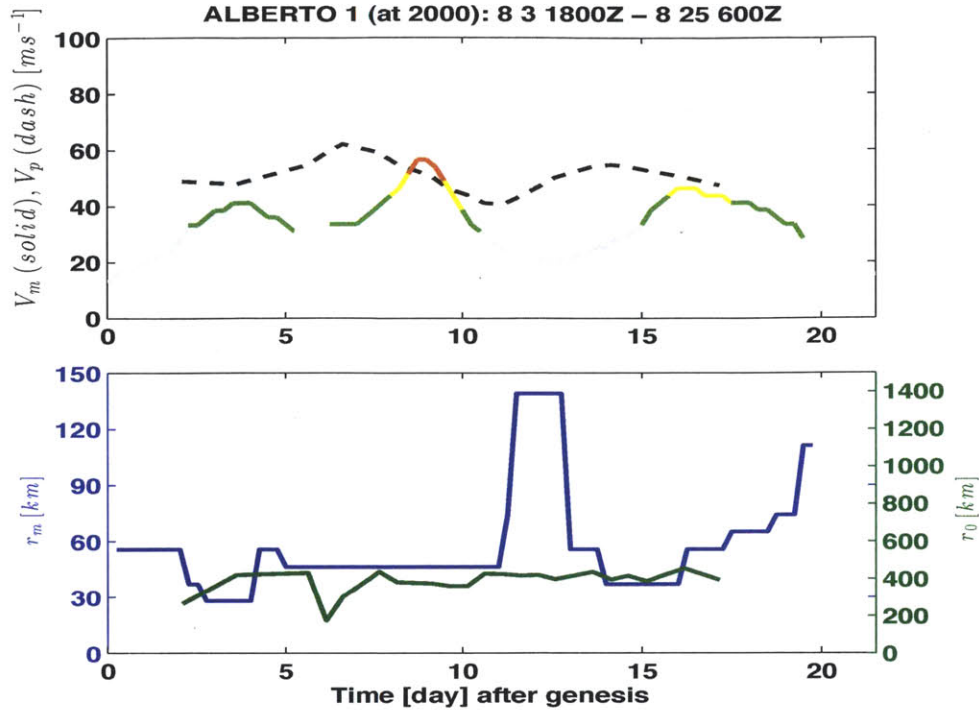


Figure 2-7: Time series of V_m and V_p (top), r_m and r_0 (bottom) for Alberto (2000). Colors for V_m correspond to Saffir-Simpson category as in Figure 2-6.

considered to be operationally-relevant to TC evolution, including both environmental parameters and characteristics of the inner-core of the storm. In particular, this case study provides anecdotal evidence that the increase in storm size with latitude during the life-cycle of a storm, which has been noted in previous observational studies (Merrill, 1984; Weatherford and Gray, 1988), may simply be the signal associated with those storms undergoing extratropical transition rather than any fundamental process associated with changes in f (indeed, equilibrium dynamics would predict a smaller storm at larger f , as discussed in Chapter 3). Though extratropical transition climatologically begins as a storm begins to recurve poleward at around $35^\circ N$ (Hart and Evans, 2001), Alberto demonstrates that storms are occasionally able to move substantially poleward while retaining their pure tropical structure, in which case storm expansion may not be expected to occur.

2.5 Discussion and Conclusions

Given the high resolution and high precision of QuikSCAT data, the results presented here provide credible evidence that the global distribution of tropical cyclone size, defined as the radius of vanishing winds calculated using an outer wind structure model that assumes vanishing deep convection beyond the azimuthally-averaged radius of 12 ms^{-1} winds, is approximately log-normal. While the distribution of r_{12} is qualitatively log-normal, the distribution of r_0 is quantitatively much closer to log-normal. Moreover, in contrast to the work of *D09*, we find here that the normalization by the natural length scale of tropical cyclones, defined as the ratio of the potential intensity to the Coriolis parameter, reduces rather than improves the goodness of fit of the observed distribution to log-normal, suggesting that this length scale is not fundamental to storm size as it is observed under the current Earth climate. Control experiments indicate that the choice of the outer wind model alone is insufficient to explain the observed p-values for the distribution of outer radius; the distributions observed in nature of r_{12} and f , from which the distribution of r_0 is derived, appear to play an important role as well. Finally, analysis of the intra-storm evolution of size indicates that both r_{12} and r_0 tend to expand very slowly with time early in the storm lifecycle, after which size appears to remain nearly constant, although significant variance exists across storms.

What is the implication of the log-normal distribution in the context of tropical cyclones? As noted earlier, in the absence of significant external environmental forcing, there is evidence that the spatial extent of a given tropical cyclone remains relatively constant throughout its lifetime, suggesting that the existence of this distribution may be a manifestation of the processes that generate tropical cyclones in the first place and/or of the distribution of their precursor disturbances. However, with respect to size, there is no obvious single multiplicative process during genesis that is amenable to isolation. This will be the subject of future work.

Chapter 3

Equilibrium Tropical Cyclone Size and Structure in Axisymmetry

3.1 Introduction

Considerable progress has been made over the past three decades in elucidating the dynamics of tropical cyclones (TCs). Theory has been developed suggesting that TCs may be viewed as a Carnot heat engine whose heat source arises from the ambient thermodynamic disequilibrium of the tropical oceans (Emanuel, 1986). Furthermore, both theory and relatively simple dynamical models (Ooyama, 1969; DeMaria and Pickle, 1988; Rotunno and Emanuel, 1987; Emanuel, 1995a) are able to reproduce many of the characteristic features of mature tropical cyclones, including maximum wind speed, central sea level pressure, and thermodynamic structure. Most recently, Emanuel and Rotunno (2011) derived a full analytical solution for the radial structure of the axisymmetric balanced tropical cyclone wind field at the top of the boundary layer.

However, this latest solution remains defined relative to a single free parameter: the outer radius, r_0 . Indeed, despite wide recognition of the sensitivity of both storm surge (Irish et al., 2008) and wind damage (Iman et al., 2005) to storm size, size remains largely unpredictable, and relatively little observational or modeling work has been performed to elucidate the factors underlying its variability. In the absence

of interaction with land or extratropical disturbances, size is observed in nature to vary significantly more from storm to storm than within the lifetime of a given storm, regardless of basin, location, and time of year (Merrill, 1984; Frank, 1977; Chavas and Emanuel, 2010; Cheng-Shang et al., 2010). Size is found to correlate only weakly with both latitude and intensity (Merrill, 1984; Weatherford and Gray, 1988; Chavas and Emanuel, 2010), as the outer and inner core regions appear to evolve nearly independently. Chavas and Emanuel (2010) found that the global distribution of r_0 is approximately log-normal, though distinct median sizes exist within each ocean basin, suggesting that the size of a given TC is not merely a global random variable but instead is likely modulated either by the structure of the initial disturbance, the environment in which it is embedded, or both.

Recent research has begun to explore the sensitivity of storm size to local thermodynamic variables. Observationally, Quiring et al. (2011) combine the Extended Best Track and NCEP/NCAR Reanalysis datasets to demonstrate that various local environmental variables have at best a secondary influence on the radius of maximum wind (r_{max}) and the radius of gale force wind in the Atlantic basin, with the exception of a positive correlation between mid-level relative humidity and r_{max} . Idealized modeling studies in Hill and Lackmann (2009) and Xu and Wang (2010) found that TCs tend to be larger when embedded in moister mid-tropospheric environments due to the increase in spiral band activity and subsequent generation of diabatic potential vorticity which acts to expand the wind field laterally. Using a simple three-layer axisymmetric model, DeMaria and Pickle (1988) found that storm size at peak intensity increased with increasing background rotation rate but was constant with increasing sea surface temperature, while Smith et al. (2011) found in a separate three-layer model an optimum in storm size as a function of rotation rate attributed to the inhibitive effect of inertial stability on boundary-layer inflow as the rotation rate is increased. Finally, Rotunno and Emanuel (1987) found in an idealized axisymmetric framework a strong relationship between the horizontal length scales of the initial and mature vortex.

A dynamical systems approach may provide a path forward in improving our

understanding of tropical cyclone size. Tang and Emanuel (2010) demonstrated analytically that tropical cyclone intensity may be viewed as a non-linear dynamical system that evolves towards a stable equilibrium whose value depends on the local environmental and initial conditions. This behavior has been verified in a modeling context on both short time-scales (e.g. Rotunno and Emanuel (1987)) and long time-scales over which the storm’s maximum wind speed has achieved statistical equilibrium (Hakim, 2011). However, no such theory exists for the dynamical evolution of tropical cyclone structure, and the tropical cyclone at statistical structural equilibrium remains unexplored. This is of particular relevance given the large range of sizes observed in nature (Chavas and Emanuel, 2010).

This work seeks to build upon the small base of literature on tropical cyclone size by systematically exploring the sensitivity of the structure of an axisymmetric tropical cyclone at statistical equilibrium to the set of relevant model, initial, and environmental variables. Expanding on the work of Hakim (2011), we perform our analysis in the simplest possible model and physical environment: a highly-idealized state of radiative-convective equilibrium (RCE). The results of the sensitivity analysis are then synthesized via dimensional analysis to quantify the relationship between equilibrium storm structure and the set of relevant input parameters. Section 2 details the methodology, including model description and experimental design. Section 3 derives a useful alternative formulation of the maximum potential intensity in the context of our idealized RCE environment. Results and comparison with existing theory are presented in section 4, and discussion of some key findings are presented in section 5. Finally, section 6 provides a brief summary and conclusions.

3.2 Methodology

3.2.1 Model description

This work employs version 15 of the Bryan Cloud Model (CM1), a non-hydrostatic atmospheric cloud-system resolving model (CSRМ; original version described in Bryan

and Fritsch (2002)) that has been applied to the study of a variety of convective systems including topographic flow (Miglietta and Rotunno, 2010), tropical cyclones (Bryan and Rotunno, 2009b; Bryan, 2011), and mid-latitude squall lines (Parker, 2008). CM1 was originally written with the goal of incorporating state of the art numerics and physics, in particular for moist processes, while satisfying near-exact conservation of both mass and energy in a reversible saturated environment. The model is set up in three-dimensions but can also be configured with identical parameters for two-dimensional axisymmetric (radius-height) geometry, a convenient property that will be exploited in this work.

CM1 solves the fully compressible set of equations of motion in height coordinates on an f-plane for flow velocities (u, v, w) , non-dimensional pressure (π) , potential temperature (θ) , and the mixing ratios of water in vapor, liquid, and solid states (q_x) on a fully staggered Arakawa C-type grid in height coordinates. The model has a rigid lid at the top with a 5-km thick damping layer beneath and a wall at the domain's outer horizontal edge with an adjacent damping layer whose thickness is set to approximately $\frac{1}{15}$ of the domain's width. The damping time-scale is set to its default value of 6 minutes. Model horizontal (x-y) and vertical grid spacing are each constant in the domain. Model microphysics is represented using the Goddard-LFO scheme based on Lin et al. (1983), which is a mixed-phase bulk ice scheme with prognostic equations for water vapor, cloud water, rainwater, pristine ice crystals, snow, and large ice. For full details, see Bryan and Fritsch (2002). Lastly, in lieu of a comprehensive scheme for radiative transfer, an idealized scheme (discussed below) is imposed due to its simplicity.

Turbulence is parameterized using a Smagorinsky-type closure scheme (Smagorinsky, 1963), which assumes steady and homogeneous unresolved turbulence, modified such that different eddy viscosities are used for the horizontal/radial and vertical directions to represent the differing nature of turbulence between the radial and vertical directions in a highly anisotropic system such as in the inner core of a tropical cyclone. In the context of tropical cyclones, turbulence fulfills the critical role of counteracting eyewall frontogenesis by the secondary circulation that, in the inviscid limit, would

lead to frontal collapse (Emanuel, 1997). Meanwhile, in a three-dimensional RCE state, turbulence has a minimal impact on the mean state.

3.2.2 Idealized model/environmental RCE set-up

We construct a highly-idealized model and environmental configuration with the objective of reducing the model atmospheric system to the simplest possible state (i.e. minimal number of dimensional variables) that supports a tropical cyclone. Model horizontal and vertical grid spacings are set to $dx = dy = dr = 4 \text{ km}$ and $dz = .625 \text{ km}$, respectively, and no grid stretching is applied. This horizontal resolution was selected with the goal of minimizing both the sensitivity of storm structure to grid spacing and the overall computational load. Surface pressure is set to 1015 hPa . Radiation is represented simply by imposing a constant cooling rate (which is typical of the clear-sky mean tropical troposphere, see Hartmann et al. (2001)), Q_{cool} , to the potential temperature everywhere in the domain where the absolute temperature exceeds a threshold value, T_{tpp} ; below this value, Newtonian relaxation back to this threshold is applied:

$$\frac{\partial \theta}{\partial t} = \begin{cases} -Q_{cool} & T > T_{tpp} \\ \frac{\theta(p, T_{tpp}) - \theta(p, T)}{\tau} & T \leq T_{tpp} \end{cases} \quad (3.1)$$

where θ is potential temperature, T is absolute temperature, and τ is the relaxation timescale, set to 40 days (except in the damping layer as noted above). Thus, all water-radiation and temperature-radiation feedbacks are neglected. The lower-boundary sea surface temperature, T_{sst} , is set constant. Surface fluxes of enthalpy and momentum are calculated using standard bulk aerodynamic formulae

$$F_k = C_k \rho |\mathbf{u}| (k_s^* - k) \quad (3.2)$$

$$\tau_s = -C_d \rho |\mathbf{u}| \mathbf{u} \quad (3.3)$$

where F_k is the surface enthalpy flux, ρ is the near-surface air density, \mathbf{u} is the near-surface (i.e. lowest model level) wind velocity, k is the near-surface enthalpy, k_s^*

is the saturation enthalpy of the sea surface, τ_s is the surface stress, and the exchange coefficients for momentum, C_d , and enthalpy, C_k , are set constant, despite their acknowledged real-world dependence on wind-speed (Powell et al., 2003). Finally, background surface enthalpy fluxes are required to balance column radiative cooling in order to achieve RCE in the absence of significant resolved wind perturbations (such as a tropical cyclone). Because axisymmetric geometry precludes the direct imposition of a background flow, we instead simply add a constant gustiness, u_{sfc} , to $|\mathbf{u}|$ for the model calculation of (3.2) and (3.3). This set-up is conceptually similar to that of Hakim (2011) with the important exceptions that here we employ a non-interactive radiative scheme and we include background surface fluxes throughout the domain.

This configuration provides a simplified framework for the exploration of equilibrium tropical cyclone structure in RCE. Nolan et al. (2007) demonstrated that, in the presence of a full radiation scheme, the f-plane RCE state depends only on T_{sst} , u_{sfc} and very weakly on the Coriolis parameter, f . For this work, the idealized radiation scheme introduces two additional degrees of freedom, T_{tpp} and Q_{cool} , to which the RCE state is sensitive. Thus, we initialize each axisymmetric simulation with the RCE solution from the corresponding three-dimensional simulation on a $196 \times 196 \text{ km}^2$ domain with identical T_{sst} , T_{tpp} , Q_{cool} , and u_{sfc} ; the RCE state is indeed found to be nearly insensitive to f (not shown) and thus it is held constant at its Control value to reduce computational load. This domain size is specifically chosen to be large enough to permit a large number of updrafts but small enough to inhibit convective self-aggregation (Bretherton et al., 2005) over a period of at least 100 days. The RCE solution is defined as the 30-day time- and horizontal-mean vertical profiles of potential temperature and water vapor, with the threshold for equilibrium defined as $\frac{\partial \theta}{\partial t} < \frac{1}{30} \text{ K day}^{-1}$ over the equilibrium period at all model levels; in most cases, this period corresponds to simulation days 70-100, though in a few cases (primarily those with low radiative cooling rates for which equilibration is slow) the simulation is extended until the equilibrium criterion is met. Overall, this approach ensures that each axisymmetric simulation begins very close to its “natural” model-equilibrated

background state (first emphasized in Rotunno and Emanuel (1987)) and thus is absent any significant stores of available potential energy that may exist by imposing an alternate initial state, such as a mean tropical sounding.

The result of the above methodology is a model RCE atmosphere comprised of a troposphere capped by a nearly isothermal stratosphere at temperature T_{tpp} . More generally, this model tropical atmosphere may be thought of as an extension of the classical fluid system in which a fluid is heated from below and cooled from above (albeit throughout the column), but with two key modifications: 1) the energy input into the system is dependent on wind-speed, thereby permitting a wind-induced surface heat exchange (WISHE; Emanuel (1986)) feedback; and 2) the energy lost from the system is dependent on an externally-defined temperature threshold, T_{tpp} , which conveniently corresponds to the convective outflow temperature central to the maximum potential intensity theory of tropical cyclones. Both modifications facilitate a more straightforward methodology and analysis of the factors that modulate equilibrium storm size and structure.

3.2.3 Initial perturbation

Bister and Emanuel (1997) demonstrated that the fundamental process during tropical cyclogenesis is the near-saturation of the column at the mesoscale in the core of the nascent storm. Thus, we superpose an initial perturbation upon the background RCE state by saturating the air at constant virtual temperature in a region above the boundary layer bounded by $z = [1.5, 9.375] \text{ km}$ and $r = (0, r_{0_q})$ within a quiescent environment. We also test an initial mid-level vortex of the form used in Rotunno and Emanuel (1987), characterized by a radius of vanishing wind r_{0_u} and a peak wind of $V_{m_0} = 12.5 \text{ ms}^{-1}$ at $r_{m_0} = r_{0_u}/5$, centered at $z = 4.375 \text{ km}$ with azimuthal wind speeds above and below decaying linearly to zero over a distance of 2.875 km . However, as is shown in Fig. 3-7, the two approaches have similar results, and thus for the sake of simplicity we elect to initialize all other simulations with the mid-level moisture anomaly. In addition to this initial disturbance, random perturbations with magnitudes uniformly distributed on the range $[-1, 1] \text{ K}$ are added to the potential

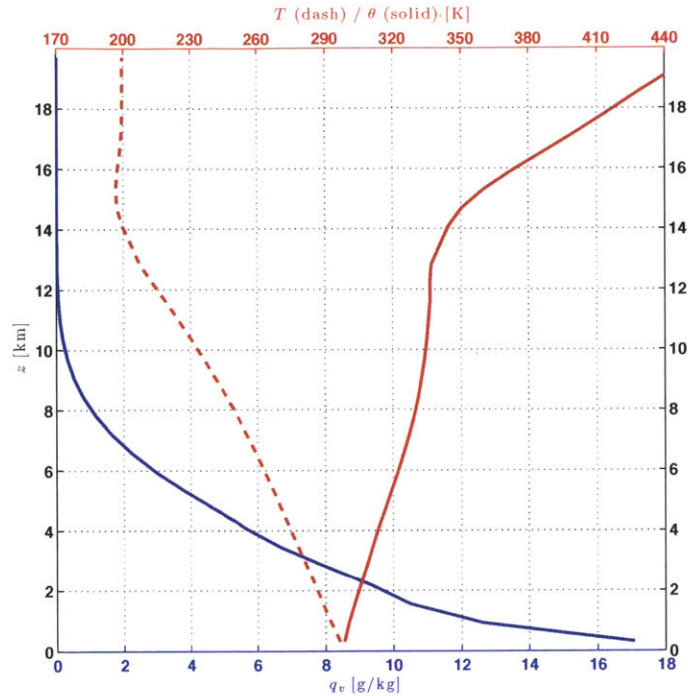


Figure 3-1: Initial three-dimensional radiative-convective equilibrium vertical profile of temperature (red dashed), potential temperature (red solid), and water vapor mixing ratio (blue) for the Control simulation.

temperature field at every point to break the initial horizontal symmetry of the model.

3.2.4 Control simulation parameter values

For the Control simulation, values of the key external parameters for the model, environment, and initial condition are provided in Table 3.1. The values of the horizontal and vertical mixing lengths, l_h , and l_v , respectively, used in the Smagorinsky-type parameterization of three-dimensional turbulence are typical values taken from the literature (Bryan and Rotunno, 2009a). The corresponding initial three-dimensional RCE vertical profile of potential temperature and water vapor is displayed in Figure 3-1.

The domain size for the Control run requires special attention. Prior research modeling tropical cyclones typically place the outer wall of the domain at a distance of 1000-1500 km (e.g. Rotunno and Emanuel (1987); Hakim (2011)). However, as shown

Table 3.1: Parameter values for the Control simulation. The parameters l_h and l_v correspond to the horizontal and vertical mixing lengths, respectively, in the turbulence parameterization; H_{domain} is the height of the model lid; L_{domain} is the radius of the outer wall in the axisymmetric model.

| Model | Value | Environment | Value | Initial Perturbation | Value |
|--------------|-----------------|-------------|---|----------------------|---------------|
| l_h | 1500 <i>m</i> | T_{sst} | 300 <i>K</i> | r_{0_g} | 200 <i>km</i> |
| l_v | 100 <i>m</i> | T_{tpp} | 200 <i>K</i> | r_{0_u} | 400 <i>km</i> |
| C_k, C_d | .0015 | Q_{cool} | 1 <i>K day</i> ⁻¹ | | |
| H_{domain} | 25 <i>km</i> | u_{sfc} | 3 <i>m s</i> ⁻¹ | | |
| L_{domain} | 12288 <i>km</i> | f | 5×10^{-5} <i>s</i> ⁻¹ | | |

in Figure 3-2, which depicts the day 100-150 mean radial profile of the azimuthal component of the gradient wind at $z = 1.56$ *km*, storm size is dramatically influenced by the radius of the outer wall up to an upper bound; the storm seems content to simply fit into the box into which it is placed. Beyond this upper bound, the equilibrium storm is largely insensitive to the location of the wall. The theoretical basis underlying the existence of this upper bound is discussed below.

Thus, because the outer wall is purely a model artifact, we set it conservatively at $L_{domain} = 12288$ *km* for all simulations run herein. This has the added benefit of ensuring that the storm itself is not significantly altering the background environment, which could modify the potential intensity from its RCE value.

3.2.5 Characterizing equilibrium storm structure

All simulations are run for 150 days in order to allow sufficient time for the full tropical cyclone structure to reach statistical equilibrium, and data is output at 6-hour intervals. We then calculate a 2-day running mean of the radial profile of the azimuthal gradient wind at $z = 1.56$ *km* to reduce noise in the pressure field. Results are not sensitive to the output frequency nor the averaging period length. We calculate the gradient wind, V_g , directly from model prognostic variables based on gradient wind balance:

$$V_g = -\frac{1}{2}fr + \left(\frac{1}{4}f^2r^2 + rC_p\theta_v \frac{\partial\pi}{\partial r} \right)^{\frac{1}{2}} \quad (3.4)$$

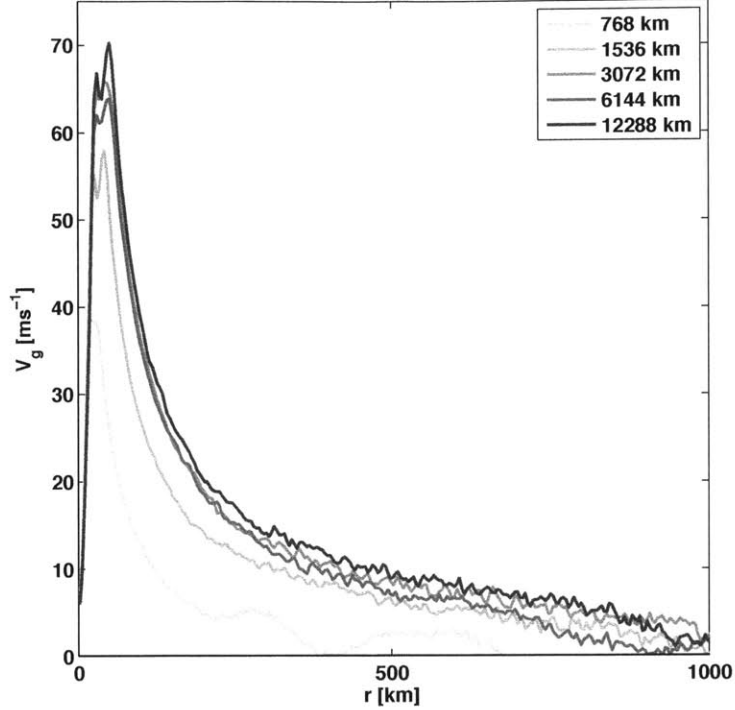


Figure 3-2: Time-mean radial gradient wind profiles at $z = 1.56 \text{ km}$ for days 100-150 as a function of domain width. Note the convergence in storm size beyond $L_{domain} \approx 3000 \text{ km}$.

where r is radius, C_p is the specific heat of air at constant pressure, θ_v is the virtual potential temperature, and π is the Exner function. The pitfalls of using the full π (i.e. including contributions from both the balanced and unbalanced flow) for calculating V_g are discussed in Bryan and Rotunno (2009a). The equilibrium radial wind profile is defined as the time-mean of the 30-day period after day 60 with the minimum time-variance in the maximum gradient wind speed, V_m . For two cases ($f = 10^{-4} \text{ s}^{-1}$, $l_h = 750 \text{ m}$), the equilibrium period was adjusted manually to account for ongoing structural variability. Though simplistic, this definition provides a clean signal in many of the details discussed below. A dynamic equilibrium period is preferable to a static one (e.g. day 70-100 mean) to account for simulations that exhibit significant long-period variability in storm structure.

Following the theory presented in Emanuel and Rotunno (2011), we would ideally characterize the structure of the tropical cyclone wind field near the top of the

boundary layer with three variables: the maximum gradient wind speed, V_m , the radius of maximum gradient wind, r_m , and the outer radius of vanishing wind, r_0 . However, variability in the radial profile of the gradient wind in the eyewall, which typically (though not always) exhibits a double-humped structure due to the existence of super-gradient flow (see Bryan and Rotunno (2009a) for discussion), renders r_m noisy. Thus, as a proxy we will track the radius of 75% of V_m outside of the eyewall, hereafter denoted r_{ew} , which is more stable and typically scales closely with r_m .

Meanwhile, direct calculation of r_0 is problematic due to the large variability toward the outer edge of the model storm ($V \lesssim .1V_m$) and correspondingly large sensitivity of the precise value of r_0 to this variability. Instead, we employ the outer wind structure model derived in Emanuel (2004) to represent the outer portion of the storm circulation and to estimate r_0 . This outer wind model assumes that the flow is steady, axisymmetric, and absent deep convection, resulting in a local balance between subsidence warming and radiative cooling. Furthermore, the equilibrium radiative subsidence velocity, w_{cool} , can be taken to be approximately constant with radius. In equilibrium, this subsidence rate must match the rate of Ekman suction-induced entrainment of free tropospheric air into the boundary layer in order to prevent the creation of large vertical temperature gradients across the top of the boundary layer. The radial profile of azimuthal velocity is therefore determined as that which provides the required Ekman suction and is governed by the following differential equation

$$\frac{\partial(rV)}{\partial r} = \frac{2r^2 C_d V^2}{w_{cool}(r_0^2 - r^2)} - fr \quad (3.5)$$

where r is the radius and V is the azimuthal wind speed. Eq. (3.5) is a Riccati equation with no known analytical solution. The value of w_{cool} is calculated from the assumed balance between subsidence-induced warming and radiative cooling

$$w_{cool} \frac{\partial \theta}{\partial z} = Q_{cool} \quad (3.6)$$

where $\frac{\partial \theta}{\partial z}$ is set to its pressure-weighted mean value in the layer $z = 1.5 - 5 \text{ km}$ (i.e. directly above the boundary layer) for the background state (see Section 3.2.8).

For the Control run, this gives $w_{cool} = .25 \text{ cms}^{-1}$, which agrees well with the value of .24 obtained by calculating the mean (negative) vertical velocity in the region $r = [400, 600] \text{ km}$ and $z = [1.5, 5] \text{ km}$ from the equilibrium state of the Control simulation. Finally, given a single point in r-V space, (3.5) may be solved numerically for r_0 using a shooting method. Details of the application of this analytical model are reprised in a later section.

The equilibrium maximum gradient wind speed, V_m , is defined as the time-mean of its 2-day running mean value over the equilibrium period in order to account for shifts in r_m that would act to smooth out V_m , though the difference between this value and the simple time-mean value is typically small ($\leq 1\%$). Meanwhile, equilibrium values of the two size variables, r_{ew} and r_0 , are calculated directly from the final equilibrium radial profile.

3.2.6 Experimental approach: parametric sensitivities and dimensional analysis

We begin by running a Control simulation whose parameter values are given above and the evolution of which is discussed below. We then perform a wide range of experiments in which we independently and systematically vary all eight external dimensional parameters that are potentially relevant to the dynamics of the system: T_{sst} , T_{tpp} , Q_{cool} , u_{sfc} , l_h , l_v , f , and r_{0q} . For each of l_h , l_v , f , r_{0q} , we run simulations successively halving and doubling from the Control value, while for the four thermodynamic parameters we run simulations each varying one parameter from Control as follows: $T_{sst} = 285, 287.5, 290, 292.5, 295, 300, 305, 310 \text{ K}$; $T_{tpp} = 238, 225, 213, 200, 188, 175, 163, 150 \text{ K}$; $u_{sfc} = 10, 5, 4, 3, 2, 1, 0.5 \text{ ms}^{-1}$; and $Q_{cool} = .25, .375, .5, .75, 1, 1.5, 2, 3, 4 \text{ K day}^{-1}$. These ranges, listed in order of increasing V_p , span a reasonable range of values of V_p from $50 - 150 \text{ ms}^{-1}$.

Some important modifications are made to accommodate the wide range of simulations presented here. The domain height is increased by 5 km in cases where the troposphere is deeper than Control to ensure that the upper damping layer lies suffi-

ciently far above the tropopause. For the above sensitivity experiments in which the equilibrium radius of maximum wind is less than the Control value, the simulation is re-run at doubled horizontal resolution (i.e. $dx = 2 \text{ km}$, $L_{domain} = 6144 \text{ km}$ domain) to ensure that the inner storm core is comparably resolved. Lastly, the time step is halved in cases where the CFL condition is violated.

The final scaling results indicate to which dimensional variables the equilibrium storm structure is systematically sensitive. Dimensional analysis is then applied to synthesize the results in a non-dimensional framework.

3.2.7 Potential Intensity in RCE

The architecture of this model RCE state enables the equation for the maximum potential intensity to be reformulated in a useful manner. The generalized potential intensity (Emanuel, 2010) is given by

$$V_p^2 = \frac{C_k}{C_d} \frac{T_{sst} - T_{tpp}}{T_{tpp}} (k_0^* - k) \quad (3.7)$$

Combining (3.7) with the surface enthalpy flux equation in (3.2) gives

$$V_p^2 = \frac{T_{sst} - T_{tpp}}{T_{tpp}} \frac{F_k}{\rho C_d |\mathbf{u}|} \quad (3.8)$$

In RCE, column energy balance requires that the surface enthalpy flux into the column be exactly balanced by the column-integrated radiative cooling, which in this idealized set-up is given by

$$F_k = - \int_{p_s}^0 C_p \frac{\partial T}{\partial t} \frac{dp}{g} = - \int_{p_s}^0 C_p \frac{\partial \theta}{\partial t} \left(\frac{p}{p_0} \right)^{R_d/C_p} \frac{dp}{g} = C_p Q_{cool} \frac{\overline{\Delta p}}{g} \quad (3.9)$$

where C_p is the specific heat of air, $\overline{\Delta p}$ given by

$$\overline{\Delta p} = \frac{p_0}{1 + \frac{R_d}{C_p}} \left(\left(\frac{p_s}{p_0} \right)^{1 + \frac{R_d}{C_p}} - \left(\frac{p_{tpp}}{p_0} \right)^{1 + \frac{R_d}{C_p}} \right) \quad (3.10)$$

is the mean pressure depth of the troposphere, reduced slightly by the adiabatic expansion term in the integrand of (3.9), and we have ignored any small contribution from Newtonian relaxation in the stratosphere. Substituting (3.9) into (3.8) results in

$$V_p^2 = \frac{T_{sst} - T_{tpp}}{T_{tpp}} \frac{C_p Q_{cool} \overline{\Delta p}}{g \rho C_d |\mathbf{u}|} \quad (3.11)$$

Thus, (3.11) makes it readily apparent that the potential intensity in RCE with constant tropospheric cooling is a function of four externally-defined parameters: T_{sst} , T_{tpp} , u_{sfc} , and Q_{cool} , with the tropospheric thickness Δp primarily a function of T_{tpp} . Note that $|\mathbf{u}|$ represents the mean background wind speed, including both the resolved mean wind speed and the gustiness, u_{sfc} ; because the TC occupies only a small areal fraction of the very large domain, its contribution to the mean wind is small.

This analytical result will be leveraged below, though all values of potential intensity presented herein are calculated from the background state sounding (defined in the subsequent section) using the detailed Emanuel sub-routine (Bister and Emanuel, 2002) with zero boundary layer wind speed reduction under pseudo-adiabatic thermodynamics and including dissipative heating.

3.2.8 Defining the background state

Though we initialize each axisymmetric simulation with the three-dimensional RCE state, ultimately the more relevant background state for the equilibrium tropical cyclone is that of the ambient environment beyond the storm circulation in the axisymmetric model itself. Thus, we define the background state as the area-weighted mean vertical profile of potential temperature and water vapor averaged over the radial grid points 2000-2500, which corresponds to the region $r = [8000, 10000]$ km for our Control domain size. This quantity is largely insensitive to radius or averaging time period so long as it is calculated beyond the primary storm circulation. From this background state, we may calculate relevant quantities for our analysis, including the potential intensity, radiative-subsidence rate, and deformation radius.

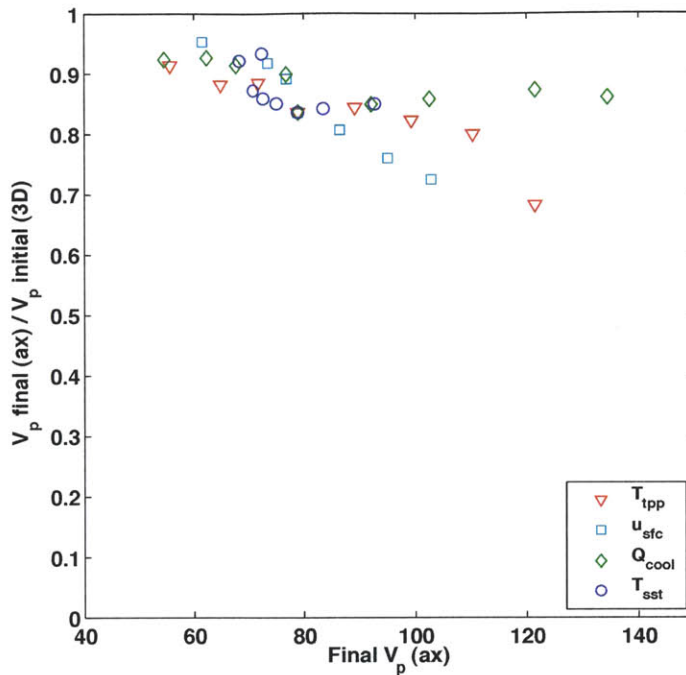


Figure 3-3: Comparison of the potential intensity, V_p , calculated from the initial three-dimensional RCE state and the final axisymmetric RCE state outside of the storm across simulation sets varying each of the four governing thermodynamic parameters.

The potential intensity for the axisymmetric RCE state is typically 80-90% of the value of the corresponding three-dimensional RCE state, though they do not differ precisely by a constant factor across simulations. Figure 3-3 displays the fractional reduction of V_p in axisymmetry relative to its three-dimensional counterpart across the simulation sets varying each of the four governing thermodynamic parameters. As in the three-dimensional case, the axisymmetric V_p is predominantly a function of these thermodynamic parameters. In the cases of varying T_{tp} and u_{sfc} , there is systematic variation in this fractional reduction, such that this reduction increases with increasing V_p . Meanwhile, this quantity does not vary significantly with l_h , f , or domain size, suggesting that the difference in V_p between axisymmetry and three-dimensions is not attributable to the existence of the storm itself (i.e. the relative contribution of the storm circulation to the domain-mean resolved near-surface wind) but rather is related to the differing nature of convection in the two geometries. This

is curious and warrants further investigation.

3.3 Results

3.3.1 Control run

Figure 3-4 displays the time evolution of the 2-day running mean of V_m , r_m , and an estimate of the outer radius, r_0 (calculated as in Section 3.3.4), for the Control simulation as well as estimated time-scales to equilibrium for each individual variable. The time-scale to equilibrium, τ_x , where x is the variable of interest, is defined as the starting time of the first 30-day interval whose mean value is within 10% of the equilibrium value and whose average daily rate of change over this period does not exceed 1% of the mean. All three variables exhibit similar qualitative evolutions: rapid increase during genesis to a super-equilibrium value followed by a more gradual decay to equilibrium. However, the maximum excess over equilibrium is very large for r_0 and r_m ($\sim 100\%$) and relatively small ($\sim 30\%$) for V_m , the latter of which matches the overshoot value found in Hakim (2011) for the same radial turbulent mixing length. Moreover, the time-scales to equilibrium for storm size are significantly longer for size ($\tau_{rm} = 70$ days and $\tau_{r_0} = 61$ days) than for intensity ($\tau_V = 29$ days). The details of the transient phase of the structural evolution will be explored in future work. Ultimately, the Control simulation's equilibrium storm structure is characterized by $V_m^{eq} = 70$ ms^{-1} , $r_m^{eq} = 46$ km , $r_0^{eq} = 694$ km . Importantly, the Control case exhibits non-negligible long-period variability of $\sim 20\%$ about the estimated equilibrium value, leaving some ambiguity regarding the precise values for each structural variable at equilibrium.

These results suggest that modeling tropical cyclones over a period sufficient to achieve quasi-equilibrium in intensity (typically 10-20 days), as is commonly done in the literature, may result in a storm that has not reached structural equilibrium or else has done so artificially due to the domain-limitation imposed by the model's outer wall.

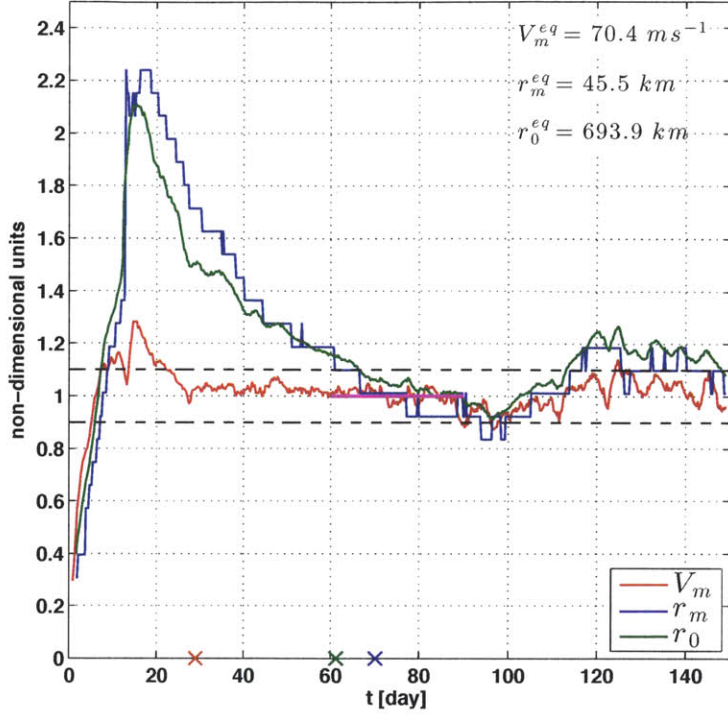


Figure 3-4: For the Control simulation, time evolution of the 2-day running mean V_m , r_m , and r_0 normalized by their respective equilibrium values (upper-right corner). For this simulation, $V_p = 79 \text{ m s}^{-1}$ and $f = 5 \times 10^{-5} \text{ s}^{-1}$. Pink line denotes 30-day period used for equilibrium calculation, and black dashed lines denote $\pm 10\%$ of the equilibrium value. Markers along the abscissa denote estimated time-scales to equilibration.

3.3.2 Radial profile sensitivity tests

The principal objective is to collapse the radial wind profiles across all simulations to a single curve based on external parameters alone. Thus, we begin simply with the dimensional radial gradient wind profiles for eight simulation sets, each of which correspond to one of the eight external dimensional parameters, displayed in Figure 3-5, in order to highlight a few basic but important features. First, both storm intensity and inner-core size (e.g. r_m) increase with increasing potential intensity across all four thermodynamic parameters (panels 1-4). Second, storm size decreases with increasing f and increases with increasing l_h , the latter primarily only within the inner core, while storm intensity decreases with increasing f and l_h . Detailed analysis of the

effects of the horizontal mixing length is found in Bryan and Rotunno (2009b) and Rotunno and Bryan (2012). Third, the equilibrium storm forgets the initial condition, r_{0_q} (panel 8), with an identical result for an initial mid-level vortex (not shown; see Figure 3-7 for scalings). Finally, storm intensity and overall size are not systematically sensitive to the vertical mixing length, l_v (panel 7), which corroborates the results of Bryan and Rotunno (2009b) and Rotunno and Bryan (2012); larger vertical mixing length magnitudes do correspond to a slow expansion of the eye at the apparent expense of the eyewall, though its overall effect remains small relative to that of l_h , so long as l_v is much smaller than the depth of the troposphere as is easily the case for the range of plausible values. A much deeper discussion of the role of l_v in the boundary layer in the broader context of classical vortex flow solutions with frictional boundary layers is discussed in Rotunno and Bryan (2012). Thus, based upon these results, we hereafter elect to neglect the effects of both the initial condition and the vertical mixing length, leaving only six external dimensional parameters.

Given the structural similarity apparent in the dimensional curves in Figure 3-5, we propose to normalize V by V_m and r by r_{ew} (the radius of 75% of the maximum wind); the result is shown in Figure 3-6. Remarkably, this single normalization removes a large majority of the variability in each case and, conveniently, separates any residual variability between the inner core region and the outer circulation. In effect, Figure 3-6 provides a road map for analysis, beginning first and foremost with the relationship between the internal variables V_m and r_{ew} and our external dimensional parameters, followed by an exploration of the residual variability in the eye, eyewall, and outer region of the storm.

Based on Eq. (3.11) and the common scaling of both intensity and size with V_p , we hypothesize that the primary role of the dimensional parameters T_{sst} , T_{tpp} , Q_{cool} , and u_{sfc} is to modulate the potential intensity, V_p . From among the four thermodynamic external parameters, the tropopause temperature is the simplest theoretically, such that its variability should affect only the potential intensity and the depth of the troposphere, H . It will also slightly modulate the column-integrated radiative cooling, but due to the exponential decay in density with height, the mass of the troposphere

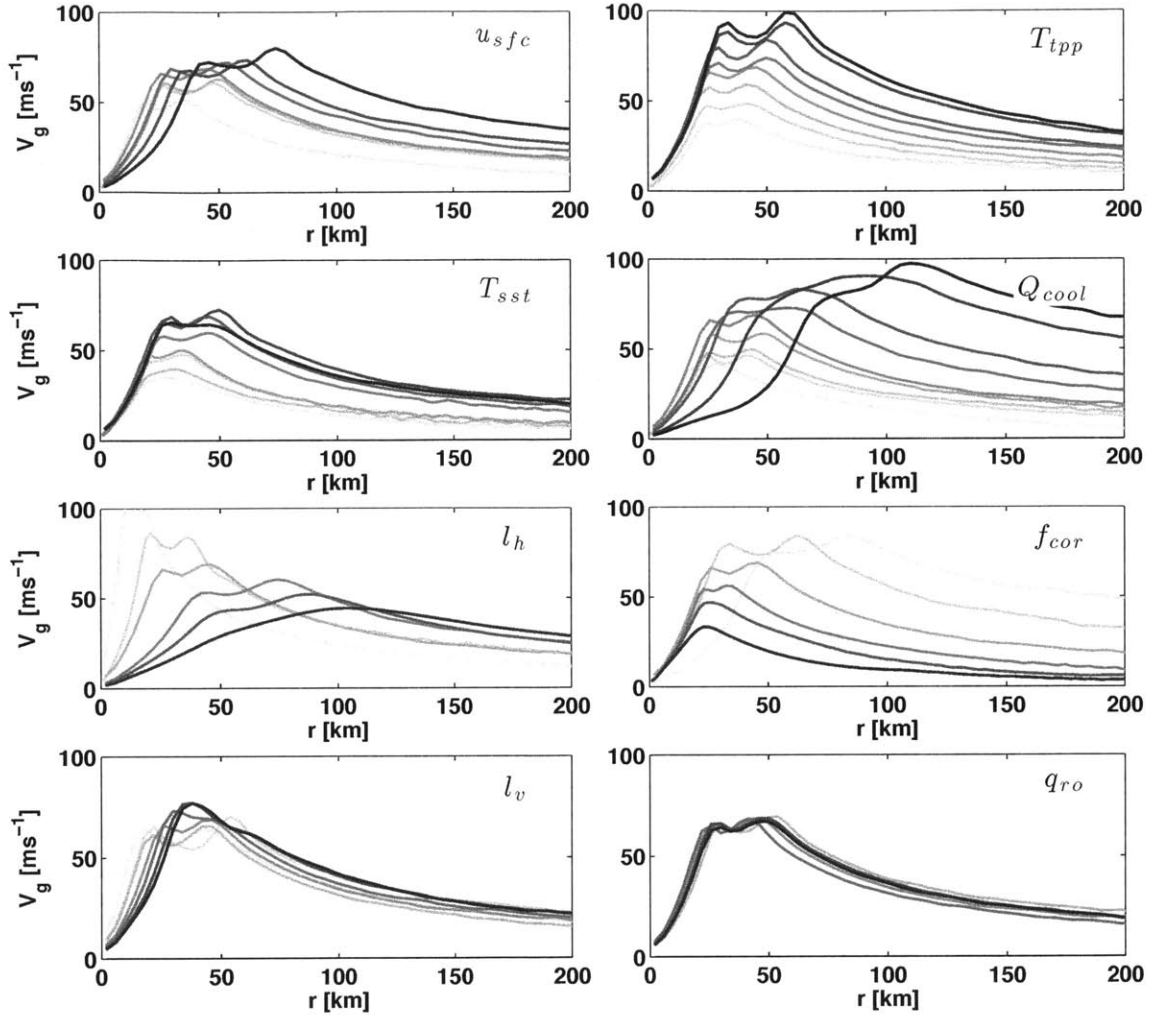


Figure 3-5: Equilibrium radial profiles of the gradient wind for simulation sets in which each of the eight dimensional external parameters is varied. The top four panels correspond to the four thermodynamic parameters, for which shading reflects potential intensity from low (light grey) to high (black); the bottom four panels correspond to relevant dynamic parameters, for which shading reflects parameter magnitude from low (light grey) to high (black).

varies by $\lesssim 15\%$ over the range of tropopause temperatures explored here. Given that H is not expected to be relevant to the dynamics of the system so long as $\frac{l_v}{H} \ll 1$ as noted earlier, we argue that T_{tpp} represents the “base” case that isolates the variability in storm structure due strictly to variations in V_p . We focus first on this base case,

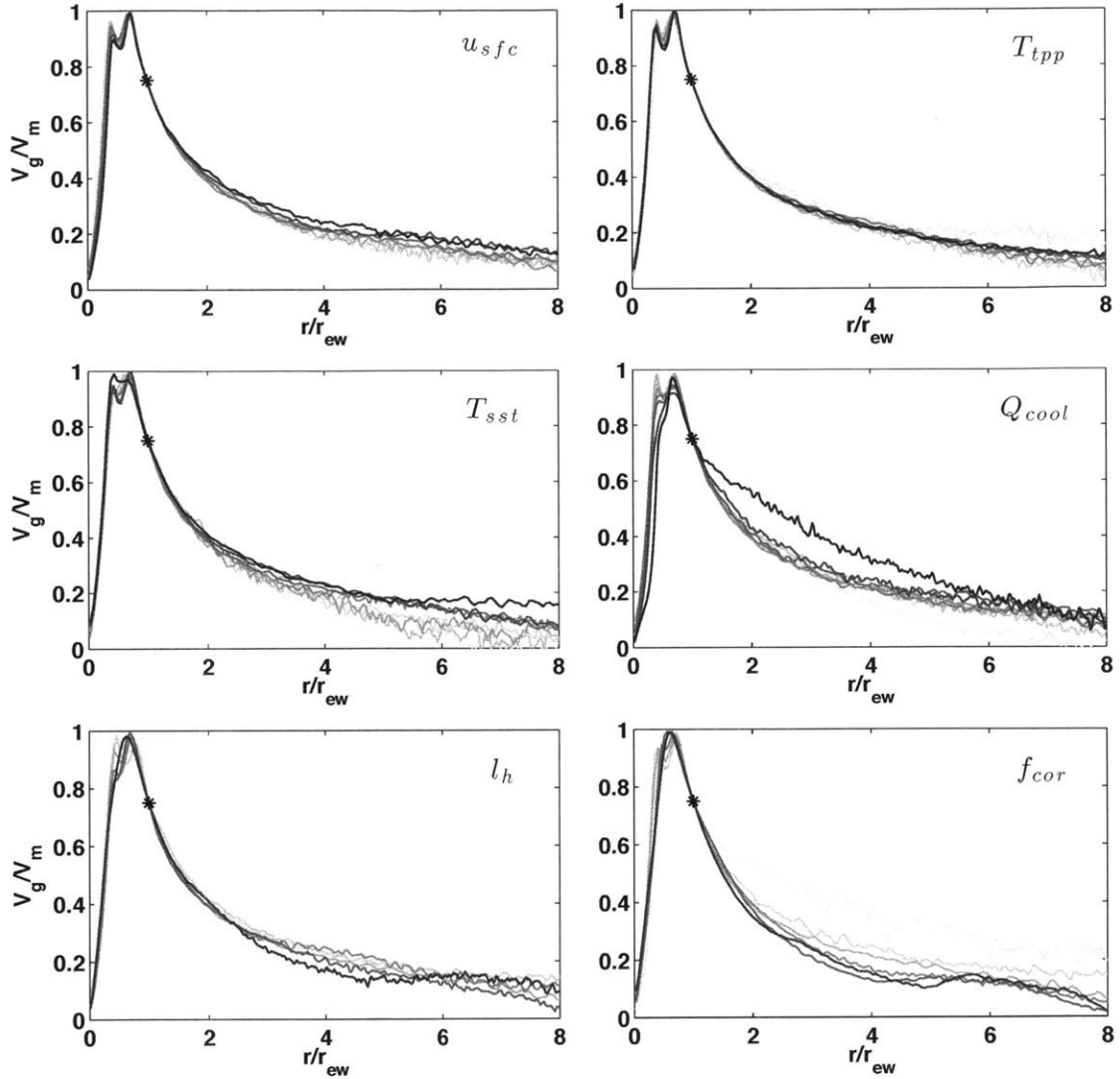


Figure 3-6: As in Figure 3-5, but with radial profiles normalized as follows: V by V_m and r by r_{ew} . Only those six parameters exhibiting strong structural sensitivity are shown.

$V_p(T_{tpp})$, before proceeding to analysis of the other three parameters, which may have additional effects on the system superimposed upon that associated with V_p .

3.3.3 Base case: Inner core

Figure 3-7 displays the scaling of V_m and r_{ew} with the set of relevant input physical parameters. Both structural variables exhibit systematic sensitivity to three param-

eters: $V_p(T_{tpp})$, f , and l_h , with minimal sensitivity to the other parameters as noted above.

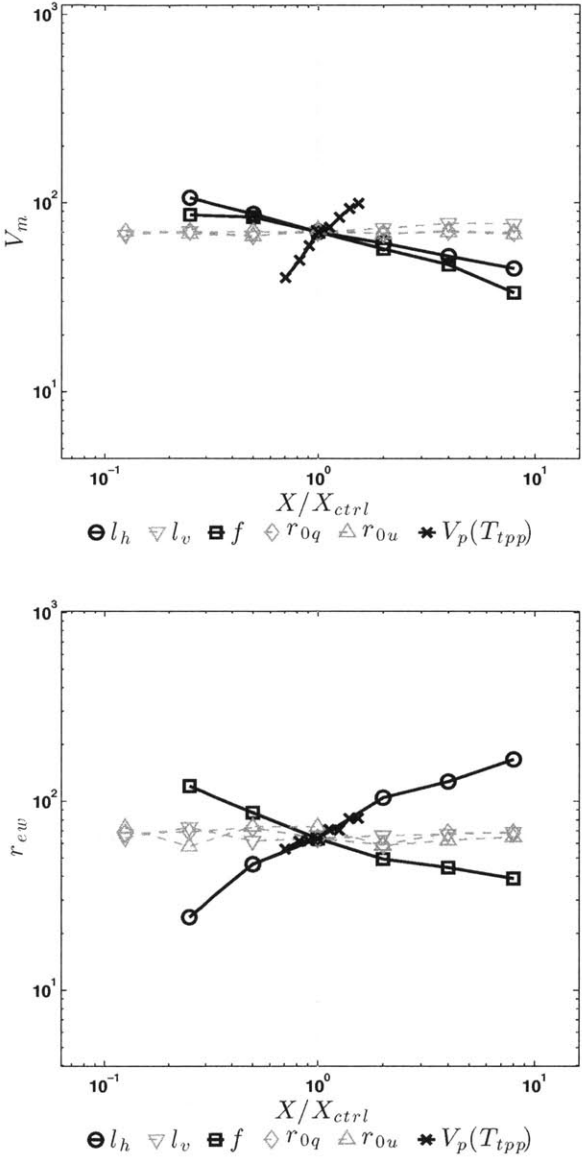


Figure 3-7: Scaling of the equilibrium value of V_m (top) and r_{ew} (bottom) with relevant dimensional parameters, X , normalized by their respective Control values (absicssa). Parameters to which a structural variable exhibits systematic sensitivity are plotted in solid black.

Rather than analyzing the role of each parameter independently, though, we may synthesize the results quantitatively via dimensional analysis. The Buckingham-Pi theorem states that the number of independent non-dimensional parameters in a

dimensional system is equal to the difference between the number of independent dimensional parameters and the number of fundamental measures. For our purposes, we have three relevant dimensional parameters and two fundamental measures, distance and time, thereby giving only one independent non-dimensional parameter, hereafter C_1 . Any output non-dimensionalized quantity, Y , can be expressed as a function of the set of non-dimensional parameters. For our system, the result is

$$Y = f(C_1) \quad (3.12)$$

The form of this functional relationship can only be determined by experimentation.

Thus, we define the dominant non-dimensional number in this system as

$$C_1 = \frac{V_p}{fl_h} \quad (3.13)$$

We choose to non-dimensionalize V_m by V_p and r_{ew} by $\frac{V_p}{f}$.

The scalings between the two non-dimensional structural variables and C_1 for a suite of experiments varying one or more of V_p , f , or l_h are displayed in Figure 3-8; parameters for the set of experiments are given in Table 3.2. A linear relation in log-log space corresponds to a power-law scaling whose exponent is given by the linear slope, i.e.

$$Y = C_1^\alpha \quad (3.14)$$

The linearly-regressed slopes are also given in Figure 3-8. In the case of r_{ew} , the power law indeed provides the best statistical fit. In the case of V_m , though, the log-log plot exhibits slight negative curvature, particularly towards low values of C_1 , indicating that a logarithmic relationship, $Y \sim \beta \times \log_{10}(C_1)$, provides a slightly better fit; this regression with $\beta = .37$ is plotted as well (dash-dot line). Though statistically slightly less precise, the power law relationship is much more amenable to theoretical physical insight. The resulting non-dimensional power-law relationships are given by

$$\frac{V_m}{V_p} \sim \left(\frac{V_p}{fl_h} \right)^{.27} \quad (3.15a)$$

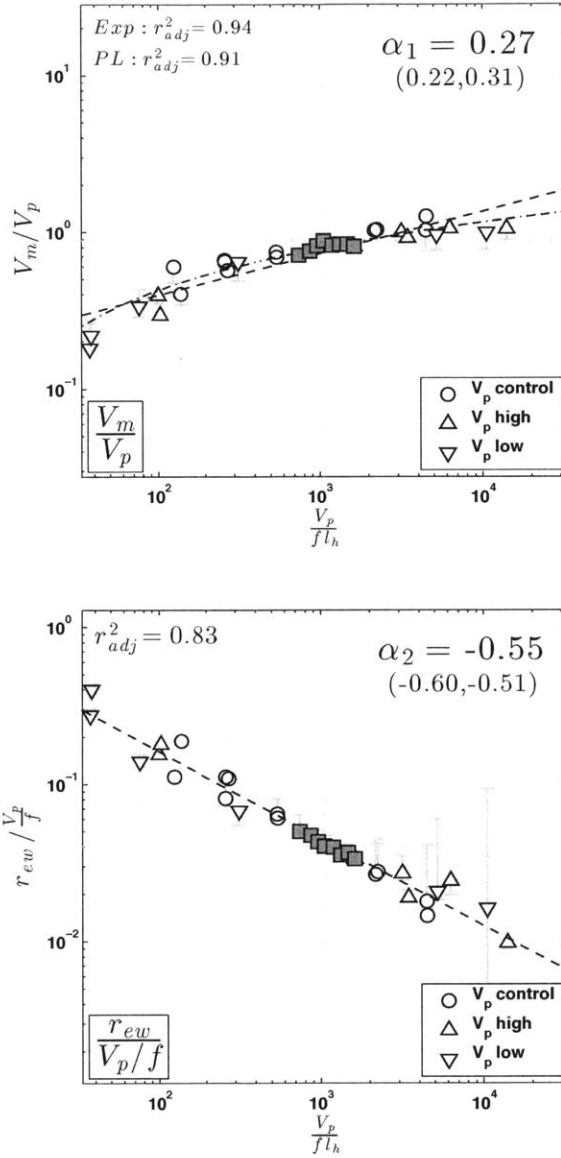


Figure 3-8: Scaling of the equilibrium values of the non-dimensionalized structural variable V_m (top), r_{ew} (bottom) with the non-dimensional number $C = \frac{V_p}{f l_h}$. Best-fit linear regressions plotted (dash), whose linearly-regressed slopes, corresponding to the estimated power-law scaling exponent in (3.14), and associated 95% confidence intervals listed (parentheses) and r-square values adjusted to account for the number of estimators (top-left corner). For V_m , a logarithmic regression is also shown (dash-dot). Grey fill highlights those simulations for which $V_p(T_{tpp})$ alone is modulated. Grey bars indicate the full range of variability of the 30-day running mean after day 60.

$$\frac{r_{ew}}{\frac{V_p}{f}} \sim \left(\frac{V_p}{fl_h} \right)^{-.55} \quad (3.15b)$$

We may then solve (3.15) for the corresponding dimensional scalings:

$$V_m \sim V_p^{1.27} (fl_h)^{-.27} \quad (3.16a)$$

$$r_m \sim \left(\frac{V_p}{f} \right)^{.45} (l_h)^{.55} \quad (3.16b)$$

Thus, equilibrium storm intensity is found to scale super-linearly with the potential intensity and, more weakly, inversely with both the background rotation rate and the radial turbulent mixing length. The equilibrium r_{ew} , which scales closely with the radius of maximum gradient wind, is found to scale approximately as the geometric mean of the ratio of the potential intensity to the Coriolis parameter and the radial turbulent mixing length, weighted slightly towards the latter. Note that the direct non-dimensional scaling for r_m has an exponent of $\alpha = -.52$ and $r_{adj}^2 = .84$, both statistically indistinguishable from r_{ew} at the 95% confidence level.

Curiously, the power dissipation (Emanuel, 2005) follows the scaling

$$PDI \sim V_m^3 r_m^2 \sim V_p^{4.7} f^{-1.7} l_h^3 \quad (3.17)$$

which exhibits only a very weak dependence on l_h .

3.3.4 Base case: Outer wind field

We may now quantify the scaling of the overall storm size. We reiterate that r_0 is difficult to extract directly from numerical model output, and thus elect to use the analytical outer wind model of Emanuel (2004) to represent the outer circulation. Following the above non-dimensional scaling results, we first non-dimensionalize V by V_p and r by $\frac{V_p}{f}$ in Eq. (3.5), giving

$$\frac{\partial(\tilde{r}\tilde{V})}{\partial\tilde{r}} = \frac{C_d V_p}{w_{cool}} \frac{2\tilde{r}^2 \tilde{V}^2}{(\tilde{r}_0^2 - \tilde{r}^2)} - \tilde{r} \quad (3.18)$$

Table 3.2: Parameter values for each simulation used to test the scaling relationships associated with Eq. (3.12), where $C_1 = \frac{V_p}{f l_h}$. Control values are listed in Table 3.1.

| $f [\times 10^{-5} s^{-1}]$ | $l_h [m]$ | $V_p(T_{tp}) [ms^{-1}]$ | C_1 |
|-----------------------------|-----------|-------------------------|-------|
| 10 | 12000 | 126 | 105 |
| 20 | 6000 | 126 | 105 |
| 10 | 12000 | 50 | 42 |
| 5 | 12000 | 50 | 84 |
| 1.25 | 750 | 126 | 13403 |
| 20 | 6000 | 50 | 42 |
| 1.25 | 750 | 50 | 5386 |
| 1.25 | 375 | 50 | 10772 |
| 2.5 | 750 | 126 | 6701 |
| 2.5 | 1500 | 126 | 3351 |
| 5 | 750 | 126 | 3351 |
| 10 | 3000 | 92 | 306 |
| 5 | 3000 | 50 | 337 |
| 5 | 1500 | 92 | 1225 |
| 5 | 1500 | 58 | 778 |
| 5 | 1500 | 70 | 939 |
| 5 | 1500 | 79 | 1049 |
| 5 | 1500 | 103 | 1369 |
| 5 | 1500 | 116 | 1550 |
| 5 | 1500 | 120 | 1594 |
| 5 | 1500 | 126 | 1675 |
| 1.25 | 1500 | 92 | 4899 |
| 2.5 | 1500 | 92 | 2449 |
| 10 | 1500 | 92 | 612 |
| 20 | 1500 | 92 | 306 |
| 40 | 1500 | 92 | 153 |
| 5 | 375 | 92 | 4899 |
| 5 | 750 | 92 | 2449 |
| 5 | 3000 | 92 | 612 |
| 5 | 6000 | 92 | 306 |
| 5 | 12000 | 92 | 153 |

where tildes denote non-dimensional quantities. Chavas and Emanuel (2010) employed this model to estimate r_0 in observations by fitting the model to the radius of $12 ms^{-1}$. Here we find that Eq. (3.18) can credibly reproduce the entire equilibrium radial wind profile outside of the eyewall for many simulations with a simple empirical

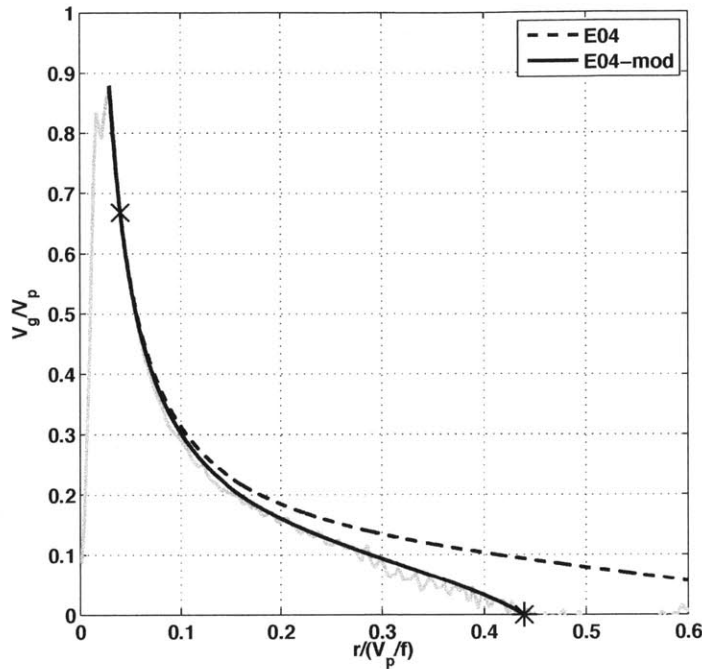


Figure 3-9: Comparison of equilibrium radial wind profile for Control simulation (grey) with Eq. (3.18) without (dashed) and with (solid) constant modification ($c = .3$), fit to $r(.75V_m)$ (marked 'X').

modification of the first term on the RHS of (3.18) by a constant factor, taken here to be $c = .3$. As an example, Figure 3-9 depicts the Control simulation equilibrium profile compared against Eq. (3.18) fit without and with this modification (i.e. $c = 1$ and $c = .3$, respectively). To fit this analytical model, we begin at $r_{ew} = r(.75V_m)$ from the equilibrium radial wind profile and integrate Eq. (3.18), with the first term on the RHS multiplied by $c = .3$, outwards to r_0 . Remarkably, the empirically-modified Eq. (3.18) captures nearly the entire equilibrium radial wind profile beyond r_m . This empirical fit across our simulation sets is explored in the next section.

Outer wind field model fit

The fit of Eq. (3.18) to the equilibrium radial wind profile in the outer region of the storm can be improved significantly by multiplying the first term on the RHS of Eq. (3.18) by a constant. Figure 3-10 shows a histogram of the optimal constant, c , for

Table 3.3: Optimized c for each simulation (see text for details); corresponding histogram is plotted in Figure 3-10. Asterisk denotes a likely outlier.

| T_{sst} | c | u_{sfc} | c | Q_{cool} | c | T_{tpp} | c | l_h | c | $f (\times 10^{-5})$ | c |
|-----------|-----|-----------|-----|------------|-------|-----------|------|-------|-----|----------------------|-------|
| 285 | .4 | 10 | .23 | .25 | .1 | 238 | 2.9* | 375 | .58 | 1.25 | 10.0* |
| 287.5 | .35 | 5 | .21 | .375 | .13 | 225 | .26 | 750 | .83 | 2.5 | 1.06 |
| 290 | .23 | 4 | .26 | .5 | .17 | 213 | .27 | 1500 | .26 | 5 | .26 |
| 292.5 | .17 | 3 | .26 | .75 | .2 | 200 | .26 | 3000 | .41 | 10 | .25 |
| 295 | .3 | 2 | .31 | 1 | .26 | 188 | .26 | 6000 | .35 | 20 | .16 |
| 300 | .26 | 1 | .68 | 1.5 | .31 | 175 | .26 | 12000 | .26 | 40 | .46 |
| 305 | .25 | .5 | .55 | 2.0 | .78 | 163 | .24 | — | — | — | — |
| 310 | .69 | — | — | 3.0 | .96 | 150 | .25 | — | — | — | — |
| — | — | — | — | 4.0 | 10.0* | — | — | — | — | — | — |

each simulation, and the optimal values are provided in Table 3.3. Optimal values are obtained by minimizing the mean square error within the region $r(.1V_m < V < .75V_m)$ over the range $c = [.1, 10]$. The median is $c = .26$, and most simulations lie in the range $c = .2 - .4$, skewed slightly towards higher values. For varying T_{tpp} , all cases are tightly clustered at $c = .25 - .27$, with the exception of $T_{tpp} = 238 K$, which is likely an outlier. Thus, for this work we choose $c = .3$.

Taking $c = .3$, Figure 3-11 displays the radial profile of the error, defined as $V_{E04} - V_{CM1}$, for all simulations varying each of the six relevant dimensional parameters. Mean absolute errors are less than $2 ms^{-1}$ across most simulations. The most significant deviation occurs for Q_{cool} , which exhibits a systematic trend in mean error that reflects an overestimation of the wind field at low cooling rates and an underestimation at high cooling rates, indicating that the sensitivity to w_{cool} is not as strong in the numerical model as would be predicted by Eq. (3.18). This behavior is also reflected in the steady increase in the optimal value of c in Table 3.3 for radiative cooling rates of $.375 - 1.5 K day^{-1}$. More precisely, increasing Q_{cool} (and thus w_{cool}) by a factor of 4 over this range corresponds approximately to a doubling in c , suggesting that the sensitivity of the true radial wind profile to the radiative-subsidence rate is overestimated by a factor of two. At very high radiative cooling rates, convection progressively increases beyond the eyewall region such that the entire wind field ex-

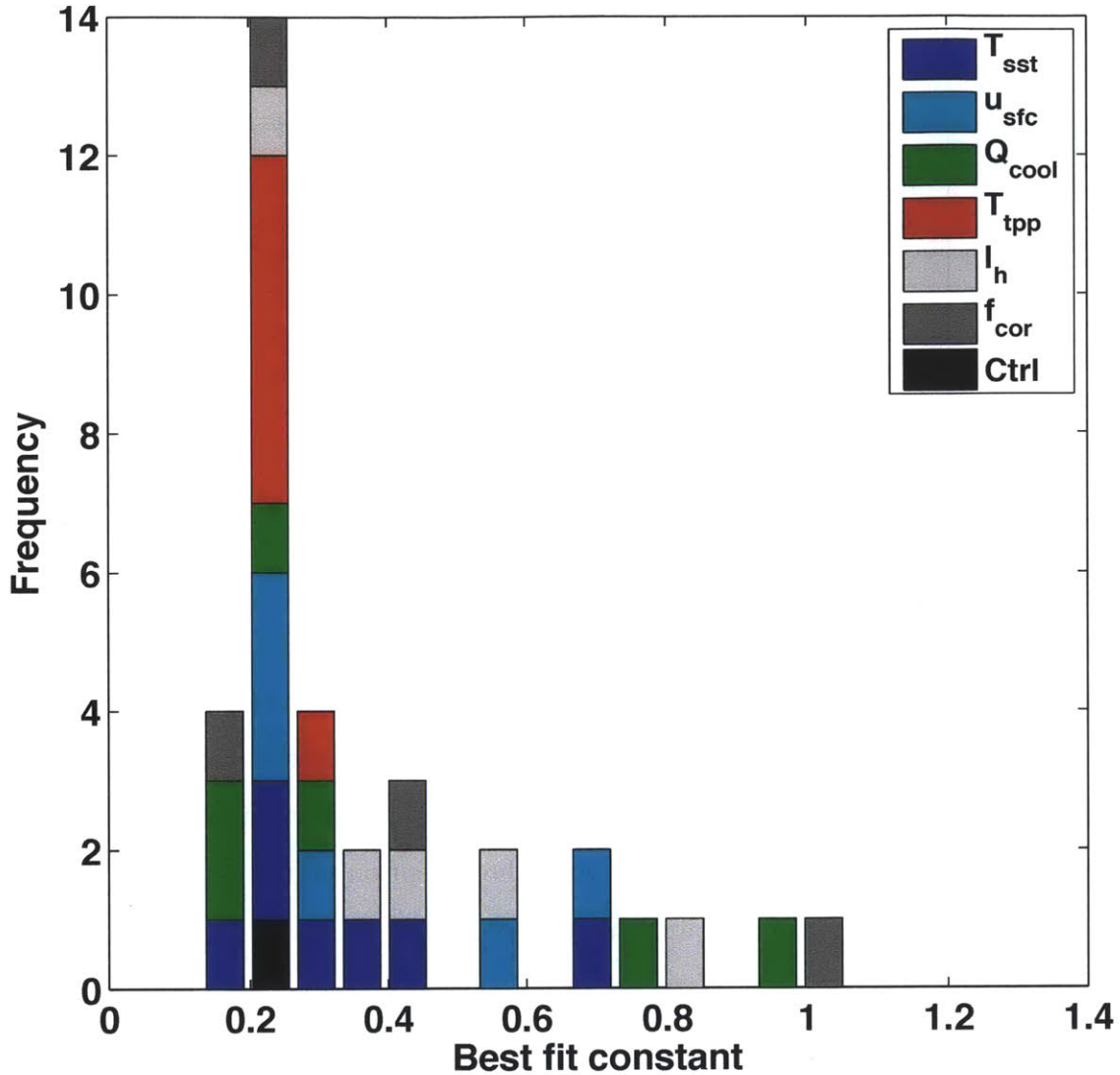


Figure 3-10: Histogram of optimized constant, c , applied to first term on the RHS of Eq. (3.18) across simulation sets (color). Control simulation is in black. The values are calculated by fitting Eq. (3.18) to $r(.75V_m)$ and then minimizing the mean square error in the region $r(.1V_m < V < .75V_m)$. Values are tested over the range $c = [.1, 10]$. The median is $c = .26$.

pands significantly and the analytical model provides a poor fit due to the significant mismatch in the vicinity of r_{ew} .

Nonetheless, the broad success of this simple empirical modification indicates that this analytical model, despite its simplicity and many documented deficiencies in the inner core of a TC (Smith and Montgomery, 2008; Persing and Montgomery, 2003;

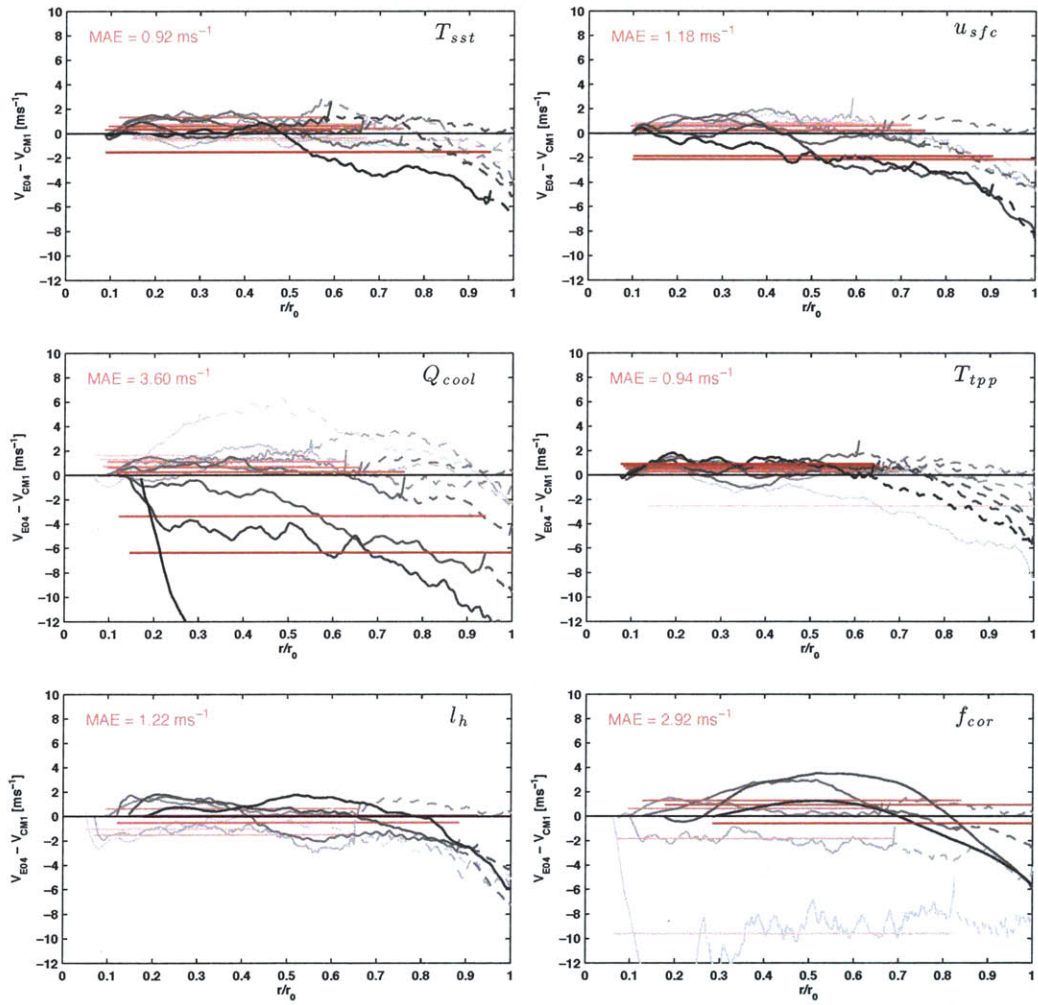


Figure 3-11: Radial profiles of error in the fit of the analytical outer wind model (Eq. (3.18), empirically modified with $c = .3$) to the equilibrium radial wind profile, defined as $V_{E04} - V_{CM1}$, for all simulations varying each of the six relevant dimensional parameters. Error profiles are smoothed with a 10-pt smoother. In the top four panels, shading reflects potential intensity from low (light grey) to high (black); in the bottom two panels, shading reflects parameter magnitude from low (light grey) to high (black). Analytical model is fit to $r(.75V_m)$, with the range $r(.75V_m < V < .1V_m)$ solid and $r(V < .1V_m)$ dashed; radii are normalized by r_0 as calculated from the outer wind model given by Eq. (3.18). Red line depicts mean error over the inner range, and the corresponding mean absolute error (MAE) for the simulation set is listed in the top left corner.

Smith and Vogl, 2008), likely captures the essential physics of the equilibrated, non-convecting outer circulation at least within the idealized approach employed here. Ultimately, this simple slab boundary layer model, which is derived from a balance between the net convergence of angular momentum by the radial wind in the boundary layer and its frictional sink at the surface, assumes that all quantities, such as V and $u \frac{\partial M}{\partial r}$, are constant with height below $z = 1.56 \text{ km}$. The cumulative effect of violations of these assumptions will manifest itself as a misfit between Eq. (3.18) and the “true” equilibrium wind profile. Because Eq. (3.18) is derived from a simple two-term balance between radial advection of angular momentum and frictional loss of angular momentum at the surface, this misfit may be represented simply by a single multiplicative factor. Why this factor should remain roughly constant both with radius and across many simulations is not obvious, and a preliminary analysis of the model assumptions (not shown) reveals no single, dominant assumption that is consistently violated and from which an improved theoretical model might be developed.

Thus, for our purposes, we elect simply to use $c = .3$, noting that the scaling results are not sensitive to the precise value chosen. Though one may be tempted to optimize the value of c for each individual simulation, such an approach introduces an additional degree of freedom that, absent an underlying theoretical justification, will add additional complexity to the problem with minimal new physical insight. A deeper analysis of the physics behind this empirical modification, and of the validity of this model more generally in the outer non-convecting region of the storm circulation, is an important endeavor for future work.

Outer radius

We apply Eq. (3.18) with the aforementioned empirical modification to estimate the outer radius and to explore variability in the outer region of the equilibrium radial wind profiles.

The top panel of Figure 3-12 displays outer radial wind profiles for varying T_{tpp} , normalized as in Figure 3-6. Overlaid on top of these radial profiles are the solutions of Eq. (3.18), each of which provide an estimate of the outer radius, r_0 (blue dots).

The scaling of r_0 with V_p is shown as an inset. As noted earlier, the normalized equilibrium radial wind profiles exhibit a systematic expansion of the far outer wind field with increasing V_p , a qualitative behavior that is correctly predicted by Eq. (3.18).

Indeed, Eq. (3.18) is itself modulated by a second non-dimensional parameter, C_2 , given by

$$C_2 = \frac{C_d V_p}{w_{cool}} \quad (3.19)$$

We may quantify the impact of C_2 by simply holding it fixed at its Control value (53) when solving Eq. (3.18); the result is shown in the bottom panel of Figure 3-12. Comparison of the red curves in the top and bottom panels of Figure 3-12 reveals that the effect of C_2 manifests itself primarily only at large radii in the far outer region of the storm circulation. Additionally, these new curves provide an estimate of an adjusted outer radius, r_0^* (blue dots, bottom panel), which is analogous to r_0 but with C_2 fixed at its Control value. The scaling of r_0^* with V_p is shown as an inset. Physically, fixing C_2 acts to partially collapse the curves in the far outer region, reducing 80% of the variance in the normalized outer radius.

Though the influence of C_2 is minimal at smaller radii where wind speeds are an appreciable fraction of the maximum value, it exerts a significant influence on the precise value of r_0 . This is of particular importance given that C_2 includes a factor V_p . As a result, the true r_0 is a function of C_1 and C_2 , both of which include variability with V_p , one of our critical dimensional parameters.

Thus, Figure 3-13 displays the joint scaling of r_0 with C_1 and C_2 over a wide range of values of each. The values of r_0 are calculated beginning with the empirically-derived relationships for $\frac{V_m}{V_p}$ (exponential) and $r_{ew}/\frac{V_p}{f}$ (power-law) as a function of C_1 displayed in Figure 3-8 and given by

$$\frac{V_m}{V_p} = -.3 + .37 \times \log_{10}(C_1) \quad (3.20a)$$

$$\frac{r_{ew}}{\frac{V_p}{f}} = 0.73 C_1^{-.55} \quad (3.20b)$$

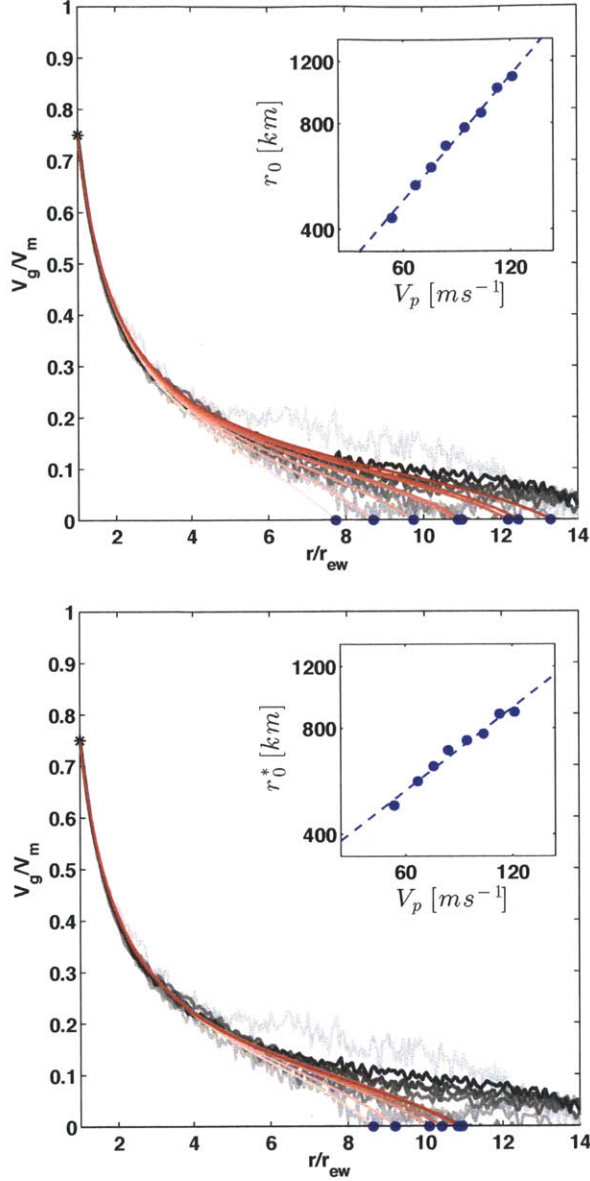


Figure 3-12: As in Figure 3-6 for varying T_{tpp} , focused on the outer region of the storm. Black curves are the equilibrium radial wind profiles; red curves are solutions of Eq. (3.18) fit directly (top), and fit with $\frac{C_d V_p}{w_{cool}}$ held fixed at its Control value (bottom). Blue dots indicate corresponding r_0 (top) and r_0^* (bottom), and the corresponding scalings with V_p are shown as insets.

Then, for each C_1 , Eq. (3.18) is applied to the corresponding $(r_{ew}/\frac{V_p}{f}, \frac{V_m}{V_p})$ using a range of values of C_2 . In this way, we exploit the fact that the direct impacts of C_1 and C_2 are effectively independent in radius, with the former modulating the inner core

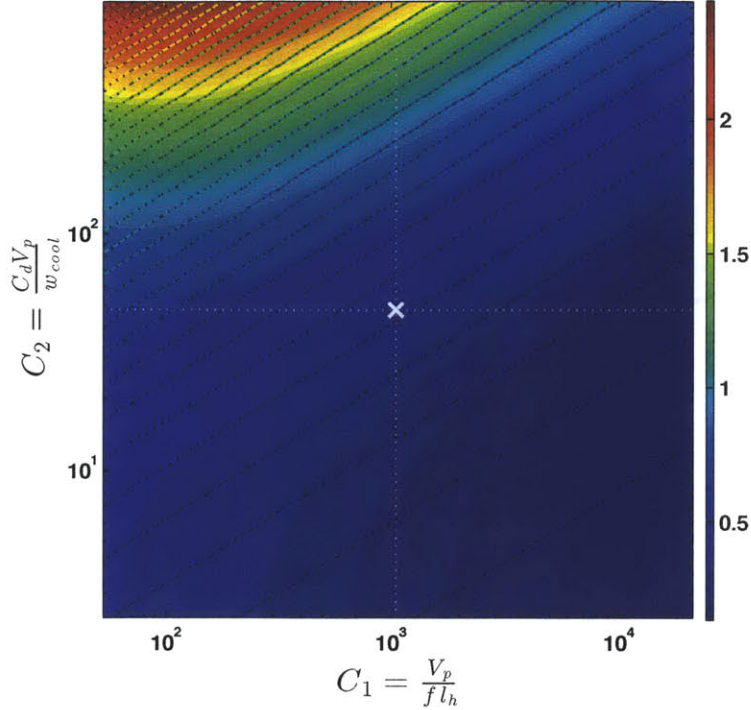


Figure 3-13: Scaling of $r_0/\frac{V_p}{f}$ with C_1 and C_2 , calculated using Eq. (3.18) with empirical fit to simulation results. Marker ('X') denotes Control simulation. Contours depict power law scaling fit given by Eq. (3.21).

of the storm and the latter modulating the outer circulation. The non-dimensional outer radius decreases slowly with increasing C_1 and increases more quickly with increasing C_2 , particularly at high values. Additionally, there is non-linearity in the joint scaling for small C_1 and large C_2 , which is associated with the more rapid decline of the exponential relationship for $\frac{V_m}{V_p}$ (Eq. (3.20a)) at very small C_1 .

To quantify the variation of non-dimensional r_0 with C_1 and C_2 , a simple estimate of the separable power-law scaling can be obtained using multiple linear regression. The result is given by

$$\frac{r_0}{\frac{V_p}{f}} \sim C_1^{-.2} C_2^{.33} \quad (3.21)$$

and is plotted (contours) in Figure 3-13. This statistical fit performs reasonably well except in regions of significant curvature, i.e. for small C_1 and large C_2 and vice versa. Notably, there is minimal curvature in the neighborhood of the Control simulation.

Additionally, we may probe the scaling with C_1 and C_2 independently. First, the

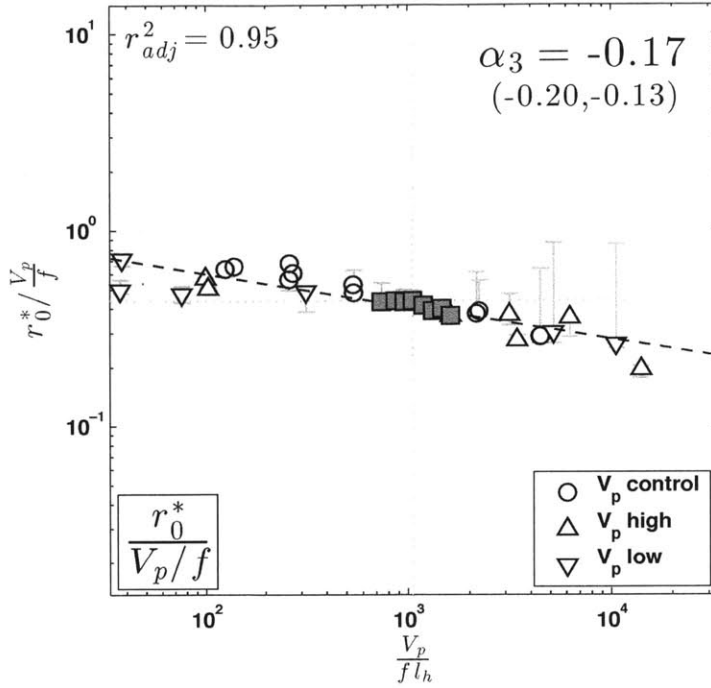


Figure 3-14: As in Fig. 3-8 but for overall storm size, r_0^* , with C_2 fixed at the Control value.

scaling of the non-dimensional outer radius with C_1 while holding C_2 fixed at its Control value, which corresponds to r_0^* in Figure 3-12, is equivalent to the application of dimensional analysis to r_0^* as was done above for V_m and r_{ew} . Indeed, the direct estimate of the non-dimensional scaling for r_0^* is shown in Fig. 3-14. The empirically-derived power law scaling exponent is -0.15 , which closely matches the result from multiple linear regression over the combined (C_1, C_2) parameter space given in Eq. (3.21). The corresponding dimensional scaling is

$$r_0^* \sim \left(\frac{V_p}{f} \right)^{.85} (l_h)^{.15} \quad (3.22)$$

Thus, Eq. (3.22) dictates that, at fixed C_2 , overall storm size is found to scale nearly linearly with the ratio of the potential intensity to the Coriolis parameter, with a slight expansion for increasing radial turbulent mixing length. This scaling matches the existing axisymmetric theoretical prediction for the scaling of the upper bound

on the size of a tropical cyclone (Emanuel, 1986, 1989, 1995a). This “natural” length scale is $\frac{\sqrt{\chi_s}}{f}$, where $\sqrt{\chi_s}$ is a velocity scale that is equivalent to the potential intensity with $C_k = C_d$ and neglecting dissipative heating and the pressure dependence on the saturation vapor pressure of water. As first described in Emanuel (1986), the existence of this theoretical upper bound is most easily understood from the perspective of a Carnot heat engine, in which the work required to restore lost angular momentum in the anticyclone aloft increases with increasing storm size, and by conservation of energy there remains less energy available to overcome frictional dissipation at the surface, i.e. a weaker storm. To the extent that the inclusion of the pressure dependence of saturation vapor pressure and dissipative heating do not alter this fundamental principle, our modeling results appear to confirm this prediction.

Meanwhile, the scaling of the non-dimensional outer radius with C_2 while holding C_1 fixed at its Control value represents an expansion of the far outer circulation, whose scaling is $C_2^{.33}$, above and beyond this primary storm scaling associated with C_1 . Importantly, in order to isolate the theoretical scaling of (Emanuel, 1986) in a dimensionally-consistent manner, one must first hold C_2 constant, as we have done in calculating r_0^* ; this seems reasonable given that the theory is applicable only to the ascending region of the storm and so should not be expected to represent variability in the non-convecting outer circulation. Moreover, the scaling result for r_0^* is very similar when applying Eq. (3.18) beginning at $r(.2V_m)$ (scaling exponent of $-.11$), as shown in Figure 3-15, indicating that this result is not an artifact of the analytical outer wind model.

3.3.5 Physical interpretation

More generally, the non-dimensional parameter, C_1 , represents the ratio of the storm radial length scale, $\frac{V_p}{f}$, to the parameterized eddy radial length scale, l_h , and thus it is the values of each of these parameters relative to one another, rather than their absolute values, that is fundamental to the structure of the storm. For example, though one would expect V_m to scale linearly with V_p all else equal, the super-linearity is a manifestation of the fact that a larger value of V_p results in a storm that is

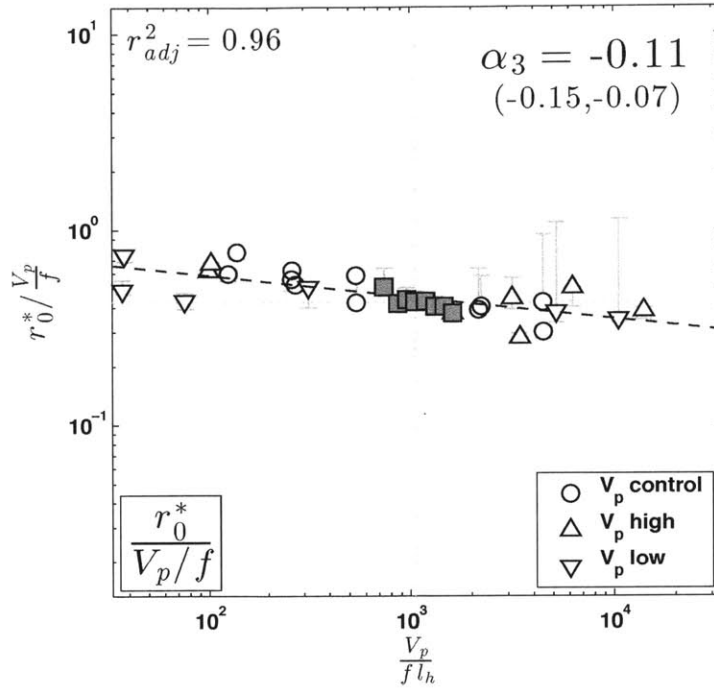


Figure 3-15: As in Fig. 3-14 but with r_0^* calculated by applying (3.18) to the numerical equilibrium solution beginning at $r(.2V_m)$.

more intense *and* larger. Because radial turbulence acts to reduce radial gradients in scalars such as temperature (and thus gradient azimuthal wind speed, through gradient thermal wind balance) over a distance proportional to the prescribed mixing length, a larger storm at constant l_h implies a reduction in C_1 , and thus the storm will feel a weaker effective turbulence. Indeed, from (3.14) for constant C_1 we do indeed recover the linear scaling $V_m \sim V_p$.

In addition, these findings corroborate prior work demonstrating the importance of radial turbulence in determining inner-core storm structure (Bryan and Rotunno, 2009a; Bryan, 2011; Rotunno and Bryan, 2012). In particular, the strong scaling relationship between r_m and l_h reflects the critical role of radial turbulence in counteracting eyewall frontogenesis by the secondary circulation that, in the inviscid limit, would lead to frontal collapse (Emanuel, 1997). Meanwhile, the influence of radial turbulence as parameterized here only weakly modifies storm structure near the outer edge of the storm.

Notably, the combination of f and l_h in the denominator suggests that, in the inner core of the non-dimensional system, both variables are dynamically equivalent. This notion appears reasonable given that both variables modulate the eyewall structure (Figure 3-6) in an identical manner such that the two-hump structure is replaced by a single hump as either parameter progressively increases in magnitude.

Meanwhile, C_2 represents the reciprocal of the non-dimensional Ekman suction rate in the outer wind region, where the requirement that $w_{Ek} = w_{cool}$ has been imposed. This can be seen more clearly by deriving Eq. (3.18) starting explicitly from the definition of the Ekman suction velocity, given by the divergence of the frictionally-induced inflow, u , integrated over the boundary layer depth, h ,

$$w_{Ek} = \int_0^h \frac{1}{r} \frac{\partial(ru)}{\partial r} \partial z \quad (3.23)$$

and non-dimensionalizing as above. Combining Eq. (3.23) with u derived from angular momentum balance in the boundary layer leads to an expression for $\frac{w_{Ek}}{C_d V_p}$ that can be rearranged to give Eq. (3.18) (this scaling for w_{Ek} also appears in the traditional Ekman solution for a vertically-uniform boundary layer, which corresponds to this same derivation for Eq. (3.18) but in the limit $rV \ll \frac{1}{2}fr^2$, i.e. near r_0). Physically, decreasing the Ekman suction rate implies through Ekman dynamics a weaker (negative) vorticity and thus a more gradual decay of the radial wind profile. In non-dimensional space, the non-dimensional suction rate can be decreased either by decreasing w_{cool} , which by assumption implies a smaller dimensional w_{Ek} , or by increasing the scaling factor $C_d V_p$. In this way, C_2 governs the rate of decay of the wind profile with radius at large radii in the non-dimensional system.

3.3.6 Estimating l_h

Given the sensitivity of the equilibrium structure, particularly r_m , to the turbulent radial mixing length, an accurate estimation of l_h in the inner core of a real tropical cyclone is important but lacks any theoretical or observational foundation, as it is not a physical parameter that can be determined as a function of physically calcu-

lable natural variables. Bryan and Rotunno (2009b) and Bryan (2011) attempt to estimate its value by tuning it to match the steady-state model intensity to either the theoretical potential intensity or the theoretical maximum gradient wind speed of Emanuel and Rotunno (2011). We note here that the theory of Emanuel and Rotunno (2011) does not include the effect of radial turbulence, so it is not clear whether it is the appropriate quantity against which to tune. Nonetheless, the above results suggest that the more relevant objective is to tune the ratio $\frac{V_m}{V_p}$ to the horizontal mixing length non-dimensionalized by the storm scale $\frac{V_p}{f}$ (i.e. the reciprocal of C_1). We thus estimate this parameter value as that which gives the theoretical result from Emanuel and Rotunno (2011) of $\frac{V_m}{V_p} = \frac{1}{\sqrt{2}}$ in the case of $\frac{C_k}{C_d} = 1$, as shown shown in Figure 3-16. Given that this exercise favors statistical precision over theoretical insight, we perform this estimation using the logarithmic rather than the power law fit to the data. The resulting best estimate is $\frac{l_h}{V_p/f} = .0017$, or approximately $\frac{1}{600}$ of the storm radial length scale. For our Control values for V_p and f , this result translates to $l_h \approx 2700$ m. This value seems reasonable in the context of previous work that finds optimal values in the range 1000 – 1500 m given that those simulations were performed in domains approximately half the size required to avoid influencing storm size (Figure 3-2).

3.3.7 Sensitivity to potential intensity

We now return to the hypothesis that the sensitivity of storm structure to each of the four thermodynamic parameters collapses to a sensitivity to potential intensity. Figure 3-17 displays the respective scalings of V_m , r_{ew} and r_0^* with V_p . Indeed, across all four parameters there is a systematic, direct scaling with V_p in both intensity and size, with several interesting deviations. Implicitly, any variability above and beyond the scaling with $V_p(T_{tpp})$ is necessarily a result of modulation of some other aspect of the system that is correlated with V_p . For V_m , the slightly super-linear scaling with V_p matches that found for T_{tpp} in all cases with the exception of u_{sfc} , for which the scaling is more gradual, and at high values of Q_{cool} . For r_{ew} , the scaling with V_p for both u_{sfc} and Q_{cool} is faster than for T_{tpp} , and the scaling diverges non-linearly at

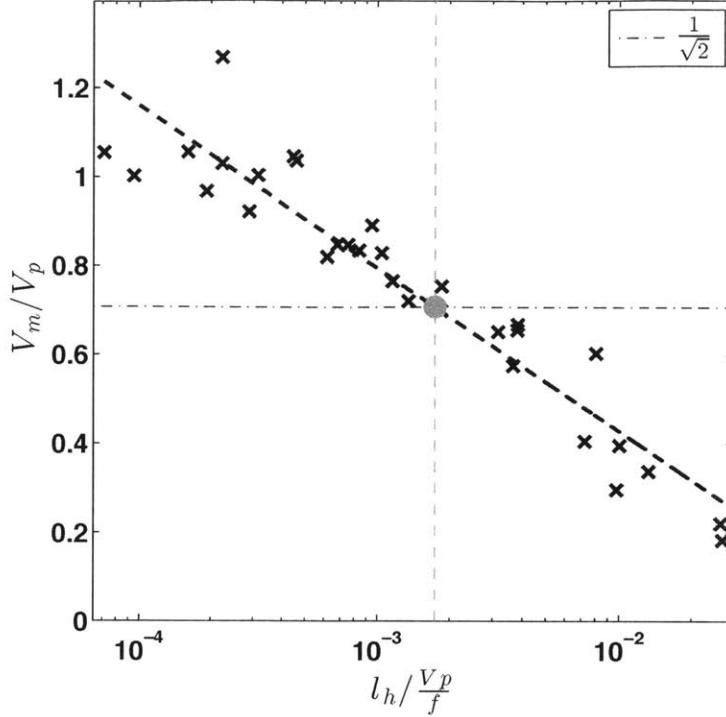


Figure 3-16: Estimation of the optimal value of the radial mixing length normalized by $\frac{V_p}{f}$ by matching the logarithmic fit to the data (black dash) to the theoretical relationship of $\frac{V_m}{V_p} = \frac{1}{\sqrt{2}}$ (black dash-dot) for $\frac{C_k}{C_d} = 1$ in Emanuel and Rotunno (2011). The best estimate (grey dot) is approximately $\frac{1}{600}$ of the storm scale.

very high radiative cooling rates. Finally, for r_0^* (the outer radius at fixed C_2), the scalings largely collapse with the exception of high radiative cooling rates as was seen for r_{ew} . The two cases with coldest T_{sst} (285, 287.5 K) do not conform well to the overall scaling but instead are weaker and smaller than expected given their potential intensities, though these simulations exhibit significant ongoing variability during the post-equilibration period.

For r_0^* , we may also apply our analytical model beginning at much larger radii to test the sensitivity of the scaling result to the use of (3.18). Figure 3-18 displays the scaling for r_0^* where we apply (3.18) beginning at $r(.2V_m)$. The result is very similar to the original result, reflecting the fact that (3.18) does a reasonable job representing the radial wind profile radially-inwards of $r(.2V_m)$ (Figure 3-11)

Additionally, we may calculate r_0^* using the optimized values of c specific to each

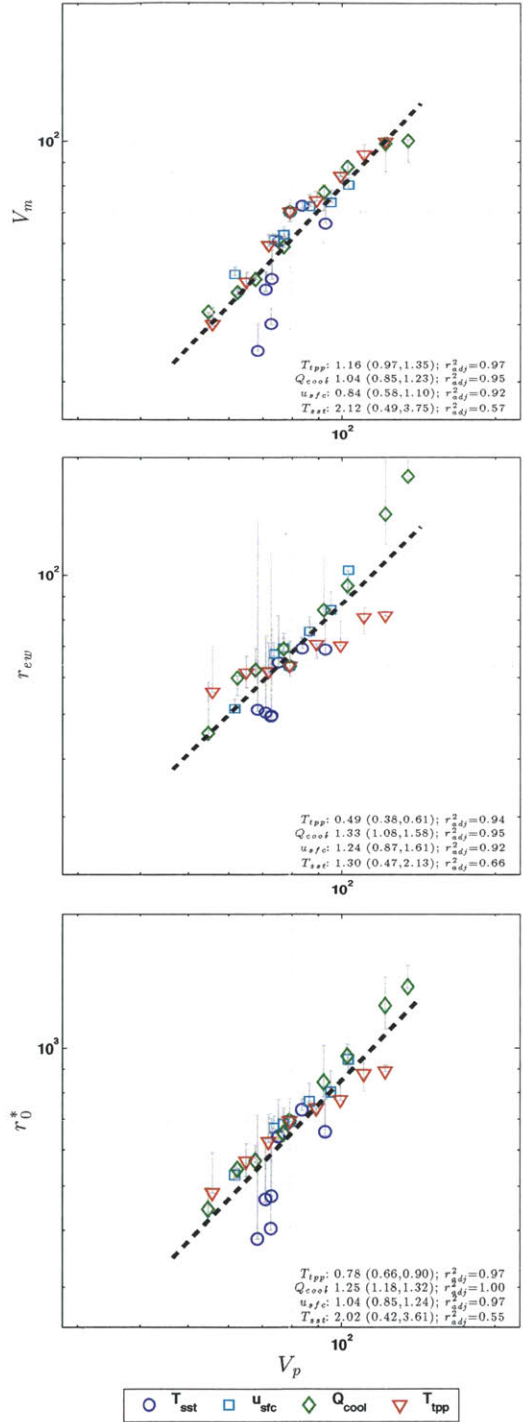


Figure 3-17: Scaling of the respective equilibrium values of V_m , r_{ew} , and r_0^* (ordinate) with V_p (abscissa) for the four thermodynamic parameters. Dashed line indicates best fit to all data. For each individual parameter, best fit linear slope (95% CI) and corresponding adjusted r-square statistic listed in lower right corner. Grey bars indicate the full range of variability of the 30-day running mean after day 60.

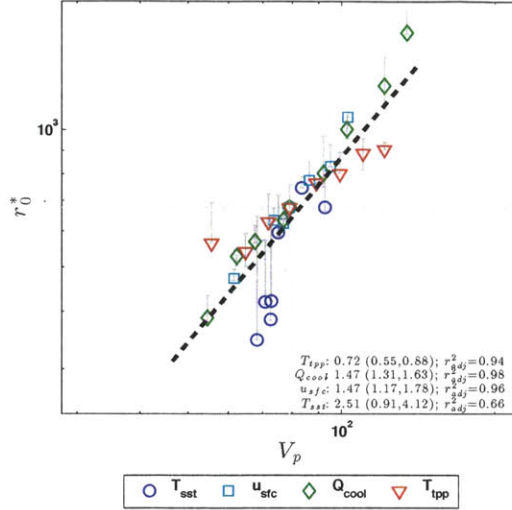


Figure 3-18: As in Fig. 3-17 but with r_0^* calculated by applying (3.18) to the numerical equilibrium solution beginning at $r(.2V_m)$.

simulation, as shown in Figure 3-19. The overall scaling with V_p is preserved, though the scaling appears to be more rapid for u_{sfc} and Q_{cool} than in the original case. However, it is important to note that variations in c are mathematically equivalent to variations in C_2 , and therefore r_0^* is no longer a function solely of C_1 . It is likely that variations in c actually reflect variations in the true dependence on the factors that comprise C_2 (or some other, more complex set of factors) that may not be properly captured by such a simple model as (3.18) and thus for which we cannot control, except by setting the product $c \times C_2$ constant at the Control value as we have done in Figures 3-17 and 3-18. Moreover, the data overall may be noisier (e.g. the excluded outlier at the warmest value of T_{tpp}), as the estimate of c will be sensitive to long-period variability in storm structure at large radii approaching $r(.1V_m)$; subsequently, r_0 is quite sensitive to c . This is again an indication that a more complete understanding of the validity of (3.18) in the outer region would be highly beneficial for determining the precise nature of the variability far outer wind field. Nonetheless, the consistent signal of the scaling of overall storm size with V_p is insensitive to these details.

In combination, these results indicate that storm structure scales predominantly with V_p , though the inner core of the storm has a tendency to expand more rapidly for

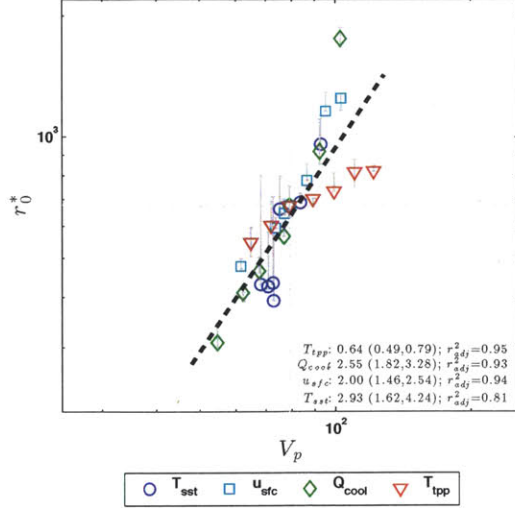


Figure 3-19: As in Fig. 3-17 but with r_0^* calculated from (3.18) using the optimal value of c specific to each simulation. Two cases ($T_{tpp} = 238 \text{ K}$, $Q_{cool} = 4 \text{ K day}^{-1}$) have very large values of c (Table 3.3) and are filtered out as outliers.

increasing Q_{cool} and u_{sfc} than what is expected from increasing V_p alone, particularly for very high radiative cooling rates at which the size of the entire storm (both r_{ew} and r_0) increases. The scaling for r_{ew} necessarily integrates the variability of the eye and eyewall together. To isolate effects associated solely with the eye, we also extract from the equilibrium storm structure the counterpart to r_{ew} (i.e. $r(.75V_m)$) that lies within the eye, which we denote r_e . Figure 3-20 displays the scaling of the ratio of r_e to r_{ew} with V_p . Positive slope indicates that the eye is expanding relative to r_{ew} for increasing V_p , whereas zero slope indicates that the entire inner core structure of the storm scales uniformly. There are two prominent deviations from zero.

First, u_{sfc} exhibits a statistically-significant positive scaling with an estimated slope of .5. Indeed, one can observe in Figures 3-5 and 3-6 a distinct difference in the behavior of the eye as compared to T_{tpp} , such that the radial wind profile in the eye expands outward as the gustiness is decreased. This expansion of the eye, which is positively correlated with the expansion associated with increasing V_p , may explain the difference in the scaling of r_{ew} between u_{sfc} and T_{tpp} noted earlier.

Second, Q_{cool} exhibits a substantial expansion of the eye, but only for large radiative cooling rates. The strange behavior in the eye is evident in Figure 3-5, as the

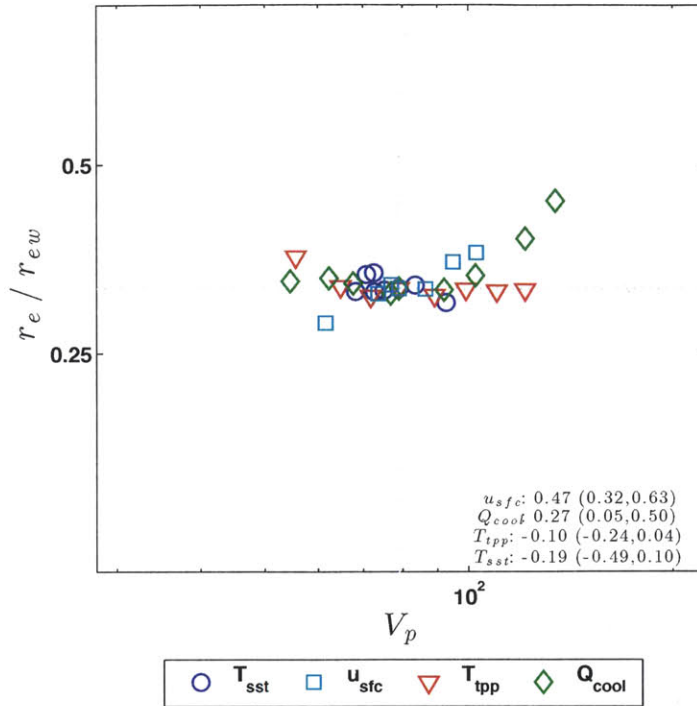


Figure 3-20: As in Figure 3-17, but for the scaling of the ratio of r_e to r_{ew} . Positive slope indicates that the eye is expanding relative to the width of the eyewall.

inner edge of the eyewall is rapidly pushed to larger radii. In the normalized plots in Figure 3-6, this behavior manifests itself as the progressive erosion of the inner hump in the two-humped structure of the gradient wind profile in the eyewall region. At equilibrium, the eye above the boundary layer is characterized by radiative-subsidence balance, which, coupled with Ekman upwelling within the boundary layer, necessarily implies from mass continuity an outward mass flux above the boundary layer that should act to push the eyewall radially outwards. One expects that this mass flux would scale with the radiative subsidence rate and thus with the radiative cooling rate, but why this effect appears prominent only for high cooling rates is unclear.

As noted above, both r_{ew} and r_0^* expand at high radiative cooling rates. This may be due to the development of significant convection beyond the eyewall, which may cause an expansion of the wind field (Hill and Lackmann, 2009) and also likely explains the poor fit of the analytical outer wind model to the equilibrium radial wind profile near r_{ew} in these cases. It should be noted, though, that the variability in storm

structure increases significantly at these more extreme conditions. For the largest radiative cooling rate (4 K day^{-1}), the storm develops wind maxima at radii around 1000 km before eventually developing a more traditional radial wind structure only around day 120. More generally, this behavior may reflect the fact that in radiative-convective equilibrium, precipitation must balance free tropospheric radiative cooling. Thus, total precipitation necessarily must increase with Q_{cool} , but given constraints on the terminal velocity of raindrops (to which V_m was found to be sensitive in Bryan and Rotunno (2009a)) as well as the decrease in boundary layer water vapor mixing ratio with increasing Q_{cool} , this implies that the areal coverage of precipitation may necessarily increase, which may result in a larger storm. At sufficiently high values of Q_{cool} , a precipitation distribution that is confined to the eyewall region, as it appears to be in typical axisymmetric simulations, may no longer be sufficient to balance radiative cooling, and thus convection will necessarily develop at larger radii. A more detailed analysis of this hypothesis is beyond the scope of this work.

3.3.8 Rossby deformation radius

Given that the structure of a tropical cyclone is characterized by a warm anomaly embedded within a rotating fluid, one potentially-relevant length scale from conventional geostrophic adjustment theory that has not been discussed to this point is the Rossby deformation radius, defined as

$$L_R = \frac{N_v H}{f} \quad (3.24)$$

where $N_v^2 = \frac{g}{\theta_v} \frac{\partial \theta_v}{\partial z}$ is the buoyancy frequency, θ_v is the virtual potential temperature, and H is the fluid depth (Emanuel (1994), p. 166). One plausible explanation for the finding that the relevant storm length scale is $\frac{V_p}{f}$ is that this quantity simply covaries with the deformation radius. Indeed, in a three-dimensional rotating radiative-convective equilibrium simulation, Held and Zhao (2008) noted a scaling for the size of their tropical cyclone that was consistent with either L_R or $\frac{V_p}{f}$ but could not distinguish between the two based on the given parameter space. Here we test this

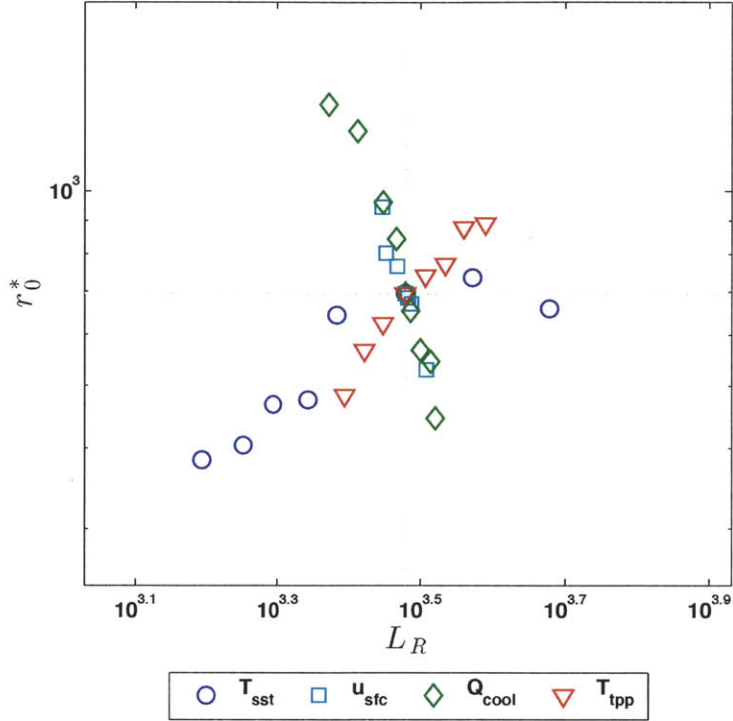


Figure 3-21: As in Figure 3-17, but for the scaling of r_0^* with the Rossby deformation radius.

hypothesis in Figure 3-21, which is analogous to the bottom panel of Figure 3-17 but for the scaling of r_0^* with L_R rather than V_p (which is equivalent to $\frac{V_p}{f}$ since f is fixed). The deformation radius is calculated from the background state vertical profiles of potential temperature and water vapor, where H is the depth of the troposphere, taken to be the linearly-interpolated altitude where the temperature first drops below T_{tpp} , and N_v is taken as the tropospheric pressure-weighted mean. In the case of varying T_{sst} and T_{tpp} , r_0^* indeed scales in the same direction for both L_R and V_p . In contrast, the scaling of r_0^* with u_{sfc} and Q_{cool} is of the opposite sign. Taken together, Figure 3-21 suggests that L_R is not fundamental to the scaling of the equilibrium storm, noting that this conclusion applies equivalently to V_m and r_m given that both exhibit similar qualitative scaling behavior (i.e. positive and monotonic with V_p).

Physically, the distinct scaling relationship of these two parameters is the manifestation of their convenient effect on our idealized RCE state: an increase in Q_{cool} and a decrease in u_{sfc} both act to increase the air-sea thermodynamic disequilibrium,

$k_s^* - k$, which increases V_p (Eq. (3.11)) while simultaneously decreasing N_v and H . This latter effect is explained as follows: in our idealized set-up, the requirement of column energy balance between surface enthalpy fluxes (Eq. (3.2)) and net radiative cooling (Eq. (3.9)) reduces to a mutual constraint on $k_s^* - k$, u_{sfc} , and Q_{cool} ; the effects of the associated changes in ρ , Δp , and the mean resolved wind speed are relatively small. Thus, decreasing u_{sfc} at constant Q_{cool} necessitates an increase in $k_s^* - k$ in order to maintain constant surface enthalpy fluxes, as does increasing Q_{cool} at constant u_{sfc} in order to increase surface enthalpy fluxes to match the enhanced radiative cooling. In either case, an increase in the air-sea thermodynamic disequilibrium at constant T_{sst} implies a decrease in the specific humidity at the lowest model level and of the boundary layer overall. Given that the RCE state is constrained to approximately follow a moist adiabat associated with some measure of the sub-cloud layer entropy (Betts, 1986) and, moreover, that the air-sea disequilibrium is predominantly in the form of latent heat, N_v is directly proportional to the sub-cloud layer specific humidity. Furthermore, for fixed T_{tpp} , H scales with the mean lapse rate, which is proportional to N_v . Thus, decreased sub-cloud layer water vapor translates to a decrease in N_v and H and therefore, given fixed f , a decrease in L_R .

Additionally, $L_R = 0$ for the case of a dry tropical cyclone, which would preclude its existence if L_R were indeed the fundamental length scale. Yet Mrowiec et al. (2011) demonstrated a quasi-steady dry tropical cyclone in an axisymmetric model, and we have successfully generated a quasi-steady dry storm in this modeling environment as well. Figure 3-22 (left) displays the time-evolution of the radial profile of the full azimuthal wind speed at $z = 1.5 \text{ km}$ for a dry version of the Control simulation. This dry simulation is initialized using the RCE sounding calculated from the analogous small-domain three-dimensional simulation absent any water, and no initial disturbance is input. The dry case is more variable than its moist counterpart, though the wind field remains reasonably steady for days 80-140. The time-mean radial wind profile averaged over days 100-130 is also shown in Figure 3-22 (right).

The higher degree of variability in the dry case is likely due to the fact that in dry RCE, the static stability is zero, and thus radiative cooling cannot be balanced

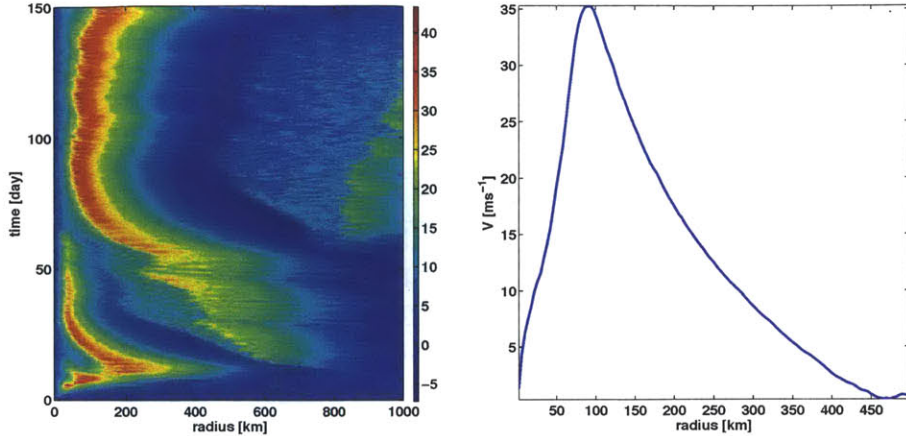


Figure 3-22: Left: Time-evolution of the radial profile of the full azimuthal wind speed at $z = 1.5$ km for a dry version of the Control simulation. Right: Time-mean radial wind profile averaged over days 100-130.

by subsidence warming. Instead, it can only be balanced by convection, including in regions that are typically convection-free in the moist case, such as inside the eye and perhaps in the subsiding region within the outer region of the storm (though here the storm itself may generate positive static stability). Furthermore, in contrast to the moist case, the dry case must be characterized by updraft-downdraft symmetry, yet the distribution of convection in a moist TC is typically concentrated into a small region within the eyewall. Both differences may explain the existence of a secondary wind maximum just beyond the edge of the primary TC ($r \approx 800$ km) in Figure 3-22, a feature that is not typically observed in the moist simulations. A deeper analysis of the differences between the dry and moist simulations may prove to be quite insightful and is left to future work; here we simply note that such a dry storm can indeed be generated in this modeling environment.

3.4 Varying $\frac{C_k}{C_d}$

Beyond the non-dimensional parameters identified above, an additional non-dimensional parameter of interest is the ratio of the surface exchange coefficients of enthalpy and momentum, $\frac{C_k}{C_d}$. Though current theory suggests that it is only their ratio that is relevant to storm structure, here we perform tests varying both C_k and C_d indepen-

Table 3.4: Simulations varying either C_k or C_d and the corresponding values for the potential intensity and for the value of the horizontal mixing length used in order to fix $\frac{V_p}{fl_h}$ to its Control value.

| $C_k [\times 10^{-3}]$ | $C_d [\times 10^{-3}]$ | $\frac{C_k}{C_d}$ | $V_p [ms^{-1}]$ | $l_h [m]$ |
|------------------------|------------------------|-------------------|-----------------|-----------|
| 0.75 | 1.5 | .5 | 80 | 1316 |
| 1.5 | 1.5 | 1 | 92 | 1500 |
| 3 | 1.5 | 2 | 105 | 1720 |
| 6 | 1.5 | 4 | 124 | 2026 |
| 12 | 1.5 | 8 | 155 | 2532 |
| 1.5 | 2.12 | .71 | 76 | 1247 |
| 1.5 | 1.5 | 1 | 92 | 1500 |
| 1.5 | 1.06 | 1.41 | 110 | 1800 |
| 1.5 | 0.75 | 2 | 133 | 2180 |
| 1.5 | 0.53 | 2.82 | 161 | 2642 |
| 1.5 | 0.375 | 4 | 201 | 3284 |
| 1.5 | 0.1875 | 8 | 261 | 4276 |
| 1.5 | 0.0938 | 16 | 346 | 5672 |
| 1.5 | 0.0625 | 24 | 449 | 7359 |

dently, spanning a large range of values of $\frac{C_k}{C_d}$: the range of C_k is $.75-12 \times 10^{-3}$ (i.e. $\frac{C_k}{C_d}$ spans $\frac{1}{2}$ -8x the Control value) and the range of C_d is $.0625-2.1 \times 10^{-3}$ (i.e. $\frac{C_k}{C_d}$ spans $\frac{1}{\sqrt{2}}$ -24x the Control value). Because V_p is itself a function of the exchange coefficients, varying the latter will also modulate the dominant non-dimensional parameter, $\frac{V_p}{fl_h}$, based on our earlier result. Thus, in order to isolate the effect of varying C_k or C_d alone, we simultaneously modulate l_h so as to fix $\frac{V_p}{fl_h}$ to its Control value. The values for V_p and l_h are listed in Table 3.4.

Note that in our idealized thermodynamic environment the potential intensity is much more sensitive to C_d than C_k . Indeed, Eq. (3.11) predicts that V_p should be independent of C_k , though the detailed calculation still indicates an increase in V_p with C_k , which is amplified by the pressure dependence on the saturation vapor pressure.

The dimensional equilibrium radial profiles for the simulation sets varying C_k and C_d are displayed in Figure 3-23. For increasing C_k (i.e. slowly increasing V_p), the equilibrium storm structure remains nearly fixed in space but exhibits a gradual re-

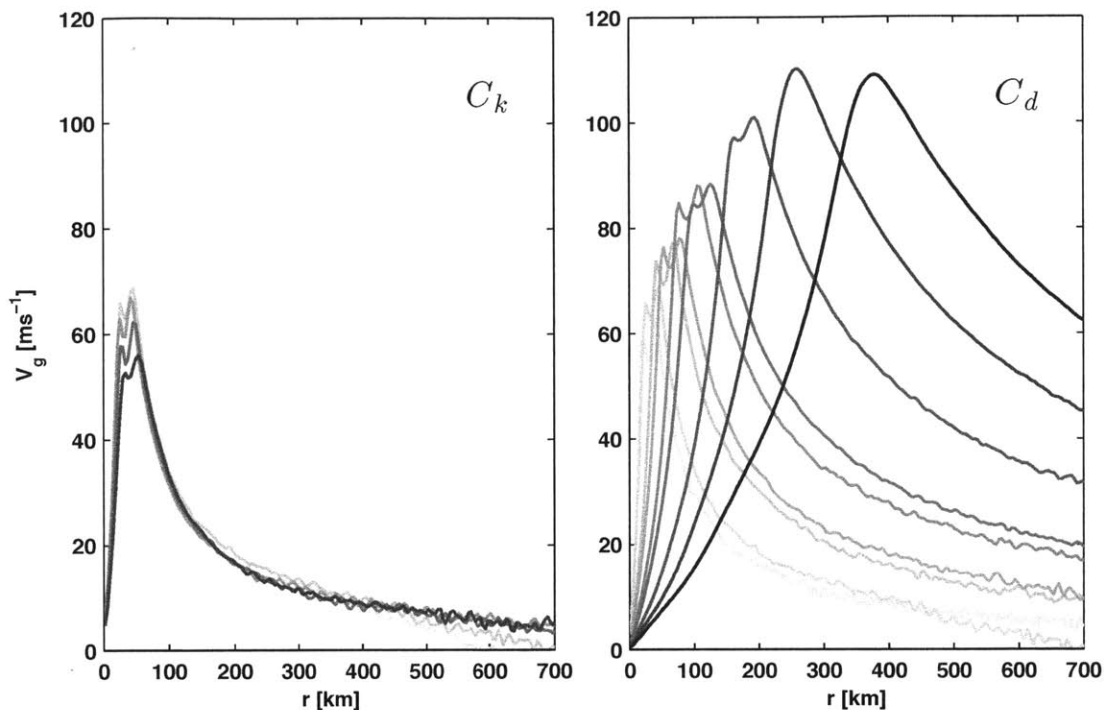


Figure 3-23: Equilibrium radial profiles of the gradient wind for simulation sets varying C_k (left) and C_d (right), where $\frac{V_p}{f l_h}$ has been held constant across all simulations. Shading reflects potential intensity from low (light grey) to high (black).

duction in the peak wind speeds within the eyewall. Meanwhile, for decreasing C_d (i.e. rapidly increasing V_p), the storm intensifies and expands significantly. Notably, for a given value of $\frac{C_k}{C_d}$, the dimensional storm structure is markedly different depending on whether one varies this ratio via C_k or C_d .

3.4.1 Inner Core

Following our prior procedure, we normalize V by V_m and r by r_{ew} , with the result displayed in Figure 3-24. Once again, this normalization removes much of the variability in both cases and divides residual variability between the inner and outer regions. For C_k , there is minimal additional variability. For C_d , there are two additional degrees of variability: a contraction of the far outer wind field and an expansion of the eye with increasing V_p (i.e. decreasing C_d). Explanations for these additional modes of

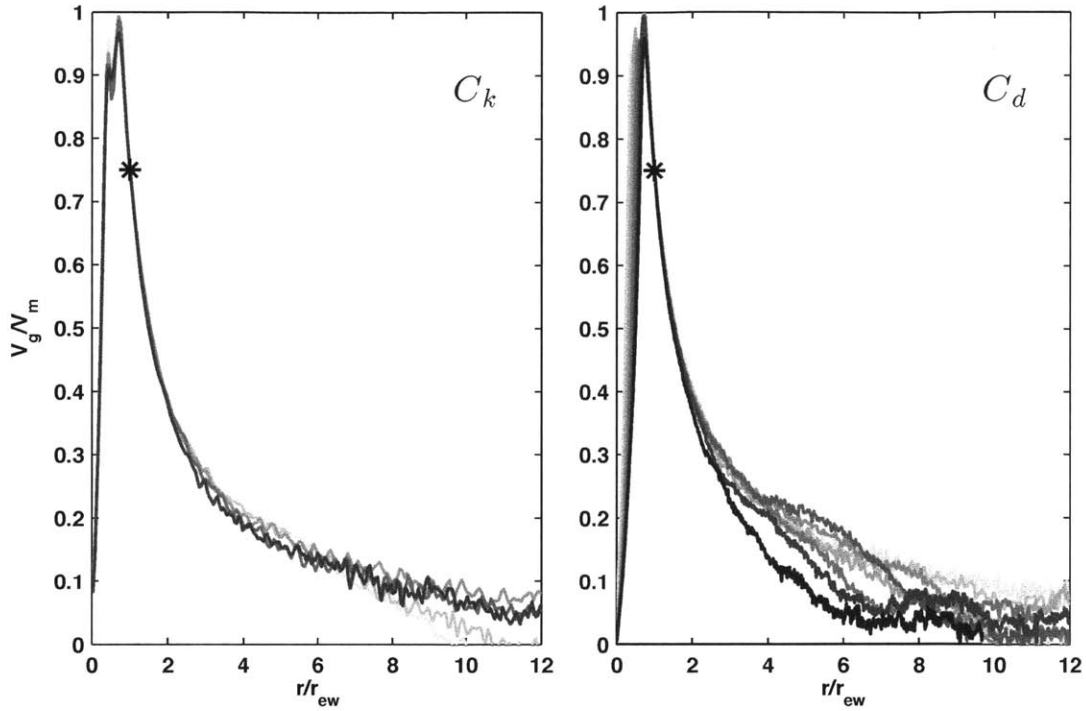


Figure 3-24: As in Figure 3-23, but with radial profiles normalized as follows: V by V_m and r by r_{ew} .

variability are explored further below.

In the case of V_m , a theoretical relationship exists that we may test using our simulation results. For a reasonably intense vortex, i.e. $V_m \gg fr_m$, Emanuel and Rotunno (2011) derive an equation (Eq. (41)) for the non-dimensional maximum gradient wind speed that is a function solely of the ratio of the exchange coefficients, given by

$$\frac{V_m}{V_p} \sim \left(\frac{1}{2} \frac{C_k}{C_d} \right)^{\frac{\frac{1}{2} C_k}{2 - \frac{C_k}{C_d}}} \quad (3.25)$$

The simulated equilibrium values of V_m are compared to the scaling of Eq. (3.25) in Figure 3-25. The data closely match the theory over the entire range of values when varying both C_k and C_d , and the respective best-fit scaling constants are identical and near unity (1.02). Indeed, the non-dimensional equilibrium intensity appears to closely follow the theoretical relation of Emanuel and Rotunno (2011) and depends

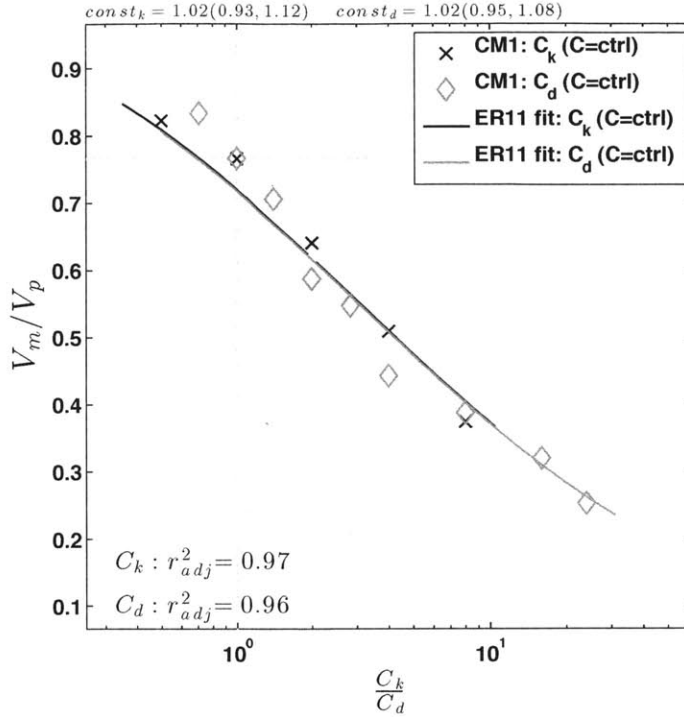


Figure 3-25: Scaling between $\frac{V_m}{V_p}$ and $\frac{C_k}{C_d}$ in simulations (marker) and the theoretical scaling relation given by Eq. (3.25) (line) from Emanuel and Rotunno (2011) for varying C_k (black, x) and C_d (grey, diamond). The horizontal mixing length, l_h , is varied such that the non-dimensional parameter $\frac{V_p}{fl_h}$ remains fixed at its Control value. For each exchange coefficient, best-fit scaling constants and 95% confidence intervals are listed at the top and adjusted r-square values are listed in the lower-left corner.

only on the ratio of the exchange coefficients, which is remarkable given that the dimensional storms differ so greatly depending on whether this ratio is varied by C_k or C_d . Additionally, note that the experiments with very small C_d correspond to extremely large values of V_p (450 ms^{-1} ; Table 3.4), which may lead one to question whether such a storm can be properly resolved in the given modeling environment. However, the combination of the rapid decline of $\frac{V_m}{V_p}$ at large values of $\frac{C_k}{C_d}$ (V_m actually decreases as C_d is reduced from $\frac{1}{16}$ to $\frac{1}{24}$ of its Control value despite the corresponding large increase in V_p) and the rapid expansion of the storm both serve to maintain a well-resolved dimensional storm.

As for r_{ew} , Figure 3-26 displays the scaling relationships between the ratio of exchange coefficients and r_{ew} when varying C_k and C_d . These scalings do not collapse

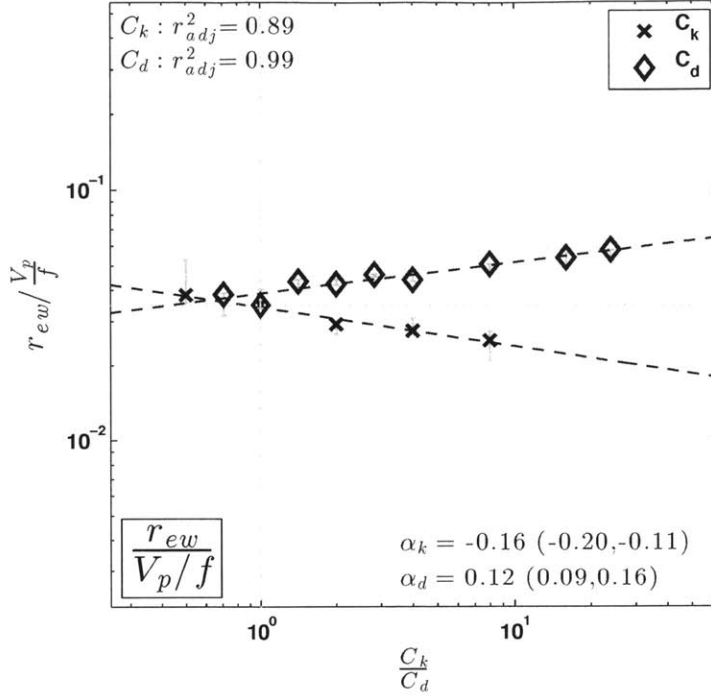


Figure 3-26: Scaling of r_{ew} with the ratio of exchange coefficients, $\frac{C_k}{C_d}$, for varying C_k (black, x) and C_d (grey, diamond). Best fit scaling exponents with 95% confidence intervals are listed in the lower-right corner, and adjusted r-square values are given in the top-left corner.

to a single scaling with $\frac{C_k}{C_d}$, though in each case the scaling is relatively weak and is given by

$$\frac{r_{ew}}{\frac{V_p}{f}} \sim C_k^{-0.15} C_d^{-0.1} \quad (3.26)$$

Thus, the inner core of the non-dimensional storm contracts slowly with both increasing C_k and C_d .

Given that for the case of varying C_k , the inner core appears to scale uniformly, whereas for C_d this is not the case, an alternative possible interpretation is the following approximate scaling

$$\tilde{r}_{ew} \sim C_d^{-0.25} \left(\frac{C_k}{C_d} \right)^{-0.15} \quad (3.27)$$

This perspective would suggest that the inner core storm size does in fact scale with

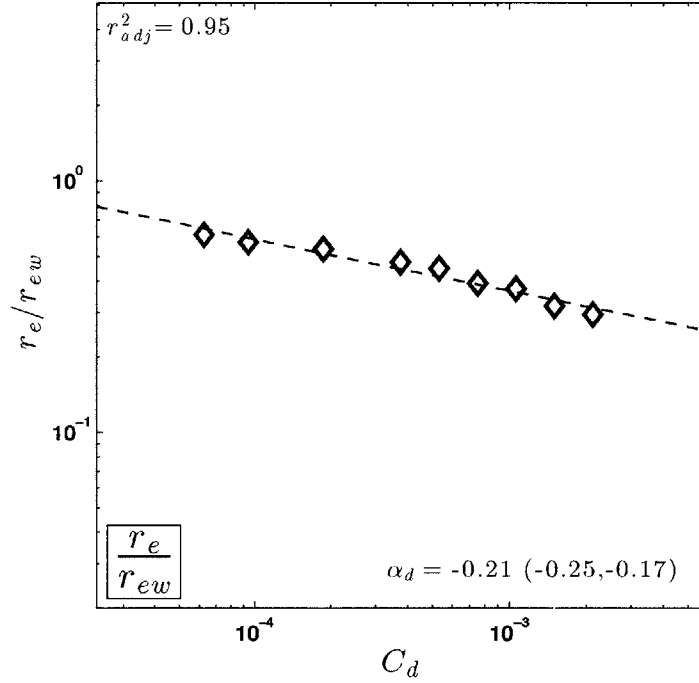


Figure 3-27: Scaling of the ratio of r_e to r_{ew} with C_d . Best fit scaling exponents with 95% confidence intervals are listed in the lower-right corner, and adjusted r-square values are given in the top-left corner.

$\frac{C_k}{C_d}$, but superimposed upon this scaling is an additional modification associated with C_d alone. This seems plausible given the variability observed within the eye (Figure 3-24), characterized by an expansion of the eye relative to the eyewall for decreasing C_d . Such behavior is consistent with a negative scaling exponent. To quantify this relationship, Figure 3-27 displays the scaling of the ratio $\frac{r_e}{r_{ew}}$ as a function of C_d . The resulting scaling is $\frac{r_e}{r_{ew}} \sim C_d^{-0.21}$, though because this is a scaling relative to r_{ew} , it cannot explain the additional scaling with C_d in Eq. (3.27). A theoretical argument for this relative scaling is explored in Section 3.5.

3.4.2 Outer radius

Finally, we explore sensitivity of the outer wind field to variations in the exchange coefficients following our earlier procedure. Figure 3-24 indicates that for varying C_k , there is little residual variability in the outer wind field, with the possible exception

Table 3.5: As in Table 3.3, but for C_k and C_d , with $C_1 = \frac{V_p}{f l_h}$ held fixed at its Control value.

| $C_k (\times 10^{-3})$ | c | $C_d (\times 10^{-3})$ | c |
|------------------------|-----|------------------------|------|
| .75 | .28 | 2.12 | .27 |
| 1.5 | .26 | 1.5 | .26 |
| 3 | .31 | 1.06 | .44 |
| 6 | .26 | .75 | .45 |
| 12 | .24 | .53 | .92 |
| — | — | .375 | .73 |
| — | — | .188 | 2.52 |
| — | — | .094 | 2.28 |

of very near r_0 where wind speeds are close to zero. Meanwhile, for varying C_d , there is significant additional variability in the outer wind field that, though quite noisy, suggests a systematic contraction as C_d is decreased. Given that $V_p \sim C_d^{-\frac{1}{2}}$, the quantity $C_d V_p$ varies directly with C_d . Thus, the role of C_2 in Eq. (3.18) predicts that the far outer wind field will indeed contract as C_d is decreased, as is observed.

The fit of Eq. (3.18), empirically modified with $c = .3$, to the equilibrium outer wind profiles is shown in Figure 3-28, which is analogous to Figure 3-9. Eq. (3.18) provides a good fit for all values of C_k , corroborated by the constancy of the optimized c as C_k is varied (Figure 3-10 and Table 3.5). However, Eq. (3.18) is too sensitive to changes in C_d relative to the numerical model output, resulting in large errors at all radii as C_d is progressively decreased toward an extreme value of $\frac{1}{24}$ of Control. Unfortunately, the optimized value of c does not vary smoothly with C_d , rendering a quantitative estimate of the degree of oversensitivity difficult. We emphasize, though, that in this case we are exploring values of C_d that are far removed from those typically associated with an Earth-like atmospheric boundary layer beneath a tropical cyclone.

Though estimation of the true r_0 may thus be difficult for C_d , the outer radius with the influence of C_2 removed, r_0^* , still provides a sensible metric for the overall size of the storm that is independent of the outer wind field variability. Thus, Figure 3-29 displays the scaling of r_0^* with $\frac{C_k}{C_d}$ for varying C_k and C_d , where r_0^* is calculated

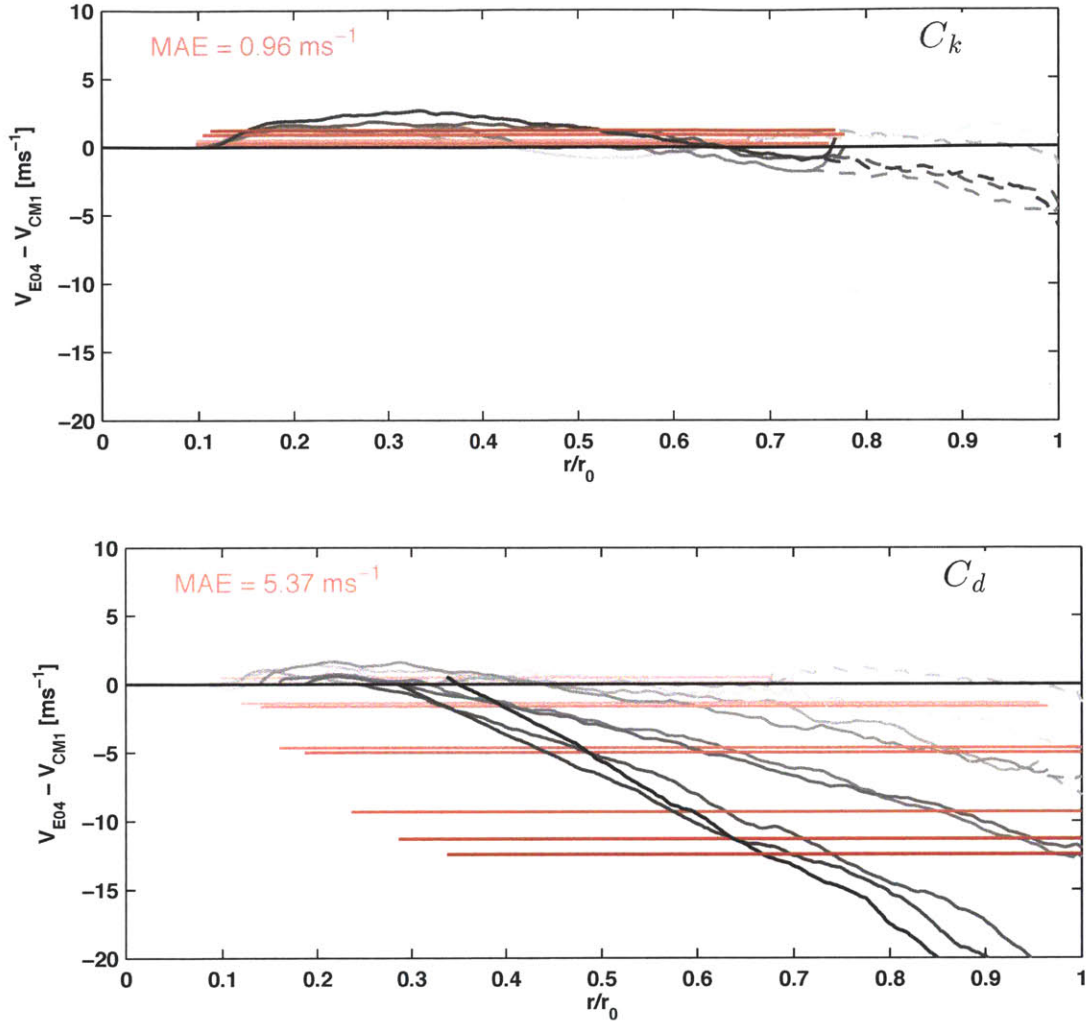


Figure 3-28: As in Figure 3-11, but for simulations varying C_k and C_d while holding $\frac{V_p}{f l_h}$ fixed to its Control value. Radial profiles of error in the fit of the analytical outer wind model (Eq. (3.18), empirically modified with $c = .3$) to the equilibrium radial wind profile, defined as $V_{E04} - V_{CM1}$, for all simulations varying each of the six relevant dimensional parameters. Error profiles are smoothed with a 10-pt smoother. In the top four panels, shading reflects potential intensity from low (light grey) to high (black); in the bottom two panels, shading reflects parameter magnitude from low (light grey) to high (black). Analytical model is fit to $r(.75V_m)$, with the range $r(.75V_m < V < .1V_m)$ solid and $r(V < .1V_m)$ dashed; radii are normalized by r_0 calculated using the outer wind model. Red line depicts mean error over the inner range, and the corresponding mean absolute error (MAE) for the simulation set is listed in the top left corner.

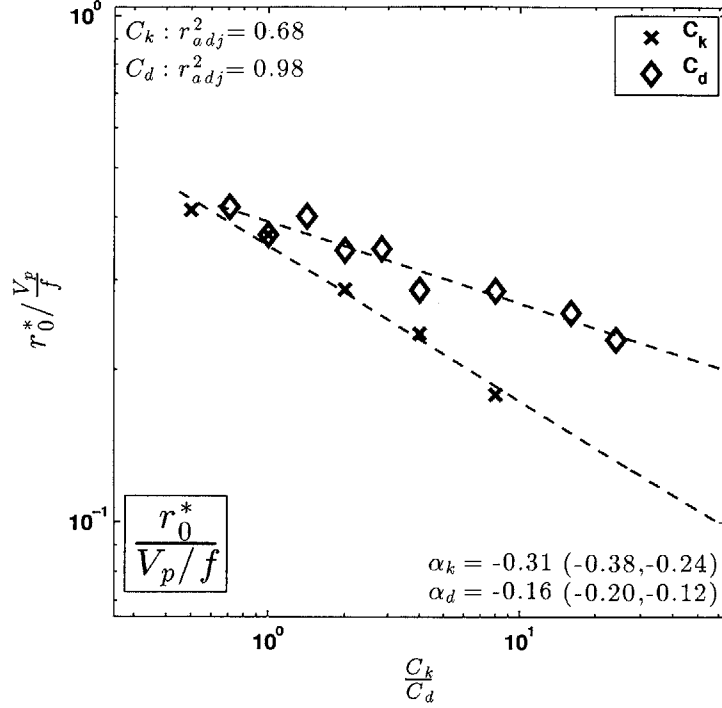


Figure 3-29: As in Figure 3-26 but for r_0^* .

with Eq. (3.18), fit at r_{ew} as it was above. The resulting scaling is

$$\frac{r_0^*}{\frac{V_p}{f}} \sim C_k^{-.3} C_d^{-.15} \quad (3.28)$$

Thus, overall non-dimensional storm size contracts slowly with increasing C_d and more rapidly with increasing C_k .

3.4.3 Comparison with structural theory

Emanuel and Rotunno (2011) also derive a structural relationship between r_m and r_0 (Eq. (42)), which can be rewritten in non-dimensional form as

$$\frac{\widetilde{r}_m}{\widetilde{r}_0^2} = \left(\frac{1}{2}\right)^{\frac{3}{2}} \left(\frac{C_k}{C_d}\right)^{\frac{1}{2}} \quad (3.29)$$

where tildes denote non-dimensionalization by $\frac{V_p}{f}$ and we use our r_0^* to represent their

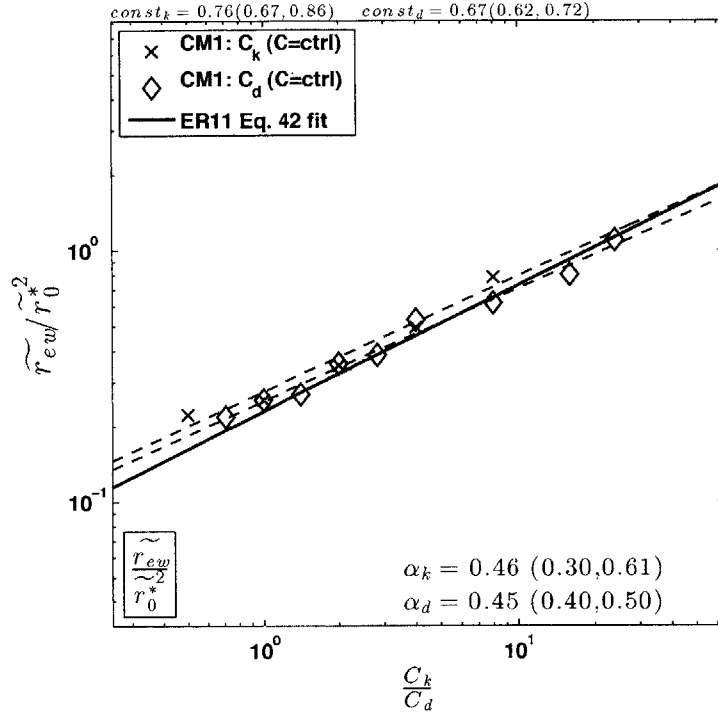


Figure 3-30: Scaling of $\frac{\tilde{r}_{ew}}{r_0^*}$ with $\frac{C_k}{C_d}$ in simulations (marker) with linear fit (dashed) and the theoretical scaling relation given by Eq. (3.29) (solid) from Emanuel and Rotunno (2011) for varying C_k (black, x) and C_d (grey, diamond). The horizontal mixing length, l_h , is varied such that the non-dimensional parameter $\frac{V_p}{fl_h}$ remains fixed at its Control value. For each exchange coefficient, best-fit scaling constants and 95% confidence intervals are listed at the top.

theoretical r_0 . Taking the scaling results from Eqs. (3.27) and (3.28) together, Figure 3-30 shows that the scaling of this non-dimensional ratio with $\frac{C_k}{C_d}$ is indeed nearly a square-root dependence on $\frac{C_k}{C_d}$ when varying either C_k or C_d , despite the fact that the scalings for the respective radii differ between the two cases. The best-fit constant in each case is in the range .65 – .75.

This result is somewhat surprising given that the theory of Emanuel and Rotunno (2011) is valid only in the ascending region of the storm, and thus it's not clear that such a structural relationship for the outer region of the storm would apply. The scalings are nearly identical when fitting Eq. (3.18) to $r(.3V_m)$, suggesting that they are relatively robust even though the fit of Eq. (3.18) to the true outer wind field is far from perfect. However, in the context of the earlier result that the theoretical length

scale of $\frac{V_p}{f}$ also emerges from r_0^* this result provides additional evidence that extant tropical cyclone theory accurately captures the radial structure of the tropical cyclone, and any additional variability in the outer wind field associated with variations in w_{cool} , C_d , etc., is simply passively superimposed onto this underlying framework.

3.5 Theoretical scaling for eye

Our results indicate that the radial wind profile in the eye is found to be predominantly sensitive to u_{sfc} , C_d and l_h (the last modulates the entire eyewall). Specifically, the eye expands for decreasing u_{sfc} and C_d and for increasing l_h . These sensitivities can be interpreted via analysis of the integrated angular momentum balance of the eye. The eye at equilibrium within the boundary layer should be characterized by a balance between inward radial turbulent transport of angular momentum from the eyewall and the integrated angular momentum loss at surface (Emanuel, 1997; Smith, 1980).

The local tendency of scalar quantities due to turbulence is parameterized as

$$D_M = \frac{1}{r} \frac{\partial}{\partial r} \left(r K_h \frac{\partial M}{\partial r} \right) \quad (3.30)$$

where the radial turbulent diffusivity, K_h , is

$$K_h = l_h^2 S_h = l_h^2 \sqrt{2 \left(\frac{\partial u}{\partial r} \right)^2 + \left(\frac{\partial V}{\partial r} - \frac{V}{r} \right) \left(\frac{\partial V}{\partial r} \right)} \quad (3.31)$$

and S_h is the horizontal component of the local deformation. Integrating from the center out to some radius R gives the net inward turbulent flux of angular momentum across R . This flux must equal the integrated angular momentum loss due to friction at the surface,

$$\frac{C_d}{h_{BL}} \int_0^R (V + u_{sfc})(rV)rdr \approx \left[l_h^2 r V \sqrt{2 \left(\frac{\partial u}{\partial r} \right)^2 + \left(\frac{\partial V}{\partial r} - \frac{V}{r} \right) \left(\frac{\partial V}{\partial r} \right)} \right]_R \quad (3.32)$$

given zero flux across $r = 0$ and assuming that the net vertical flux of angular momentum out the top of the boundary layer is negligible; h_{BL} is the depth of the well-mixed boundary layer and we have taken $M \approx rV$. Neglecting the term on the right hand side of Eq. (3.32) involving the radial shear of the radial wind, the resulting balance is given by

$$\frac{C_d}{h_{BL}} \int_0^R (V + u_{sfc})(rV)rdr \approx \left[l_h^2 r V \sqrt{\frac{\partial V}{\partial r} \left(\frac{\partial V}{\partial r} - \frac{V}{r} \right)} \right]_R \quad (3.33)$$

The RHS is evaluated at some $r = R$ just inside r_m , whereas the LHS must be integrated.

Though $V(r)$ in the eye is typically assumed to be close to a state of solid body rotation (Emanuel, 1997), it cannot be exactly so or else the turbulent angular momentum flux (RHS) vanishes. As a simple ansatz, we apply a power-law solution for $V(r)$ of the form

$$\frac{V}{V_m} = \left(\frac{r}{r_m} \right)^\alpha \quad (3.34)$$

in Eq. (3.33), which leads to the scaling

$$r_m^3 \sim \frac{h_{BL} l_h^2}{C_d \left(1 + \frac{2\alpha+3}{\alpha+3} \frac{u_{sfc}}{V_m} \right)} \quad (3.35)$$

where we have taken $R = r_m$, ignoring the details of the eyewall structure.

Thus, this scaling predicts $r_m \sim l_h^{\frac{2}{3}}$ and $r_m \sim C_d^{-\frac{1}{3}}$. For l_h , the scaling is a reasonable estimate of the empirically-derived exponent of $-.55$ though slightly exceeds it. For C_d , the scaling also gives a decent estimate, whose exponent was found above to be $-.2$. The scaling with u_{sfc} , however, is qualitatively consistent with the observed relationship but is quantitatively incorrect. The scaling predicts significant sensitivity only for $\frac{u_{sfc}}{V_m} \sim 1$, which corresponds only to the cases with high values of u_{sfc} (for $u_{sfc} = 10$, this quantity is approximately $.2$), yet we see systematic sensitivity at all values of u_{sfc} , suggesting that the power-law solution is not appropriate to capture the effect of u_{sfc} on eye structure. This is true even for large α , a consequence of the

fact that the surface sink of angular momentum is area-weighted and the region where $\frac{u_{sfc}}{V_m} \sim 1$ lies near $r = 0$ and thus occupies a relatively small area within the eye. Note that the scalings for l_h and C_d are independent of the specific profile of $V(r)$ and can be extracted via scale analysis of Eq. (3.33). This model also does not represent the effects of Q_{cool} , which was observed to expand the eye at high values. Overall, though, this model based on angular momentum balance appears to conceptually capture a few of the key processes that contribute to modulation of the eye diameter.

3.6 Discussion

Though our scaling results are physically intuitive, the representation of the full spectrum of turbulent eddies via a single radial mixing length scale, l_h , as is required in axisymmetric geometry, is less than ideal. We have demonstrated that the more relevant external parameter is this radial mixing length normalized by the radial storm scale, yet there exists no accepted theory for the “correct” value of this parameter nor is it understood that this parameter is necessarily a constant in both time and space. In principle, given that no eddies are resolved in axisymmetry, l_h represents the length scale of the largest eddy, which plausibly corresponds to the circumference of the eyewall and therefore should scale with the radius of maximum wind. Notably, application of such an ansatz to our scalings results in $V_m \sim V_p$ and $r_m \sim r_0 \sim \frac{V_p}{f}$ as would be expected from dimensional considerations alone. However, lacking additional information, the combination of this structural uncertainty and the vagaries of modeling storm size render a transition from quantifying scaling estimates to more precise predictions of V_m and r_m potentially dubious using axisymmetric models in their current form.

Nonetheless, to the extent that the qualitative dynamics of the effect of eddies on storm structure are reasonably captured in this framework, as appears to be the case based on theoretical considerations as well as recent work that finds favorable comparisons between axisymmetric and three-dimensional simulation output (Bryan, 2011), much may yet be gleaned from the analysis of computationally-cheaper axisymmetric

simulations and comparisons with theory. In particular, it is perhaps unsurprising in retrospect that the relative rather than absolute eddy length scale is the relevant parameter in the context of extant tropical cyclone theory that is itself phrased entirely in terms of relative rather than absolute radial length scales, a topic discussed in Emanuel (1995b). Indeed, it seems plausible that a similar argument would hold for the parameterized vertical turbulence, i.e. the relevant parameter is the vertical turbulent mixing length relative to the depth of the troposphere, though sensitivity of storm structure to this parameter is in any case small for commonly-accepted values relevant for the modern Earth atmosphere.

Furthermore, details of the dynamics of the eye may play a role in modulating r_m , at least in the context of the simplified axisymmetric set-up explored here. While radial turbulence is clearly the dominant factor, whose effect is to shift the entire eyewall outwards, variations in the drag coefficient, radiative cooling rate, and gustiness all appear to add secondary variability to eye size. The extent to which such processes are important in a three-dimensional tropical cyclone containing the full spectrum of eddies is unclear. Emanuel (1997), following from Smith (1980), argues that the role of turbulent eddies is simply a passive response to an otherwise barotropically-unstable radial wind profile inside of the radius of maximum winds. The eddies rapidly transport angular momentum inwards from the radius of maximum winds (which is replenished by the secondary circulation), thereby driving the eye towards a state of solid-body rotation. Given this perspective, it seems likely that real three-dimensional eddies, which act on fast time scales and are capable of responding to changes in the local forcing (analogous to a time-varying l_h), may counteract these secondary effects in real-world tropical cyclones. Results from Khairoutdinov and Emanuel (2012) exploring RCE on an f -plane in three dimensions found preliminary evidence that, in addition to overall size, r_m increased with increasing T_{sst} .

The extent to which these equilibrium results can be applied to real storms in nature is not clear for two key reasons. First, the time-scales to equilibrium identified here for the Control simulation are significantly longer than the lifespan of tropical cyclones on Earth. Second, storms in nature rarely exist in a truly quasi-steady back-

ground for more than a couple of days, if at all. Instead, storms live within an evolving thermodynamic environment due to along-track changes in potential intensity, vertical wind shear, interactions with land or extratropical disturbances, etc. Even given an idealized atmospheric state in a truly quiescent large-scale environment, the thermal stratification of a real ocean allows for time-dependent cooling of the sea surface driven by wind-driven turbulent mixing of the upper ocean, thus precluding equilibration of the background environment when a storm is present. Indeed, the large range in observed size distribution cannot be explained by the equilibrium results; Chavas and Emanuel (2010) noted that non-dimensionalization by $\frac{V_p}{f}$ had little impact on their results, and correlations between storm size and this length scale or with V_p or f alone were relatively small. However, equilibrium dynamics may potentially manifest itself more clearly at an aggregate level, such that shifts in the global distribution of $\frac{V_p}{f}$ within the main tropical cyclone basins may translate into shifts in the size distribution of tropical cyclones, even though variability within the global distribution is the result of more complex non-equilibrium processes. For example, global warming due to a doubling of atmospheric carbon dioxide concentrations is expected to lead to a global increase in potential intensity of $\sim 10\%$ (Emanuel, 1987; Knutson et al., 2010). Much more work is needed to assess the extent to which such a relationship is borne out in models while accounting for shifts in the spatial distribution of potential intensity as well as tropical cyclone genesis locations and tracks.

More broadly, the emergence of many details of the equilibrium storm structure in these idealized simulations is interesting given the simplistic set-up and the ongoing variability that characterize the time-evolution of many of the simulations even during the post-equilibration period. Though there are additional details of storm structure that are surely lost under these idealized conditions, and a more properly resolved boundary layer may be necessary to better quantify the effects of varying those parameters that significantly modulate the lower troposphere, particularly the sea surface temperature, this work furthers the notion that many of the fundamental dynamical processes of the tropical cyclone are in fact quite coarse-grained and can be reasonably captured by simple models that enable inflow near a lower boundary, ex-

change of enthalpy and momentum with that lower boundary, and outflow aloft where enthalpy can be expelled (i.e. a Carnot engine). This harps back to the analyses using very simple three-layer tropical cyclone models by Ooyama (1969) and DeMaria and Pickle (1988), the latter found interesting variations in storm size, which compare favorably to both observations and more recent modeling work, even at a very low horizontal resolution of 25 km .

3.7 Conclusions

This work combines highly idealized modeling, motivated by existing axisymmetric tropical cyclone theory, with dimensional analysis to systematically quantify the scaling relationship between the structure of a model tropical cyclone at statistical equilibrium and relevant model, initial, and environmental input parameters. We perform this analysis in a model world whose complexity is reduced so as to retain only the essential physics of the tropical atmosphere necessary to produce a tropical cyclone: radiative-convective equilibrium in axisymmetric geometry on an f -plane with constant tropospheric cooling, constant background gustiness (to provide a background source of water vapor), constant surface exchange coefficients for momentum and enthalpy, and constant sea surface and tropopause temperatures. Importantly, this model tropical atmosphere could in principle exist for all time in column-wise radiative-convective equilibrium, in which column-integrated radiative cooling is exactly balanced by surface fluxes of enthalpy, in the absence of a tropical cyclone. Following the theoretical work of Emanuel and Rotunno (2011), we characterize the full structural evolution of the storm by the time-series of three dynamical variables calculated near the top of the boundary layer: the maximum gradient wind speed, a proxy for the radius of maximum gradient wind, taken as the radius of 75% of the maximum wind speed, and the outer radius of vanishing wind.

We find that, under these simplified conditions, the inner core storm structure at statistical equilibrium is primarily a function of only three external parameters: the potential intensity, the Coriolis parameter, and the radial turbulent mixing length.

These three parameters comprise the dominant non-dimensional parameter, $\frac{V_p}{fl_h}$, for the equilibrium system. This parameter can be interpreted as the ratio of the storm radial length scale, $\frac{V_p}{f}$, to the radial eddy mixing scale, l_h , and it dictates that the critical role of parameterized radial turbulence in determining inner-core storm structure in axisymmetric geometry is manifest not in the absolute value of the radial turbulent mixing length but rather in its value relative to the natural length scale of the storm. A second non-dimensional parameter, $\frac{C_d V_p}{w_{cool}}$, whose reciprocal represents the non-dimensional Ekman suction rate, exists within a pre-existing slab boundary layer outer wind model that, given a simple empirical modification, can reproduce the outer wind field of a tropical cyclone across a range of simulations. Controlling for this secondary mode of variability, we find that the overall size of the storm scales nearly linearly with $\frac{V_p}{f}$, which is the theoretical scaling for the upper bound on tropical cyclone size derived in Emanuel (1986) that is a consequence of the energetic contribution of outflow work in the Carnot framework. Contrary to conventional wisdom based on geostrophic adjustment, the Rossby deformation radius is shown not to be fundamental to equilibrium size. Finally, the ratio of the surface exchange coefficients, $\frac{C_k}{C_d}$, represents a third relevant non-dimensional parameter whose effect on non-dimensional storm structure appears to match the theoretical relationships for intensity and structure given in Emanuel and Rotunno (2011).

Opportunities for future work abound. First, further analysis of tropical cyclones within our idealized environment is warranted, including a better understanding of the deviations from the uniform scaling with potential intensity across our thermodynamic parameters, particularly within the eye. An exploration of storm size at the extremes, such as the existence of a theoretical lower bound, would be fruitful. New simulations run at higher resolution would be useful to test the sensitivity of the details of the results found herein to more realistic representations of real world storms. In particular, exploration of the analytical outer wind field boundary layer model and its application to the non-convecting outer region of a tropical cyclone is needed to understand both the physics of our empirical modification as well as the validity of the analytical model when applied to a simulation with a more properly resolved bound-

ary layer. Second, this work may be extended to environments of greater complexity. For example, application of an explicit temperature-dependent radiative scheme or full-physics radiation scheme could be useful in assessing the impact of radiative feedbacks on our results, which may be non-negligible given the apparent sensitivity of eye dynamics, and thus the radius of maximum wind, to the radiative cooling rate. The impact of factors that limit storm intensity, such as mid-level ventilation (Tang and Emanuel, 2010) and ocean mixing, on storm size and structure remains unexplored. Additionally, testing the validity of the results in more computationally-expensive three-dimensional simulations where three-dimensional turbulence is more properly resolved would provide insight into the role “real” turbulence plays in setting storm structure, as well as the extent to which axisymmetric parameterizations of turbulence accurately reproduce the effects of three-dimensional turbulence on storm size. Finally, application and extension of this work to real world tropical cyclones remains an open question, including the more complicated time-dependent dynamics associated with the transient phase of storm evolution in our idealized modeling environment. Ultimately, this may help provide a physical interpretation of the observed size distribution of tropical cyclones (Chavas and Emanuel, 2010). Such a fundamental physical understanding would ideally translate into a capacity for credible prediction of storm size, structure, and evolution at the level of individual storms, as well as insight into how the distribution of storm size may differ in other climate states. Both would be beneficial for the purposes of emergency preparedness and risk management alike.

Chapter 4

Exploration of Equilibrium

Tropical Cyclone Size in Three Dimensional Simulations

4.1 Introduction

Tropical cyclone size remains an unsolved problem in tropical meteorology. Though significant advances have been made in understanding storm intensity (Emanuel, 1986; Bister and Emanuel, 1998; Emanuel and Rotunno, 2011) and its modification by interaction with the environment in which it is embedded, such as vertical wind shear (Tang and Emanuel, 2010; Zeng et al., 2007), the radial scale and structure of the storm is less well-understood. Recent theoretical work (Emanuel and Rotunno, 2011) derived a solution for the steady-state radial structure of the convecting inner core of the storm in an axisymmetric framework that assumes gradient thermal wind balance and moist slantwise neutrality. Additionally, Emanuel (2004) developed a complete radial profile as a patchwork of asymptotically-matched solutions for the eye, the convecting inner core, and the non-convecting outer circulation. In both cases, though, the solutions are defined relative to a free parameter given by the outer radius of vanishing wind, r_0 , thus providing no constraint on the radial length

scale of the storm as a whole.

Currently, no theoretical framework exists for determining r_0 , though potential intensity theory (Emanuel, 1986) provides a theoretical upper bound for this quantity that scales with a length scale given by the ratio of the potential intensity, V_p , to the Coriolis parameter, f . In Chapter 3, tropical cyclone size at a statistical steady-state across a wide range of idealized climate states was explored in an axisymmetric modeling framework. Storm size, measured by an estimate of r_0 adjusted to remove a secondary mode of variability in the non-convecting outer region of the wind field, was found to scale predominantly with this theoretical length scale, $\frac{V_p}{f}$.

Additionally, the inner core structure of the storm was found to be modulated primarily by a non-dimensional parameter given by the ratio of this storm length scale to the parameterized eddy radial mixing length, l_h . This result provides a conceptually simple and qualitatively reasonable characterization of the fundamental role of radial turbulence in modulating eye and eyewall structure. Theoretically, Emanuel (1997) demonstrated the requirement of radial turbulence for preventing eyewall collapse due to the frontogenetic nature of the storm's overturning circulation. Observationally, the inner core wind field exhibits significantly greater variability than the broader outer circulation during the lifetime of a storm (Frank, 1977; Weatherford and Gray, 1988; Merrill, 1984). Indeed, overall size, often defined as r_0 (Chavas and Emanuel, 2010), the radius of 34-kt winds, the radius of outermost closed isobar, etc., is only weakly correlated with maximum wind speed or the radius of maximum winds. In contrast to the relative quiescence of the minimally-convecting outer region of the storm, the convective inner core is subject to the asymmetric, chaotic, multi-scale variability associated with a multitude of processes, such as vortex Rossby waves excited by both internal (Schubert et al., 1999) and external factors (Reasor et al., 2000; Corbosiero et al., 2006; Reasor et al., 2004; Wang, 2002) and entropy ventilation (Tang and Emanuel, 2012; Molinari et al., 2012).

Despite the conceptual appeal of this simple axisymmetric framework, though, the crude axisymmetric representation of a critical and highly azimuthally-asymmetric process muddies direct application of the axisymmetric results to real world storms

that live in three-dimensions. Thus, this work seeks to climb the next rung on the hierarchy of models (Held, 2005) from analytical theory to real world tropical cyclones by evaluating the primary results obtained in the axisymmetric framework within a fully three-dimensional model environment in which eddies with scales larger than the grid scale can be explicitly resolved. Specifically, we will focus on the sensitivity of TC size to variations in potential intensity as modulated by the tropopause temperature, which was identified in Chapter 3 as a useful “base” case from among the four governing thermodynamic parameters given that its dominant effect is simply to modulate the convective outflow temperature.

Section 4.2 describes the methodology, including a brief description of the model set-up and the key similarities and differences with respect to the axisymmetric simulations. Section 4.3 motivates the role of the Coriolis parameter with a simple example of self-aggregation. Section 4.4 presents the key results. Section 4.5 discusses implications of the results and the limitations of this study. Finally, Section 4.6 synthesizes key conclusions and explores avenues for future work.

4.2 Methodology

4.2.1 CM1 model: 3D

This work employs version 15 of the Bryan Cloud Model (CM1), a non-hydrostatic atmospheric cloud-system resolving model (CSRМ; original version described in Bryan and Fritsch (2002)). CM1 solves the fully compressible equations of motion in height coordinates on an f-plane for flow velocities (u, v, w) , non-dimensional pressure (π) , potential temperature (θ) , and the mixing ratios of water in vapor, liquid, and solid states (q_x) on a fully staggered Arakawa C-type grid in height coordinates. Additional details can be found in Chapter 3.

Conveniently, the model can be configured using identical physics in both two-dimensional axisymmetric (radius-height) and fully three-dimensional geometry, with the important exception of the representation of turbulence. Because turbulence is

inherently a three-dimensional phenomenon, two-dimensional (axisymmetric) geometry cannot resolve turbulent eddies of any scale, and thus the effect of turbulent eddies is necessarily parameterized using a modified Smagorinsky-type scheme, in which the grid length scale is replaced with distinct horizontal and vertical mixing lengths, l_h and l_v , respectively. The distinct mixing lengths are employed in order to represent the differing nature of turbulence between the radial and vertical directions in a highly anisotropic system such as in the inner core of a tropical cyclone. As demonstrated in Chapter 3, the horizontal mixing length has a pronounced effect on the inner-core structure of the equilibrium storm. Meanwhile, in three-dimensions, a proper Smagorinsky turbulence scheme is employed to represent the subgrid-scale effects of turbulence, while eddies whose scales exceed the grid-scale are explicitly resolved. There remain parameterized mixing length scales, but they are much smaller and are intended to represent only unresolved subgrid-scale turbulence rather than storm-scale eddies.

In this work, a set of three-dimensional simulations is performed under the identical idealized model and environmental set-up as was employed for the axisymmetric simulations analyzed in Chapter 3. Here we briefly review this set-up. Surface pressure is set to 1015 hPa . Radiation is represented by a constant cooling rate, Q_{cool} , applied to the potential temperature everywhere in the domain where the absolute temperature exceeds a threshold value, T_{tpp} ; below this value, Newtonian relaxation back to this threshold is applied with a timescale of 40 days. At the lower boundary, the sea surface temperature is taken as a constant, T_{sst} , and surface fluxes of enthalpy and momentum are calculated using standard bulk aerodynamic formulae in which the exchange coefficients for momentum, C_d , and enthalpy, C_k , are held constant. Finally, background surface enthalpy fluxes are required to balance column radiative cooling in order to achieve radiative-convective equilibrium in the absence of significant resolved wind perturbations, such as a tropical cyclone. Though in three-dimensions this effect can be included via imposition of a mean background flow, for the sake of consistency and comparison with the axisymmetric simulation results we simply add a constant gustiness, u_{sfc} , to the magnitude of the wind speed, $|\mathbf{u}|$, for

the model calculation of the surface fluxes.

For this environmental set-up, the radiative-convective equilibrium (RCE) vertical profile of potential temperature and water vapor is a function of the four governing thermodynamic parameters: Q_{cool} , T_{tpp} , T_{sst} , and u_{sfc} . Additionally, the generalized potential intensity (Emanuel, 2010), V_p , in RCE can be reformulated as a function of these four governing thermodynamic parameters, Q_{cool} , T_{tpp} , T_{sst} , and u_{sfc} , given by

$$V_p^2 = \frac{T_{sst} - T_{tpp}}{T_{tpp}} \frac{C_p Q_{cool} \overline{\Delta p}}{g \rho C_d |\mathbf{u}|} \quad (4.1)$$

where C_p is the specific heat of air, g is the acceleration due to gravity, ρ is the near-surface air density, and $\overline{\Delta p}$ is a measure of the mean pressure depth of the troposphere. For the purposes of the subsequent analysis, all values of potential intensity presented herein are calculated using the detailed Emanuel sub-routine (Bister and Emanuel, 2002) with zero boundary layer wind speed reduction under pseudo-adiabatic thermodynamics and including dissipative heating.

4.2.2 Description of simulations

Our objective is to explore the sensitivity of TC size to potential intensity, V_p , via modulation of the tropopause temperature, T_{tpp} . We define a Control simulation using the same values for the thermodynamic parameters and exchange coefficients as were used in the axisymmetric case; the values are provided in Table 4.1. We set the rotation rate, f , to $40 \times 10^{-5} \text{ s}^{-1}$, or 8 times the value used in the axisymmetric Control simulation, with the expectation that this will generate smaller storms that require correspondingly smaller domains and therefore reduce the overall computational burden (see Section 4.3). This approach is similar to the work of Khairoutdinov and Emanuel (2012), which explored variations in TC size in f -plane RCE associated with changes in V_p via modulation of T_{sst} . The Control simulation is run on a $1536 \times 1536 \times 25 \text{ km}^3$ doubly-periodic square domain with horizontal and vertical resolutions of $dx = 4 \text{ km}$ and $dz = 625 \text{ m}$, respectively. The model has a rigid lid at the top with a 5-km thick damping layer beneath, and it employs doubly-periodic lateral

Table 4.1: Parameter values for the 3D Control simulation. See text for details.

| Parameter | Value |
|------------|-------------------------------------|
| T_{sst} | 300 K |
| T_{tpp} | 200 K |
| Q_{cool} | 1 K day ⁻¹ |
| u_{sfc} | 3 m s ⁻¹ |
| f | 40×10^{-5} s ⁻¹ |
| C_k, C_d | .0015 |

boundaries in contrast to an outer wall employed in the axisymmetric set-up. The model is initialized in the same manner as the axisymmetric simulations by using the RCE sounding, defined as the time- and horizontal-mean vertical profiles of potential temperature and water vapor for days 70-100, calculated from a three-dimensional simulation on a small 196×196 km² domain that inhibits self-aggregation (for sufficiently small f , here set at $f = 5 \times 10^{-5}$ s⁻¹; see Section 4.3 for discussion of large rotation rates). Though ideally these RCE soundings should be recalculated from simulations using the full Smagorinsky turbulence scheme, turbulence does not have a strong impact on the initial RCE state.

We run four simulations: one Control simulation with $T_{tpp} = 200$ K (CTRL), two simulations with tropopause temperatures of 150 K (PI108), and 250 K (PI43), as well as one simulation with f increased by a factor of 2 (FX2); parameter values for the experiments, including domain size, resolution, and average number of TCs extracted by the tracking algorithm at each output timestep are provided in Table 4.2. Note that PI108 only has one TC in the domain, the potential implications of which are discussed below.

4.2.3 Characterizing statistical equilibrium storm structure

One additional important distinction between the axisymmetric and three-dimensional approaches lies in the characterization of the equilibrium state. Axisymmetric simulation of a tropical cyclone seeks to exploit the near-circular symmetry of TC structure to model a TC directly, and so by definition only produces a single TC in its domain,

Table 4.2: Parameter values for each experiment. N denotes the average number of storms extracted by the algorithm at each time step, and T denotes the length of the statistical equilibrium period over which statistics are accumulated.

| Experiment | T_{tpg} [K] | V_p [ms^{-1}] | f [$\times 10^{-5}$] | dx [km] | L_{domain} [km] | N | T [day] |
|------------|---------------|---------------------|--------------------------|-----------|-------------------|-----|-----------|
| PI108 | 150 | 108.1 | 40 | 4 | 1536 | 1 | 35 |
| CTRL | 200 | 69.7 | 40 | 4 | 1536 | 1.8 | 34 |
| PI43 | 250 | 42.6 | 40 | 2 | 1152 | 3.7 | 27 |
| FX2 | 200 | 69.5 | 80 | 2 | 1152 | 3.7 | 24 |

regardless of domain size. In contrast, three-dimensional simulation of a tropical cyclone in RCE seeks to create a model atmosphere that is capable of supporting a TC, absent any constraints on the structure or behavior of a TC or even the number of TCs that develop in the system. Thus, in the former case, equilibration is defined based simply on the direct evaluation of the time-evolution of the simulated tropical cyclone wind field. In the latter case, the statistical equilibrium state may be characterized by the perpetual decay and regeneration of multiple TCs and therefore must be defined instead based upon the steadiness of some domain-wide quantity. Here we define our statistical equilibrium period based upon the domain-integrated water vapor, which reaches a quasi-steady state after 25-35 days in all simulations presented herein. The statistical equilibrium state is then characterized based on the statistics of the radial wind profiles associated with the array of TCs identified in the domain. Notably, one additional consequence is that the initial disturbance is rendered irrelevant in the three-dimensional case.

As in the axisymmetric case, the background state, from which we calculate relevant environmental quantities including the potential intensity and the radiative-subsidence rate, is ideally characterized as the mean state in the environment beyond the storm circulations. Thus, we define the background state as the mean vertical profile of potential temperature and water vapor at all gridpoints where the near-surface wind speed is below $1\ ms^{-1}$ and the pressure is greater than the mean (to exclude points in the eye of a TC). These profiles are then time-averaged over three

one-day periods corresponding to the first, middle, and last day of each simulation's equilibrium period.

At each three-hourly output time-step during the statistical equilibrium period, we use an objective tracking algorithm to locate TC centers in the domain. This algorithm takes the perturbation pressure field at the surface and zeroes out all data except those with magnitudes more than three standard deviations below the mean in order to isolate regions of data surrounding TC centers. Because of the effects of compressibility and non-hydrostatic accelerations, the minimum pressure value is occasionally offset from the true storm center. Thus, we subsequently apply a nine-point smoother 30 times to smooth the data in order to estimate the center of the TC's broader pressure distribution rather than taking the minimum of the raw pressure data. The algorithm then searches for local minima in the smoothed pressure field with magnitudes greater than 100 Pa within a square neighborhood whose side-length is set equal to the length scale $\frac{V_p}{f}$, which is the theoretical scaling length for TCs at equilibrium (Emanuel, 1986) identified in the axisymmetric simulations of Chapter 3.

We define the minimum pressure threshold relative to the mean, rather than as an absolute quantity, to account for the dependence of minimum pressure on storm size (small storms will have a higher minimum pressure than large storms, all else equal), as well as to attempt to consistently sample from the upper end of the intensity distribution specific to each simulation. As an example, Figure 4-1 displays snapshots of the wind field at $z = 1.5 \text{ km}$ for each simulation, and objectively-identified TC centers are marked. In the cases of PI43 and CTRL, there is at least one TC that can be identified by eye that has not been identified by the algorithm, which is generally true of those simulations with multiple TCs. Clearly this is a conservative algorithm, but one that focuses on mature storms while avoiding more ambiguous cases of storms in the process of genesis or decay.

For each identified TC snapshot (i.e. no compositing), we extract the storm-centered wind field and project it onto the local azimuth in order to isolate the purely rotational component of the wind field. Finally, we calculate the azimuthally-averaged

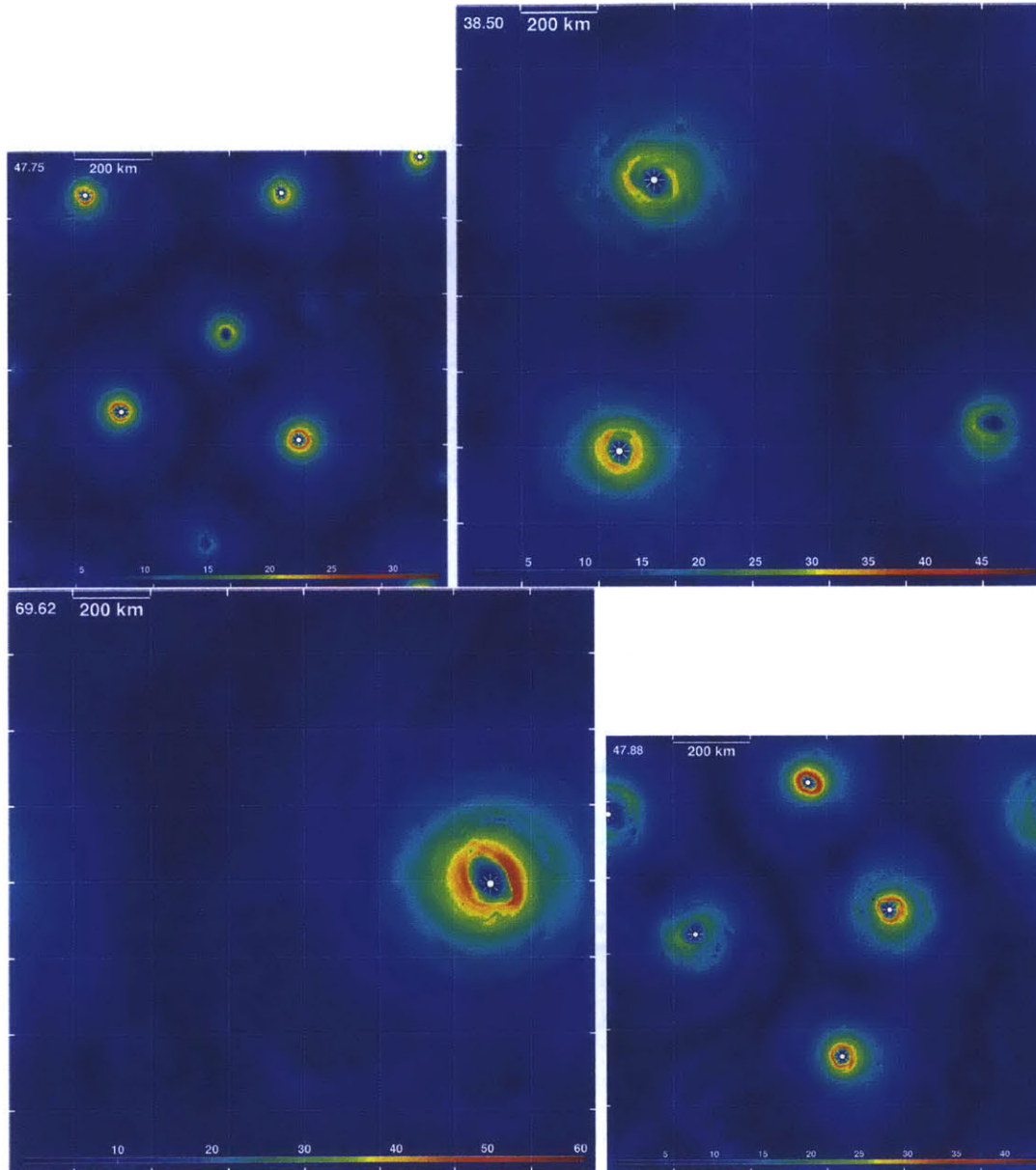


Figure 4-1: Snapshots of the distribution of the full wind speed [ms^{-1}] at $z = 1.5 km$ for PI43 (top left, day 47.75), CTRL (top right, day 38.5), PI108 (bottom left, day 69.62), and FX2 (bottom right, day 47.88). White dots mark objectively-identified TC centers. Image size scales with domain size such that length scales are preserved.

radial profile of the azimuthal wind at $z = 1.5 km$, binning data in radial increments equal to the grid spacing of the simulation of interest. From this radial wind profile, storm structure is characterized by accumulating the statistics of the maximum wind speed, V_m , a proxy for the radius of maximum winds, $r_{ew} = r(.75V_m)$, and two metrics for the outer radius, r_0 , discussed below. The proxy for r_m is used to capture the

outer edge of the eyewall while avoiding the noise in the wind profile around r_m itself.

Importantly, we focus here primarily on metrics of overall storm size. The maximum wind speed is very likely limited by the horizontal resolution, which is coarse relative to the small storm size that is an intentional consequence of the use of an artificially high rotation rate. Furthermore, though one would ideally analyze the gradient wind, this quantity is noisy and cannot be easily time-averaged without a more complex tracking algorithm that follows each individual storm in time. Given that the full wind is only expected to exceed the gradient wind within the eyewall (Bryan and Rotunno, 2009a) where wind speeds are already reduced due to the relatively coarse resolution in our simulations, we use the azimuthal component of the full wind for simplicity.

Following the results of Chapter 3, we estimate the outer radius using the simple slab boundary layer model of Emanuel (2004), which we briefly review here. The model assumes no deep convection, and combines mass continuity with the balance between radial advection of angular momentum and surface drag. The non-dimensional form of the resulting differential equation is given by

$$\frac{\partial(\tilde{r}\tilde{V})}{\partial\tilde{r}} = \frac{C_d V_p}{w_{cool}} \frac{2\tilde{r}^2\tilde{V}^2}{(\tilde{r}_0^2 - \tilde{r}^2)} - \tilde{r} \quad (4.2)$$

where r is the radius and V is the azimuthal wind speed, and tildes denote non-dimensional quantities, where we have non-dimensionalized V by V_p and r by $\frac{V_p}{f}$. The primary assumption of Eq. (4.2) is a match between the Ekman suction rate at the top of the boundary layer and the radiative-subsidence rate, w_{cool} , just above it. Eq. (4.2) is a Riccati equation with no known analytical solution. The value of w_{cool} is calculated from the assumed balance between subsidence-induced warming and radiative cooling

$$w_{cool} \frac{\partial\theta}{\partial z} = Q_{cool} \quad (4.3)$$

where $\frac{\partial\theta}{\partial z}$ is set to its pressure-weighted mean value in the layer $z = 1.5 - 5 \text{ km}$ (i.e. directly above the boundary layer) in the background state. Eq. (4.2) is solved numerically using a shooting method. As noted in Chapter 3, Eq. (4.2) carries with

it an additional mode of variability associated with the non-dimensional parameter $C_2 = \frac{C_d V_p}{w_{cool}}$, which represents the reciprocal of the non-dimensional Ekman suction rate and therefore controls the radial decay rate of the non-dimensional wind field in the far outer region of the storm.

Results from the axisymmetric simulations indicated that this outer wind model is capable of reproducing the entire axisymmetric equilibrium radial wind profile beyond the radius of maximum winds when the first term on the RHS of Eq. (4.2) is multiplied by a constant, taken as $c = .3$; this empirical adjustment accounts for deficiencies in the model assumptions, though the underlying physics are not currently understood and are the worthy subject of future work. Here we find that the best fit constant for each simulation is: CTRL – 1.34; PI43 – 1.18; PI108 – 1.03; FX2 – 1.14. This value is relatively constant across the simulations, with a mean of $c = 1.17$.

For the purposes of direct comparison with the axisymmetric results, we apply an identical methodology for estimating the outer radius by fitting the model to r_{ew} and integrating Eq. (4.2) radially outward, but taking the empirical best-fit constant $c = 1.17$. Additionally, as described in Chapter 3, we calculate an adjusted outer radius, r_0^* , in which C_2 is fixed at its Control value, thereby providing a universal metric for storm size that is independent of the secondary variability that exists only in the non-convecting outer region at large radii.

4.3 TCs in Rotating RCE

4.3.1 Self-aggregation

We first motivate the analysis of TCs in rotating radiative-convective equilibrium through a simple example of convective self-aggregation (Bretherton et al., 2005; Khairoutdinov and Emanuel, 2010) that was initially observed purely by accident. As noted above, the initial RCE state is defined based upon small-domain 3D simulations in a domain with side length $L = 196 \text{ km}$ and in which f was held fixed at a value of $5 \times 10^{-5} \text{ s}^{-1}$. However, as f is successively increased, a threshold is crossed in

which the characteristics of convection transition from a homogenous, disaggregated state to an aggregated state in a finite period of time. This behavior is displayed in Figure 4-2, which depicts snapshots of the wind field at $z = 1.5 \text{ km}$ at day 100 and the accumulated precipitation for days 98-100. In the disaggregated state, low-level wind speeds are uniformly small in magnitude and precipitation is randomly distributed within the domain. In the aggregated state, convection and precipitation are concentrated into a single region in the domain, and the horizontal wind field in this region resembles that of a very weak tropical cyclone. Aggregation does not occur for $f \leq 10 \times 10^{-5}$, but does occur for $f > 20 \times 10^{-5}$. In these latter cases in which aggregation occurs, aggregation is suppressed (at least on the time scale of 100 days) when the domain size is halved to $L = 92 \text{ km}$ at fixed horizontal resolution.

As demonstrated by Held and Zhao (2008) and Khairoutdinov and Emanuel (2012), the rotation rate plays an important role in the length scale of organized convection in rotating RCE. This organization takes the form a TC-like vortex, whose theoretical length scale is proportional to $\frac{V_p}{f}$. The statistical equilibrium state may thus tend toward a “tropical cyclone world” (Khairoutdinov and Emanuel, 2012) characterized by one or more TCs, so long as this length scale is of the same order as, or smaller than, the domain size. Here, $\frac{V_p}{f} = 174 \text{ km}$, corresponding to a diameter of $\sim 350 \text{ km}$, which is approximately double the domain size, though the vortex that develops is clearly far weaker than would be expected given the thermodynamic environment, likely due to the limitations imposed by the domain size in combination with the coarse horizontal resolution. Though an interesting subject in its own right, a deeper analysis of the self-aggregation process is beyond the scope of this study. Here we simply use this observation as a launching point for analyzing TC size in the rotating RCE state.

4.3.2 Radial wind profiles in the presence of multiple TCs

Although rotating RCE can conveniently support multiple TCs simultaneously, it’s not obvious that their respective wind fields will be sufficiently independent of one another to plausibly extract the radial wind profile of an individual storm. However,

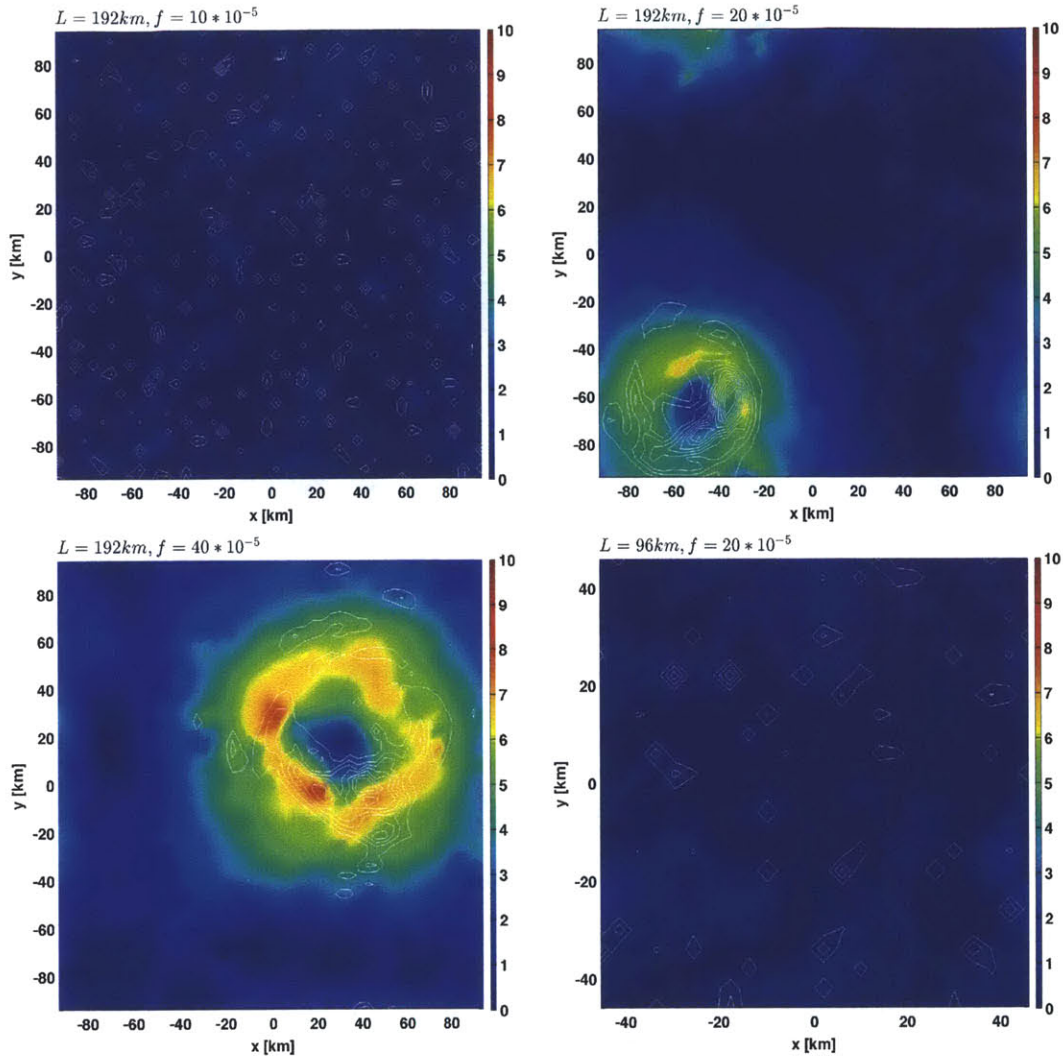


Figure 4-2: Snapshot of windspeed (color) at day 100 and accumulated precipitation over days 98-100 (white contour, 2 cm interval) for four small-domain RCE simulations in which the rotation rate and domain size are varied (respective values listed above each plot). Horizontal resolution is 4 km in all cases.

the interaction of TCs appears to be primarily that of a simple mutual advection/co-rotation (Ritchie and Holland, 2006), such that storms that approach one another temporarily co-rotate before being repelled back to a distance where the interaction ceases. Direct mergers between two mature TCs are rare in these simulations; typically mergers occur only when one storm is already in a process of decay before being “absorbed” into another, mature storm.

As an example, we return to the PI43 snapshot in the top-left panel of Figure

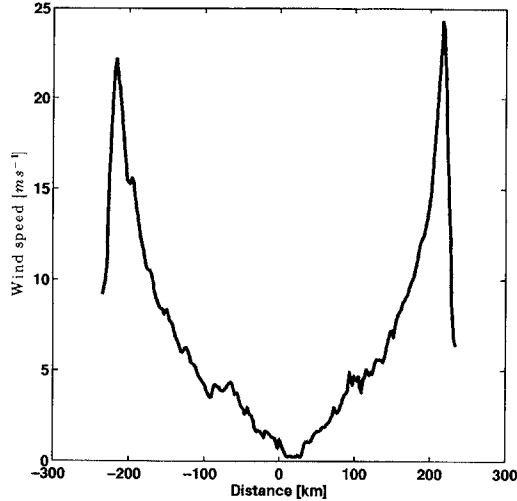


Figure 4-3: Cross-section of the magnitude of the wind speed between the centers of the two dominant TCs in the lower half of the domain of the PI43 snapshot (Figure 4-1, top-left panel).

4-1 in order to highlight the spacing between mature TCs and the honeycomb-like “moats” of very low wind speeds that separate individual storms. The wind profile cross-section connecting the center points of the two dominant TCs in the lower half of the domain is plotted in Figure 4-3. Remarkably, the wind speeds do in fact approach zero very near the mid-point of the two TC centers. Though this is a particularly clean example, such behavior appears to be commonplace at the interface between two or more adjacent storms, which is encouraging for the credible extraction of the azimuthally-averaged radial profile of each storm in the domain.

4.4 Size statistics

We begin with the statistics of the dimensional structural parameters. Figure 4-4 compares the PDFs and respective median values of V_m , r_{ew} , r_0 , and r_0^* across all objectively-identified TC snapshots within each simulation. Within the inner core, the distribution of V_m increases slowly with increasing V_p , from a median of 22 m s^{-1} in PI43 to 30 m s^{-1} in PI108. The distribution decreases slightly going from CTRL to FX2 despite the doubled horizontal resolution in the latter. Similar qualitative

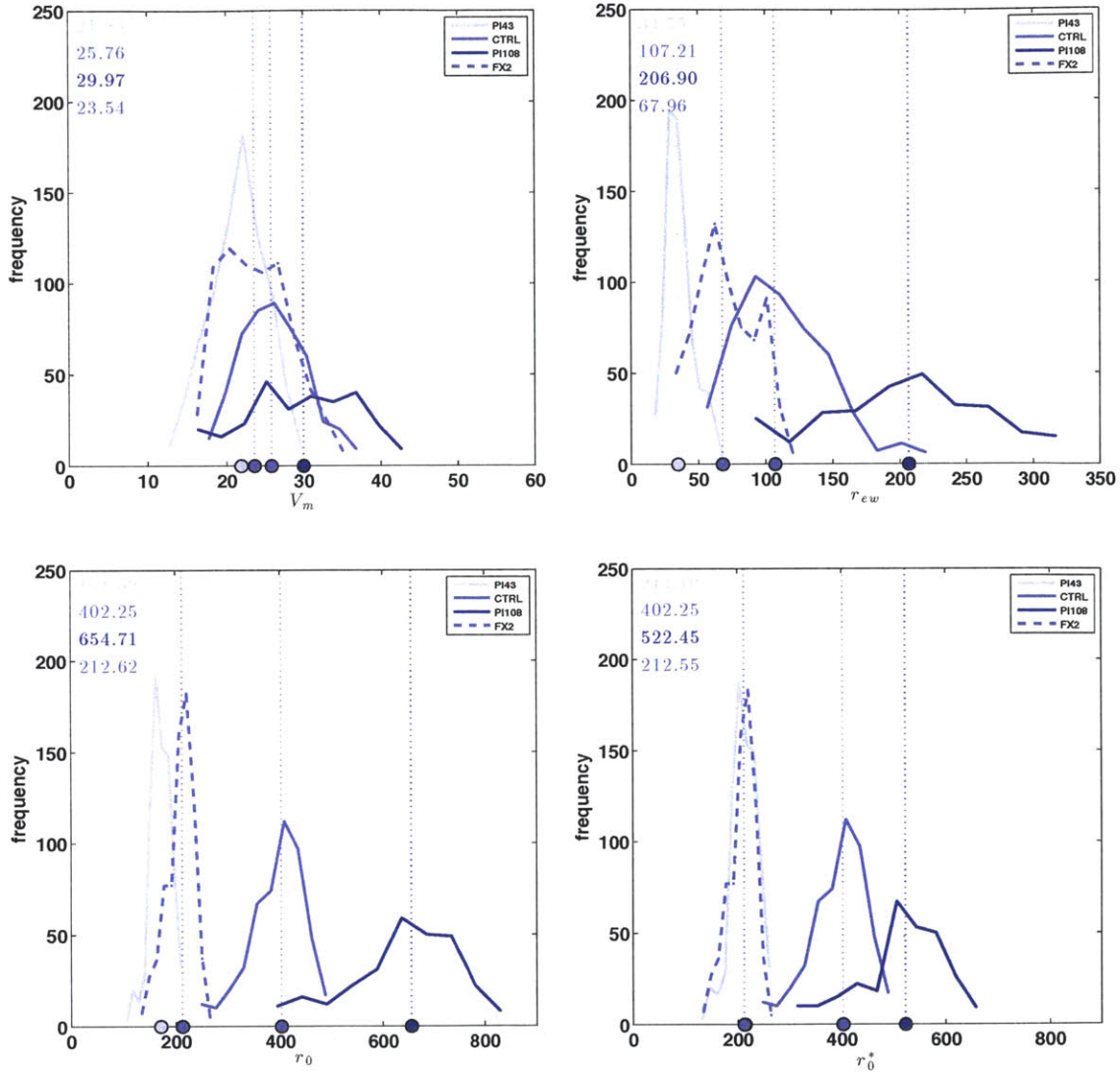


Figure 4-4: Probability distributions for V_m (top left), r_{ew} (top right), r_0 (bottom left), and r_0^* (bottom right) for all four simulations. Median values plotted (dashed line, marker) and listed in the top left corner of each plot. Shading denotes potential intensity from low (light) to high (dark).

behavior is observed for r_{ew} , whose median increases rapidly from 35 km (PI43) to 207 km (PI108) with increasing V_p , and whose respective distributions simultaneously broaden while retaining a largely symmetric shape. As for the broader circulation, our estimate of r_0 also increases rapidly with V_p , while r_0^* increases slightly more gradually because C_2 has been held fixed.

A more insightful perspective lies in the analysis of the non-dimensional structural

parameters, where V is non-dimensionalized by V_p and r by $\frac{V_p}{f}$, as shown in Figure 4-5. The distribution of non-dimensional V_m is nearly constant across the simulations, with the exception of PI43, whose median value is nearly twice as large. This suggests that each simulation is similarly resolved in non-dimensional space and thus lends credibility to a comparison across simulations. In the case of the low- V_p simulation, the fact that it appears to be better resolved than the others is encouraging and is certainly preferable to being under-resolved relative to the other simulations.

The non-dimensional r_{ew} still exhibits a significant increase with increasing V_p , with median values of .33, .62, and .77 for PI43, CTRL, and PI108, respectively, indicating that this quantity in fact scales faster than the length scale $\frac{V_p}{f}$. Curiously, for FX2 the median non-dimensional r_{ew} also increases significantly compared with the CTRL simulation, from .62 to .78. This behavior was not observed in the axisymmetric simulations. Moreover, the values for r_{ew} are quite large relative to the axisymmetric results, in which the non-dimensional r_{ew} values were $\sim .05$ for the Control simulation.

Finally, the non-dimensional r_0 increases with increasing V_p , from 1.61 to 2.42 (Figure 4-5, lower-left panel), though the majority of this increase occurs between PI43 and CTRL. Meanwhile, the non-dimensional r_0^* brings the median values for the set of simulations into closer alignment (Figure 4-5, lower-right panel). All median values fall within the range 1.93 – 2.45. This result provides some evidence in support of the results of the axisymmetric simulations, in which it was found that r_0^* scaled nearly linearly with $\frac{V_p}{f}$. Additionally, the much larger value for c in three dimensions suggests that the outer wind field of 3D storms decay significantly more gradually than their axisymmetric counterparts.

The shape of the distributions of the outer radius provides additional information regarding TCs in this rotating RCE state. First, these distributions are relatively narrow, reflecting the fact that the outer circulation does indeed remain quite stable with time despite large variations in inner-core structure, corroborating both the axisymmetric results and observations of real TCs (Weatherford and Gray, 1988). Second, the distributions of r_0 have a prominent lower tail but only a minimal upper

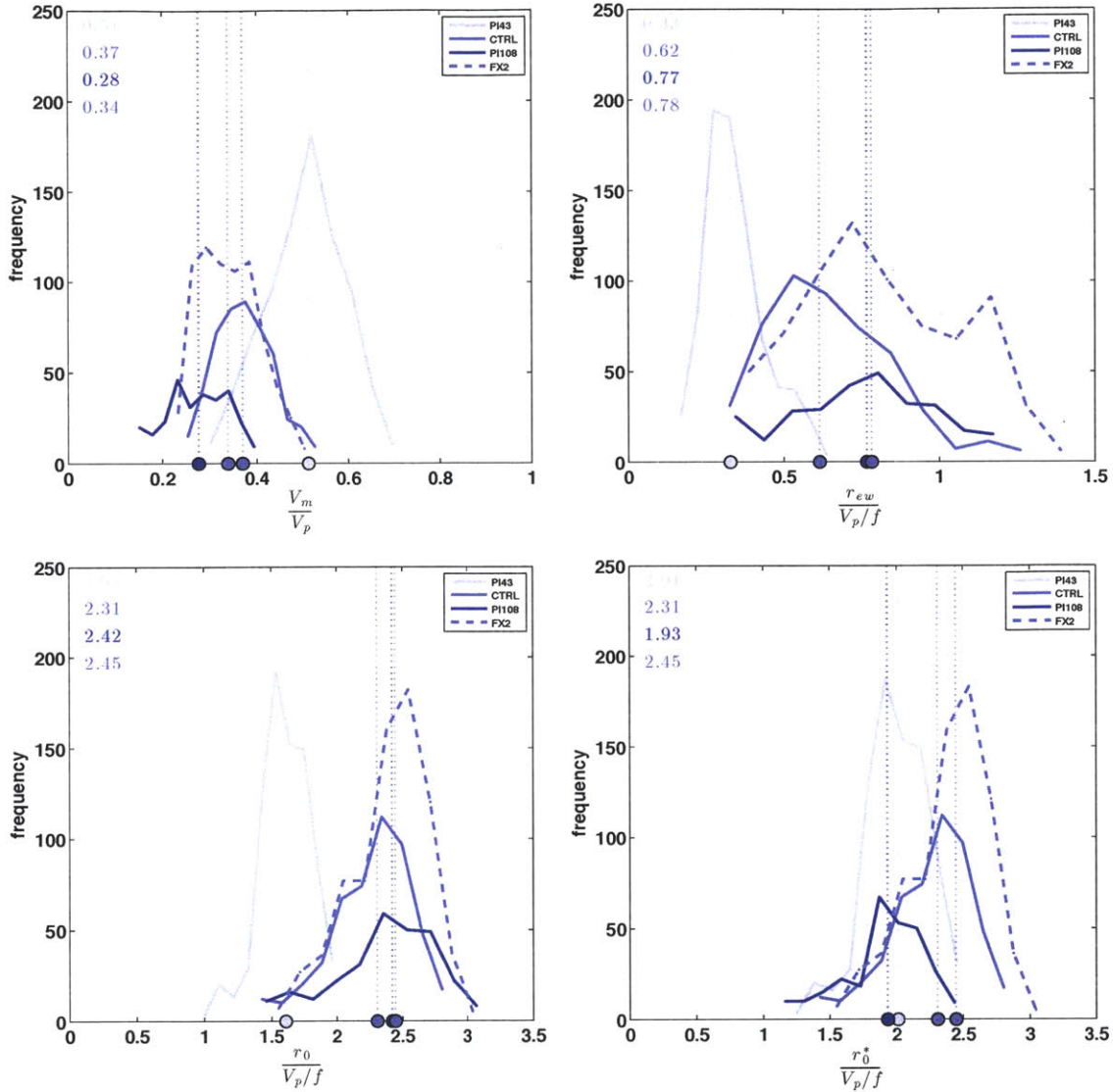


Figure 4-5: As in Figure 4-4, but with V_m non-dimensionalized by V_p and radii non-dimensionalized by $\frac{V_p}{f}$.

tail above the mode of the distribution, indicating that TCs are not exceeding their characteristic size. This is in direct contrast to the axisymmetric results, in which TCs exhibit a transient super-equilibrium phase in both intensity and size, a state that is not likely to be missed by the tracking algorithm. Instead, the existence of the lower tail suggests that TCs either first intensify and then expand early in their life-cycle, or else first contract and then decay late in their life-cycle. cursory observations of the output suggest that the former appears to be the common case. An algorithm

that tracks the life-cycle of individual TCs would allow for analysis of the trajectory of each storm through the joint (V_m, r_0^*) phase space, which will be the subject of future work.

Overall, TCs in this framework appear to be larger than their axisymmetric counterparts. In the latter, the typical magnitude of non-dimensional r_0^* was $\sim .5$. In three-dimensions, this magnitude is $\sim 2 - 2.5$, which qualitatively matches the results of Khairoutdinov and Emanuel (2012). Meanwhile, r_{ew} is significantly larger than in axisymmetry, though this result may be subject to several important caveats discussed below. This contrast in absolute sizes may reflect the tendency for convection in axisymmetry to be confined solely to the eyewall, whereas three-dimensional TCs must contend with the asymmetric nature of both radial turbulence and convection itself, as well as other asymmetric effects associated with translation and interaction with other TCs in the domain.

4.5 Discussion

Though these results are interesting, there are many caveats that must be acknowledged. First, the number of TCs in the domain may affect the structure of any single TC. In particular, the high- V_p simulation can only fit one TC in the domain. If this storm does not fit neatly within the domain, though, then the remaining space will be left open when it would otherwise be at least partially occupied by another TC in a larger domain. Because the entire domain is cooling radiatively, and radiative cooling must be energetically balanced by precipitation, which occurs almost entirely within TCs in the aggregated state, the existence of large regions of open space absent a TC implies that the lone TC in the domain must necessarily generate more precipitation than it might otherwise in a multi-TC state. Given constraints on the terminal velocity of rain and the constancy of boundary layer water vapor content as T_{tpp} or f is varied, this may lead to an expansion of the area of the precipitating region, which may cause an expansion of the TC. Indeed, the lone TC in PI108 weakens by about 50% during simulation days 55-65 before reintensifying back to its original

state, perhaps a consequence of the fact that the equilibrium state to which the TC tends cannot simultaneously exist at domain-wide equilibrium in the domain in which it is embedded. This effect may also be playing a role in the CTRL simulation as well, in which 2-3 TCs are typically present, yet it appears that a 4th storm could nearly fit into the remaining open space. More generally, one might expect this effect to decrease in influence as the domain is increasingly well-packed; how rapidly the magnitude of this effect would drop off is not known, and may be different depending on the specific quantity of interest.

Nonetheless, there seems to be a signal in overall storm size that emerges despite the above caveats. The distributions of r_0 are relatively narrow, a feature that is perhaps most evident in the case of PI108 despite the fact that its corresponding distribution of r_{ew} is the *broadest* of all simulations. This provides evidence that scalings for overall storm size may be reasonably captured in the simulations presented here. Indeed, the radiative effect discussed above may require an expansion of the TC's precipitation field, which may lead to an increase in the inner core size of the TC wind field, but if the broad outer circulation is not strongly affected by variability in the inner core, then it is plausible that the scaling for the outer circulation may remain largely unchanged.

4.6 Conclusions

Here we have explored the statistics of the size and structure of tropical cyclones that emerge within a set of idealized three-dimensional, rotating RCE simulations at statistical equilibrium. These RCE simulations are set-up under the identical thermodynamic environment as the axisymmetric simulations of Chapter 3. Importantly, here a full three-dimensional turbulence scheme is included that liberates us from the axisymmetric horizontal turbulent mixing length, l_h , which exerts a strong influence on the inner-core structure in axisymmetry.

The primary result of this analysis is the finding that a measure of the overall size of the storm, given by the outer radius calculated using a simple slab boundary layer

outer wind model and adjusted to account for dependence on the potential intensity in the far outer region of the storm, scales approximately linearly with $\frac{V_p}{f}$ as was found in the axisymmetric simulations of Chapter 3. This provides further evidence that the theoretical length scale of TCs, $\frac{V_p}{f}$, given by Emanuel (1986) does indeed govern the overall size of an equilibrium TC, corroborating the results of Khairoutdinov and Emanuel (2012) for varying T_{sst} . Our proxy for the radius of maximum wind is surprisingly found to scale super-linearly with $\frac{V_p}{f}$, though we have low confidence in the fidelity of this result given the coarse resolution of the model relative to the size of the TCs, which was made intentionally small in order to accommodate more TCs at lower computational expense.

Additionally, the distributions of size across our simulations appear to be firmly bounded from above, indicating that TCs do not undergo a transient super-equilibrium phase in size as was found in the axisymmetric case, at least in the context of storms that develop within the statistically-equilibrated TC world. This result suggests that the super-equilibrium phase may be a product of the parameterized turbulence scheme employed in axisymmetry or else to the unique dynamics associated with axisymmetric geometry. Moreover, this result appears to better match observations of TCs in nature, whose broad outer circulations are not typically observed to contract during its life-cycle (Chavas and Emanuel, 2010).

There remain several caveats to the analysis performed here that will be addressed in future work. In particular, for those simulations in which there are only one or a couple of TCs in the domain, the combination of the geometry of the domain and the need for precipitation to balance domain-wide radiative cooling may force the precipitating inner core of the TC(s) to expand relative to its true equilibrium value, which would be obtained in a domain that is neatly-packed with TCs. Additionally, dependencies on horizontal resolution must be further addressed. However, given the axisymmetric simulation results and the steadiness of the broad outer circulation relative to the turbulent inner core of real TCs (Weatherford and Gray, 1988), the behavior of the overall size of a TC may not be strongly affected by these issues. Finally, a better understanding of the physics of the outer wind region would help

improve our methodology for estimating r_0 .

Chapter 5

Conclusions and Future Work

5.1 Summary

Tropical cyclones in nature are known to span a large range of sizes, yet the factors that govern storm size remain enigmatic, whether in the context of an individual TC at genesis and during its life-cycle or in the context of its global distribution. Despite major advances over the past few decades in our understanding of the genesis, motion, intensity, and structure of TCs, as well as the two-way interaction between TCs and the environment (both atmosphere and upper ocean) in which they are embedded, size appears to behave largely independently of all of these factors and thus is effectively unconstrained. Theoretically, storm size, defined as the outer radius, r_0 , where the winds vanish, is literally a free parameter, with the exception of a scaling for its theoretical upper bound given by the ratio of the potential intensity to the Coriolis parameter.

This work takes the first steps toward a more fundamental understanding of TC size. First, a climatology of size, as measured by an estimate of r_0 , is created from the QuikSCAT satellite database. This climatology reveals that storm size is approximately log-normally distributed globally and spans a wide range of values ranging from 100 km to 1600 km, perhaps an indication that size is indeed an unconstrained random variable as intimated by current theory. However, the median values of size are distinct across basins, suggesting that size is modulated by variations in the ther-

mododynamic environment, in the distribution of initial disturbances, or both. The time-evolution of storm size exhibits a high degree of variability, but on average storms are found to expand gradually early in their life-cycle before stabilizing.

TC size is then investigated in a highly-idealized thermodynamic environment using the Bryan Cloud Model (CM1), with a focus on the determinants of the equilibrium state. Overall, the dominant length scale for the equilibrium storm is found to be $\frac{V_p}{f}$, matching the scale for the theoretical upper bound on TC size given by existing potential intensity theory. Contrary to conventional wisdom based on geostrophic adjustment, the Rossby deformation radius is shown not to be fundamental to equilibrium size.

In axisymmetry, the inner storm structure (i.e. intensity and size) of the equilibrium storm is modulated primarily by a single non-dimensional parameter, $\frac{V_p}{fl_h}$. This non-dimensional parameter represents the ratio of the storm length scale, $\frac{V_p}{f}$, to the parameterized eddy mixing length, l_h . This parameter modulates the effective turbulence felt by a storm of a given size; a higher value of V_p corresponds to a storm that is both more intense *and* larger, and therefore it feels a weaker effective turbulence, resulting in a further increase in V_m above and beyond a linear scaling with V_p . Meanwhile, the far outer region of the storm is modulated by a second non-dimensional parameter, $\frac{C_d V_p}{w_{cool}}$, that emerges from a simple slab boundary layer model of the outer wind field that assumes no deep convection.

This idealized framework is then explored in a set of three-dimensional simulations, liberated from the outsized influence of the axisymmetric parameterized turbulent length scales that lack a strong theoretical basis. These simulations reveal that overall storm size scales with $\frac{V_p}{f}$, as was found in axisymmetry, though this result is the subject of ongoing work. When varying V_p , the radius of maximum wind was surprisingly found to scale more rapidly than this length scale, though domain and resolution dependencies limit the confidence that can be placed in this result.

In axisymmetry, the time-scales to structural equilibrium are found to be quite long, as the model TC exhibits a transient phase during which storm size significantly overshoots its equilibrium value before relaxing to equilibrium after more than 50 days

for the Control simulation. In three-dimensions, as well as arguably in observations, there is no evidence of such a super-equilibrium phase, suggesting that this behavior is specific to axisymmetric geometry.

Overall, this work has taken the first steps towards a more comprehensive, fundamental understanding of TC size. There remains a significant gap to be filled between the characterization of storm size in observations and in the idealized modeling world explored here. Nonetheless, these results in combination suggest that storm structure may potentially be represented simply as a combination of radial wind profile solutions in the convecting inner region and non-convecting outer region, each of which are subject to distinct, though reasonably well-understood, dynamics. Moreover, though the equilibrium results cannot explain the observed dynamics and distribution of storm size, they do indicate the end point towards which TC size evolves, even if such an evolution is actually too slow to be observed in nature. More research is needed to continue to build our understanding from all perspectives: observations, idealized models, and theory.

5.2 Future Work

There is a multitude of avenues for future work, as the work presented herein presents only the first steps towards understanding TC size in nature. Much more work remains to be done.

5.2.1 Ventilation and equilibrium size

The work performed here explored TCs in a veritable environmental paradise: axisymmetry in the absence of any vertical wind shear or other impediments to storm intensity. Tang and Emanuel (2010) derived a solution for a ventilation-modified steady-state potential intensity that accounts for the import of low-entropy air into the core of the TC by vertical wind shear. Thus, one sensible follow-on question is whether equilibrium TC size scales with the unmodified potential intensity in its original form or that modified by ventilation. Tang and Emanuel (2012) demonstrated

a framework for incorporating the effects of vertical wind shear, which is a non-axisymmetric process, into an axisymmetric model by imposing a locally-enhanced parameterized diffusion, which mixes external dry air into the core of the storm. Such a framework could be combined with the approach applied in the work presented here to explore how equilibrium size responds to a thermodynamic environment whose potential intensity is reduced due to the presence of steady ventilation. Additionally, one could start from a storm equilibrated to the unventilated potential intensity and quantify the time-scales for structural re-equilibration following the sudden onset of ventilation.

5.2.2 Transient size evolution

Given an equilibrium size and structure toward which a storm tends, what governs the time-dependent evolution towards this equilibrium solution? This work identified the existence of long time-scales to structural equilibrium in axisymmetry, particularly in the context of storm size. Further work is needed to quantify the processes and non-dimensional parameters that govern these time-scales, though some recent theoretical work (Emanuel, 2012), which derived an analytical solution for the time-dependent evolution of storm intensity, may provide some guidance. Though it is not clear whether this super-equilibrium period is applicable to the three-dimensional world, an understanding of the time evolution of size in both contexts would be illuminating. Storm size at genesis, as well as its subsequent evolution, remains largely unpredictable in nature, and analysis of the simplified axisymmetric framework may offer insights applicable to the real world, even in the context of an unphysical representation of turbulence. However, although the physics of the mature TC appears readily represented within a purely axisymmetric framework, it is not clear whether the genesis process can be properly captured in this way or whether it is fundamentally a three-dimensional process (e.g. Montgomery et al. (2006); Simpson et al. (1997)), particularly given the highly axially-asymmetric distribution of convection that typically pervades the incipient disturbance during its development.

5.2.3 Validation of outer wind field model

This work found that the simple slab outer wind model of Emanuel (2004), with a single empirical modification, could represent the entire outer wind field of the axisymmetric TC over a surprisingly large array of simulations. A deeper analysis of this outer wind model would be highly beneficial to understand the physics behind this modification and when it breaks down, as well as the extent to which the success of the model is a function of the simplicity of the numerical model set-up employed here. Perhaps if given a boundary layer that is resolved in much greater detail, the simple empirical modification will no longer be appropriate. Ideally, one seeks an updated outer wind model that properly captures the underlying physics of the outer wind region and therefore can be used to model the full outer wind field absent any empirical modifications. Though this slab model has been widely critiqued in the context of the inner-core wind field (Smith and Montgomery, 2008; Persing and Montgomery, 2003; Smith and Vogl, 2008), it has not been thoroughly tested in the context of the quiescent, non-convecting outer region, where simplicity and validity may more readily go hand-in-hand.

5.2.4 TC size in more complex environments

This work has identified the dominant scaling for equilibrium TC size within a highly idealized environment. Based on these results, more detailed simulations would be useful in exploring with much greater precision, particularly in three dimensions, how these results are modulated by the many real-world processes not resolved or included in this environment. Such processes include a detailed representation of the boundary layer, higher horizontal resolution within the eye, realistic radiative transfer, and inclusion of external environmental interactions such as vertical wind shear (as discussed above) and an interactive ocean. Moreover, though radiative-convective equilibrium is a simple and useful representation of a tropical atmosphere, the real tropics contains much greater horizontal heterogeneity, including overturning circulations such as the Hadley and Walker cells and intra-seasonal variability such

as Equatorial waves and the MJO (Kiladis et al., 2009). Thus, exploring TC size in idealized environments other than RCE, such as under the weak temperature gradient assumption (Sobel and Bretherton, 2000), may provide insight into TC size in different regional tropical climate regimes.

5.2.5 TC size in the current climate: explaining the log-normal

What determines the observed log-normal distribution of size in nature? Ultimately, a deeper understanding of the dynamics of TC size should entail an explanation of the nature and parameters (median, variance, etc.) of this distribution. Such an explanation may arise from the combination of a fundamental understanding of initial size and size evolution at the level of individual storms and the climatological statistics of those parameters deemed relevant to size. For example, evidence from observations and modeling suggests that the scale of the initial condition plays an important role in setting the size of the storm early in its life-cycle. If this relationship can be more precisely quantified (e.g. the specific variable/quantity whose length scale is relevant, the time-scales over which it is relevant), then an understanding of the statistics of initiating disturbances, as well as the underlying physics that generate such statistics, may be useful in explaining the statistics of storm size overall. Additionally, the statistics of the environments in which they are embedded may also be relevant, particularly in the context of a non-stationary climate, given evidence that the climate state can have a strong influence on the statistics of genesis itself (Rappin et al., 2010).

However, it should be noted that there is also evidence of more fundamental two-way interactions between TCs and climate which could potentially also manifest itself in terms of TC size. TC activity may have significant impacts on meridional ocean heat transport (Jansen and Ferrari, 2009) and the atmospheric general circulation (Hart, 2011) on seasonal or annual timescales. Moreover, Khairoutdinov and Emanuel (2010) put forth the hypothesis that the tropical climate is an example of a self-organized critical system, such that the tropics tend toward a critical phase transition

between disaggregated and aggregated convection, the latter of which includes TCs. Whether there is a role to play for a metric of TC activity that includes size, such as the Power Dissipation Index (Emanuel, 2005), in modulating climate is an open topic of research, but it is not out of the question that the log-normal distribution is one manifestation of such a complex interdependence within the climate system.

5.2.6 TC size under climate change

The effects of a changing climate on TC size is unknown. Theory (Emanuel, 1987) and GCMs (Knutson et al., 2010) indicate a global increase in potential intensity of $\sim 10\%$ due to a doubling of atmospheric carbon dioxide concentrations. Based on the $\frac{V_p}{f}$ scaling for the equilibrium storm, one reasonable hypothesis entails a concurrent upward shift in the median of the log-normal size distribution. Such a hypothesis may be tested within GCM simulations. However, size in GCMs remains a largely unexplored topic under any climate. Quantifying variations in storm size in a changing climate and attributing these variations to variations in the statistics of potential intensity, initiating disturbances, genesis locations, tracks, and their underlying physical mechanisms, would be of great value in its own right, and also would provide useful datasets for application and validation of hypotheses for the theoretical relationships between TC size, the local environment, and climate. Undoubtedly, this is a particularly complex problem that integrates together the time-dependent physics of TC size at the individual storm level, the modulation of TC activity by the climate system, including the spatial and temporal distribution of genesis and intensification, and the large-scale changes in the climate system anticipated due to changes in radiative forcing, such as that associated with anthropogenic greenhouse gas emissions.

Bibliography

- Betts, A., 1986: A new convective adjustment scheme. Part I: Observational and theoretical basis. *Quarterly Journal of the Royal Meteorological Society*, **112** (473), 677–691.
- Beven, J., 2000: Tropical cyclone report: Hurricane Alberto (2000). *National Hurricane Center*.
- Bister, M. and K. Emanuel, 2002: Low frequency variability of tropical cyclone potential intensity. part 1: Interannual to interdecadal variability. *Journal of Geophysical Research*, **107** (D24), 4801.
- Bister, M. and K. A. Emanuel, 1997: The genesis of Hurricane Guillermo: TEXMEX analyses and a modeling study. *Monthly Weather Review*, **125** (10), 2662–2682.
- Bister, M. and K. A. Emanuel, 1998: Dissipative heating and hurricane intensity. *Meteorology and Atmospheric Physics*, **65** (3-4), 233–240.
- Blake, E. S., T. B. Kimberlain, R. Berg, C. J. P, and J. L. Beven II, 2013: Tropical cyclone report: Hurricane Sandy (AL182012), 22–29 October 2012. *National Hurricane Center*.
- Braun, S. A., J. A. Sippel, and D. S. Nolan, 2012: The impact of dry midlevel air on hurricane intensity in idealized simulations with no mean flow. *Journal of the Atmospheric Sciences*, **69** (1), 236–257.
- Brennan, M. J., C. C. Hennon, and R. D. Knabb, 2009: The operational use of QuikSCAT ocean surface vector winds at the National Hurricane Center. *Weather and Forecasting*, **24** (3), 621–645.
- Bretherton, C. S., P. N. Blossey, and M. Khairoutdinov, 2005: An energy-balance analysis of deep convective self-aggregation above uniform SST. *Journal of the Atmospheric Sciences*, **62** (12), 4273–4292.
- Bryan, G. H., 2011: Effects of surface exchange coefficients and turbulence length scales on the intensity and structure of numerically simulated hurricanes. *Monthly Weather Review*, **140** (4), 1125–1143.
- Bryan, G. H. and J. M. Fritsch, 2002: A benchmark simulation for moist nonhydrostatic numerical models. *Monthly Weather Review*, **130** (12), 2917–2928.

- Bryan, G. H. and R. Rotunno, 2009a: Evaluation of an analytical model for the maximum intensity of tropical cyclones. *Journal of the Atmospheric Sciences*, **66** (10), 3042–3060.
- Bryan, G. H. and R. Rotunno, 2009b: The maximum intensity of tropical cyclones in axisymmetric numerical model simulations. *Monthly Weather Review*, **137** (6), 1770–1789.
- Chan, K. T. and J. C. Chan, 2012: Size and strength of tropical cyclones as inferred from QuikSCAT data. *Monthly Weather Review*, **140** (3), 811–824.
- Chavas, D., E. Yonekura, C. Karamperidou, N. Cavanaugh, and K. Serafin, 2013: U.S. hurricanes and economic damage: An extreme value perspective. *Natural Hazards Review*, **in press**.
- Chavas, D. R. and K. A. Emanuel, 2010: A QuikSCAT climatology of tropical cyclone size. *Geophysical Research Letters*, **37** (18), 10–13.
- Cheng-Shang, L., K. K. W. Cheung, F. Wei-Ting, and R. L. Elsberry, 2010: Initial maintenance of tropical cyclone size in the western North Pacific. *Monthly Weather Review*, **138** (8), 3207–3223.
- Chou, K.-H., C.-C. Wu, P.-H. Lin, and S. Majumdar, 2010: Validation of QuikSCAT wind vectors by dropwindsonde data from dropwindsonde observations for typhoon surveillance near the taiwan region (DOTSTAR). *Journal of Geophysical Research: Atmospheres*, **115** (D2).
- Cocks, S. B. and W. M. Gray, 2002: Variability of the outer wind profiles of western North Pacific typhoons: Classifications and techniques for analysis and forecasting. *Monthly Weather Review*, **130** (8), 1989–2005.
- Corbosiero, K. L., J. Molinari, A. R. Aiyyer, and M. L. Black, 2006: The structure and evolution of Hurricane Elena (1985). Part II: Convective asymmetries and evidence for vortex Rossby waves. *Monthly Weather Review*, **134** (11), 3073–3091.
- Dean, L., K. A. Emanuel, and D. Chavas, 2009: On the size distribution of atlantic tropical cyclones. *Geophysical Research Letters*, **36** (14).
- DeMaria, M. and J. D. Pickle, 1988: A simplified system of equations for simulation of tropical cyclones. *Journal of Atmospheric Sciences*, **45**, 1542–1554.
- Demuth, J. L., M. DeMaria, and J. A. Knaff, 2006: Improvement of advanced microwave sounding unit tropical cyclone intensity and size estimation algorithms. *Journal of Applied Meteorology and Climatology*, **45** (11), 1573–1581.
- Dunnavan, G. M. and J. W. Diercks, 1980: An analysis of Super Typhoon Tip (October 1979). *Monthly Weather Review*, **108** (11), 1915–1923.
- Elsberry, R., 1995: Global perspectives on tropical cyclones. *WMO Tech. Doc*, **693**.

- Emanuel, K., 1987: The dependence of hurricane intensity on climate. *Nature*, **326 (6112)**, 483–485.
- Emanuel, K., 1994: *Atmospheric Convection*. Oxford University Press, USA, URL <http://books.google.com/books?id=VdaBBHEGAcMC>.
- Emanuel, K., 2000: A statistical analysis of tropical cyclone intensity. *Monthly Weather Review*, **128 (4)**, 1139–1152.
- Emanuel, K., 2003: Tropical cyclones. *Annual Review of Earth and Planetary Sciences*, **31 (1)**, 75–104.
- Emanuel, K., 2005: Increasing destructiveness of tropical cyclones over the past 30 years. *Nature*, **436 (7051)**, 686–688.
- Emanuel, K., 2010: Tropical cyclone activity downscaled from NOAA-CIRES reanalysis, 1908–1958. *Journal of Advances in Modeling Earth Systems*, **2 (1)**, 1–12.
- Emanuel, K., 2012: Self-stratification of tropical cyclone outflow. Part II: Implications for storm intensification. *Journal of the Atmospheric Sciences*, **69 (3)**, 988–996.
- Emanuel, K. and R. Rotunno, 2011: Self-stratification of tropical cyclone outflow. Part I: Implications for storm structure. *Journal of the Atmospheric Sciences*, **68 (10)**, 2236–2249.
- Emanuel, K. A., 1986: An air-sea interaction theory for tropical cyclones. Part I: Steady-state maintenance. *Journal of the Atmospheric Sciences*, **43 (6)**, 585–605.
- Emanuel, K. A., 1989: The finite-amplitude nature of tropical cyclogenesis. *Journal of the Atmospheric Sciences*, **46 (22)**, 3431–3456.
- Emanuel, K. A., 1995a: The behavior of a simple hurricane model using a convective scheme based on subcloud-layer entropy equilibrium. *Journal of the Atmospheric Sciences*, **52 (22)**, 3960–3968.
- Emanuel, K. A., 1995b: Sensitivity of tropical cyclones to surface exchange coefficients and a revised steady-state model incorporating eye dynamics. *Journal of the Atmospheric Sciences*, **52 (22)**, 3969–3976.
- Emanuel, K. A., 1997: Some aspects of hurricane inner-core dynamics and energetics. *Journal of the Atmospheric Sciences*, **54 (8)**, 1014–1026.
- Emanuel, K. A., 2004: Tropical cyclone energetics and structure. *Atmospheric Turbulence and Mesoscale Meteorology*, F. E. R. Rotunno, and S. B., Eds., Cambridge University Press.
- Evans, J. L. and R. E. Hart, 2003: Objective indicators of the life cycle evolution of extratropical transition for Atlantic tropical cyclones. *Monthly Weather Review*, **131 (5)**, 909–925.

- Frank, W. M., 1977: The structure and energetics of the tropical cyclone. Part I: Storm structure. *Monthly Weather Review*, **105** (9), 1119–1135.
- Fudeyasu, H. and Y. Wang, 2011: Balanced contribution to the intensification of a tropical cyclone simulated in TCM4: Outer-core spinup process. *Journal of the Atmospheric Sciences*, **68** (3), 430–449.
- Hakim, G. J., 2011: The mean state of axisymmetric hurricanes in statistical equilibrium. *Journal of the Atmospheric Sciences*, **68** (6), 1364–1386.
- Hart, R. E., 2011: An inverse relationship between aggregate northern hemisphere tropical cyclone activity and subsequent winter climate. *Geophysical Research Letters*, **38** (1), 705.
- Hart, R. E. and J. L. Evans, 2001: A climatology of the extratropical transition of Atlantic tropical cyclones. *Journal of Climate*, **14** (4), 546–564.
- Hartmann, D. L., J. R. Holton, and Q. Fu, 2001: The heat balance of the tropical tropopause, cirrus, and stratospheric dehydration. *Geophys. Res. Lett.*, **28** (10), 1969–1972.
- Held, I. M., 2005: The gap between simulation and understanding in climate modeling. *Bulletin of the American Meteorological Society*, **86** (11), 1609–1614.
- Held, I. M. and M. Zhao, 2008: Horizontally homogeneous rotating radiative-convective equilibria at GCM resolution. *Journal of the Atmospheric Sciences*, **65** (6), 2003–2013.
- Hill, K. A. and G. M. Lackmann, 2009: Influence of environmental humidity on tropical cyclone size. *Monthly Weather Review*, **137** (10), 3294–3315.
- Hoffman, R. N. and S. M. Leidner, 2005: An introduction to the near-real-time QuikSCAT data. *Weather and Forecasting*, **20** (4), 476–493.
- Iman, R. L., M. E. Johnson, and C. C. Watson Jr., 2005: Sensitivity analysis for computer model projections of hurricane losses. *Risk Analysis*, **25** (5), 1277–1297.
- Irish, J. L. and D. T. Resio, 2010: A hydrodynamics-based surge scale for hurricanes. *Ocean Engineering*, **37** (1), 69–81.
- Irish, J. L., D. T. Resio, and J. J. Ratcliff, 2008: The influence of storm size on hurricane surge. *Journal of Physical Oceanography*, **38** (9), 2003–2013.
- Jansen, M. and R. Ferrari, 2009: Impact of the latitudinal distribution of tropical cyclones on ocean heat transport. *Geophysical Research Letters*, **36** (6), 604.
- Jarvinen, B. R., C. J. Neumann, and M. A. S. Davis, 1984: A tropical cyclone data tape for the North Atlantic basin, 1886–1983: Contents, limitations, and uses. *NOAA Tech. Memo., NWS NHC 22*.

- Katz, R. W., 2012: Economic impact of extreme events: An approach based on extreme value theory. *Extreme Events: Observations, Modeling and Economics*, J. U.-F. M. Ghil and M. Chavez, Eds., American Geophysical Union, in press.
- Khairoutdinov, M. F. and K. Emanuel, 2010: Aggregated convection and the regulation of tropical climate. *29th Conference on Hurricanes and Tropical Meteorology, Tuscon, AZ, Amer. Meteo. Soc: Boston*.
- Khairoutdinov, M. F. and K. Emanuel, 2012: The effects of aggregated convection in cloud-resolved radiative–convective equilibrium. *30th Conference on Hurricanes and Tropical Meteorology, Ponte Vedra Beach, FL, Amer. Meteo. Soc: Boston*.
- Kiladis, G. N., M. C. Wheeler, P. T. Haertel, K. H. Straub, and P. E. Roundy, 2009: Convectively coupled equatorial waves. *Reviews of Geophysics*, **47** (2), RG2003.
- Kimball, S. K. and M. S. Mulekar, 2004: A 15-year climatology of north Atlantic tropical cyclones. Part I: Size parameters. *Journal of Climate*, **17** (18), 3555–3575.
- Knutson, T. R., et al., 2010: Tropical cyclones and climate change. *Nature Geoscience*, **3**, 157–163.
- Lander, M. A., 1994: Description of a monsoon gyre and its effects on the tropical cyclones in the western North Pacific during August 1991. *Weather and Forecasting*, **9** (4), 640–654.
- Lin, Y.-L., R. D. Farley, and H. D. Orville, 1983: Bulk parameterization of the snow field in a cloud model. *Journal of Climate and Applied Meteorology*, **22** (6), 1065–1092.
- Liu, K. and J. C. Chan, 2002: Synoptic flow patterns associated with small and large tropical cyclones over the western North Pacific. *Monthly Weather Review*, **130** (8), 2134–2142.
- Liu, K. S. and J. C. L. Chan, 1999: Size of tropical cyclones as inferred from ERS-1 and ERS-2 data. *Monthly Weather Review*, **127** (12), 2992–3001.
- Mendelsohn, R., K. Emanuel, S. Chonabayashi, and L. Bakkensen, 2012: The impact of climate change on global tropical cyclone damage. *Nature Climate Change*, **2**, 205–209.
- Merrill, R. T., 1984: A comparison of large and small tropical cyclones. *Monthly Weather Review*, **112** (7), 1408–1418.
- Miglietta, M. M. and R. Rotunno, 2010: Numerical simulations of low-cape flows over a mountain ridge. *Journal of the Atmospheric Sciences*, **67** (7), 2391–2401.
- Molinari, J., D. M. Romps, D. Vollaro, and L. Nguyen, 2012: CAPE in tropical cyclones. *Journal of the Atmospheric Sciences*, **69** (8), 2452–2463.

- Montgomery, M., M. Nicholls, T. Cram, and A. Saunders, 2006: A vortical hot tower route to tropical cyclogenesis. *Journal of the Atmospheric Sciences*, **63** (1), 355–386.
- Mrowiec, A. A., S. T. Garner, and O. M. Pauluis, 2011: Axisymmetric hurricane in a dry atmosphere: Theoretical framework and numerical experiments. *Journal of the Atmospheric Sciences*, **68** (8), 1607–1619.
- Munich Re, 2011: Significant natural catastrophes 1980 - 2011: 10 costliest events worldwide ordered by insured losses (NATCAT). Accessed: 2013-04-11, <http://www.munichre.com/en/reinsurance/business/non-life/default.aspx>, Accessed: 2013-04-11.
- NASA Jet Propulsion Laboratory, 2010: Sea winds on QuikSCAT. Accessed: 2013-04-11, <http://winds.jpl.nasa.gov/missions/quikscat/index.cfm>, Accessed: 2013-04-11.
- Nolan, D. S., E. D. Rappin, and K. A. Emanuel, 2007: Tropical cyclogenesis sensitivity to environmental parameters in radiative–convective equilibrium. *Quarterly Journal of the Royal Meteorological Society*, **133** (629), 2085–2107.
- Ooyama, K., 1969: Numerical simulation of the life cycle of tropical cyclones. *Journal of the Atmospheric Sciences*, **26** (1), 3–40.
- Parker, M. D., 2008: Response of simulated squall lines to low-level cooling. *Journal of the Atmospheric Sciences*, **65** (4), 13–23.
- Peduzzi, P., B. Chatenoux, H. Dao, A. De Bono, C. Herold, J. Kossin, F. Mouton, and O. Nordbeck, 2012: Global trends in tropical cyclone risk. *Nature Climate Change*, **2** (4), 289–294.
- Persing, J. and M. T. Montgomery, 2003: Hurricane superintensity. *Journal of the Atmospheric Sciences*, **60** (19), 2349–2371.
- Pielke Jr., R. A., 2007: Future economic damage from tropical cyclones: sensitivities to societal and climate changes. *Philosophical Transactions of the Royal Society A: Mathematical, Physical and Engineering Sciences*, **365** (1860), 2717–2729.
- Pielke Jr., R. A., J. Gratz, C. W. Landsea, D. Collins, M. A. Saunders, and R. Musulin, 2008: Normalized hurricane damages in the United States: 1900–2005. *Natural Hazards Review*, **9** (1), 29–42.
- Powell, M. D., S. H. Houston, L. R. Amat, and N. Morisseau-Leroy, 1998: The HRD real-time hurricane wind analysis system. *Journal of Wind Engineering and Industrial Aerodynamics*, **77**, 53–64.
- Powell, M. D., P. J. Vickery, and T. A. Reinhold, 2003: Reduced drag coefficient for high wind speeds in tropical cyclones. *Nature*, **422** (6929), 279–283.

- Quiring, S., A. Schumacher, C. Labosier, and L. Zhu, 2011: Variations in mean annual tropical cyclone size in the Atlantic. *Journal of Geophysical Research*, **116** (D9), 114.
- Rappin, E. D., D. S. Nolan, and K. A. Emanuel, 2010: Thermodynamic control of tropical cyclogenesis in environments of radiative–convective equilibrium with shear. *Quarterly Journal of the Royal Meteorological Society*, **136** (653), 1954–1971.
- Raymond, D. J., 1995: Regulation of moist convection over the west Pacific warm pool. *Journal of the Atmospheric Sciences*, **52** (22), 3945–3959.
- Reasor, P. D., M. T. Montgomery, and L. D. Grasso, 2004: A new look at the problem of tropical cyclones in vertical shear flow: Vortex resiliency. *Journal of the Atmospheric Sciences*, **61** (1), 3–22.
- Reasor, P. D., M. T. Montgomery, F. D. Marks Jr, and J. F. Gamache, 2000: Low-wavenumber structure and evolution of the hurricane inner core observed by airborne dual-doppler radar. *Monthly Weather Review*, **128** (6), 1653–1680.
- Ritchie, E. A. and G. J. Holland, 2006: On the interaction of tropical-cyclone-scale vortices. Part II: Discrete vortex patches. *Quarterly Journal of the Royal Meteorological Society*, **119** (514), 1363–1379.
- Rotunno, R. and G. H. Bryan, 2012: Effects of parameterized diffusion on simulated hurricanes. *Journal of the Atmospheric Sciences*, **69** (7), 2284–2299.
- Rotunno, R. and K. A. Emanuel, 1987: An air-sea interaction theory for tropical cyclones. Part II: Evolutionary study using a nonhydrostatic axisymmetric numerical model. *Journal of the Atmospheric Sciences*, **44** (3), 542–561.
- Schubert, W. H., M. T. Montgomery, R. K. Taft, T. A. Guinn, S. R. Fulton, J. P. Kossin, and J. P. Edwards, 1999: Polygonal eyewalls, asymmetric eye contraction, and potential vorticity mixing in hurricanes. *Journal of the Atmospheric Sciences*, **56** (9), 1197–1223.
- Simpson, J., E. Ritchie, G. Holland, J. Halverson, and S. Stewart, 1997: Mesoscale interactions in tropical cyclone genesis. *Monthly Weather Review*, **125** (10), 2643–2661.
- Smagorinsky, J., 1963: General circulation experiments with the primitive equations. *Monthly Weather Review*, **91** (3), 99–164.
- Smith, R., 1980: Tropical cyclone eye dynamics. *Journal of Atmospheric Sciences*, **37**, 1227–1232.
- Smith, R. K. and M. T. Montgomery, 2008: Balanced boundary layers used in hurricane models. *Quarterly Journal of the Royal Meteorological Society*, **134** (635), 1385–1395.

- Smith, R. K., C. W. Schmidt, and M. T. Montgomery, 2011: An investigation of rotational influences on tropical-cyclone size and intensity. *Quarterly Journal of the Royal Meteorological Society*, **137** (660), 1841–1855.
- Smith, R. K. and S. Vogl, 2008: A simple model of the hurricane boundary layer revisited. *Quarterly Journal of the Royal Meteorological Society*, **134** (631), 337–351.
- Sobel, A. H. and C. S. Bretherton, 2000: Modeling tropical precipitation in a single column. *Journal of Climate*, **13** (24), 4378–4392.
- Tang, B. and K. Emanuel, 2010: Midlevel ventilation’s constraint on tropical cyclone intensity. *Journal of the Atmospheric Sciences*, **67** (6), 1817–1830.
- Tang, B. and K. Emanuel, 2012: A ventilation index for tropical cyclones. *Bulletin of the American Meteorological Society*, **93** (12), 1901–1912.
- Thorncroft, C. and K. Hodges, 2001: African easterly wave variability and its relationship to Atlantic tropical cyclone activity. *Journal of Climate*, **14** (6), 1166–1179.
- Wang, Y., 2002: Vortex Rossby waves in a numerically simulated tropical cyclone. Part II: The role in tropical cyclone structure and intensity changes. *Journal of the Atmospheric Sciences*, **59** (7), 1239–1262.
- Wang, Y., 2009: How do outer spiral rainbands affect tropical cyclone structure and intensity? *Journal of the Atmospheric Sciences*, **66** (5), 1250–1273.
- Weatherford, C. and W. Gray, 1988: Typhoon structure as revealed by aircraft reconnaissance. Part I: Data analysis and climatology. *Monthly Weather Review*, **116** (8), 1032–1043.
- Xu, J. and Y. Wang, 2010: Sensitivity of the simulated tropical cyclone inner-core size to the initial vortex size. *Monthly Weather Review*, **138** (11), 4135–4157.
- Zeng, Z., Y. Wang, and C.-C. Wu, 2007: Environmental dynamical control of tropical cyclone intensity—an observational study. *Monthly Weather Review*, **135** (1), 38–59.